R-99-11

Modelling of excavation depth and fractures in rock caused by tool indentation

Kou Shaoquan, Tan Xiangchun, Lindqvist P-A
Luleå Unviversity of Technology

October 1997

Svensk Kärnbränslehantering AB
Swedish Nuclear Fuel
and Waste Management Co
Box 5864
SE-102 40 Stockholm Sweden
Tel 08-459 84 00
+46 8 459 84 00
Fax 08-661 57 19
+46 8 661 57 19

ISSN 1402-3091
SKB Rapport R-99-11

Modelling of excavation depth and fractures in rock caused by tool indentation

Kou Shaoquan, Tan Xiangchun, Lindqvist P-A

Luleå University of Technology

October 1997

Keywords: Indentation, Rock, Indentation depth, Crack length, Similarity analysis, Numerical Analysis, Rock drilling, Tunnel boring

ABSTRACT

The hydraulic regime after excavation in the near-field rock around deposition holes and deposition tunnels in a spent nuclear fuel repository is of concern for prediction of the saturation process of bentonite buffer and tunnel backfill. The hydraulic condition of main interest in this context is a result of the fracture network that is caused by the excavation. Modelling of the excavation disturbed zone in hard rocks caused by mechanical excavation has been carried out in the Division of Mining Engineering, Luleå University of Technology since 1993. This report contains an overview of the work conducted. The mechanical excavation is reasonably simplified as an indentation process of the interaction between rigid indenters and rocks. A large number of experiments have been carried out in the laboratory, and the results used for identifying crushed zones and fracture systems in rock under indentation are presented based on these experiments. The indentation causes crushing and damage of the rock and results in a crushed zone and a cracked zone. The indenter penetrates the rock with a certain depth when the force is over a threshold value relevant to the rock and tool. Outside the cracked zone there are basically three systems of cracks: median cracks, radial cracks, and side cracks. Fully developed radial cracks on each side of the indented area can connect with each other and join with median crack. This forms the so-called radial/median crack system. The influence of the mechanical properties of the rock is discussed based on our conceptual model, and the main factors governing the indentation event are summarised. The cracked zone is dealt with by an analytical fracture model. The side crack is simulated by applying the boundary element method coupled with fracture mechanics. Functional relationships are established relating either the indentation depth or the length of radial/median cracks to the various quantities characterising the physical event, namely the shape and the size of the indenter and the properties of the rock, etc. Results in the form of equations combining the theoretical approach and the experimentally obtained data provide new and more profound understanding of the physical mechanisms of rock indentation process. The conceptual model therefore advances into calculable formulas and computer codes for predicting the indentation depth, cracked zone, side crack and radial/median crack lengths for different shapes of indenter and various hard rocks with a reasonable accuracy.

SAMMANFATTNING

De hydrauliska förhållandena efter bergavverkning i närfältberget runt deponeringshål och deponeringstunnlar i ett djupförvar för använt kärnbränsle är betydelsefulla för prognosticering av vattenmättnadsprocessen hos bentonitbufferten och tunnelåterfyllningen. De i sammanhanget intressanta förhållandena bestäms av det spricksystem som utbildas under bergavverkningen. Modellering av den störda zonen i hårt berg orsakad av mekanisk bergavverkning har utförts vid avdelningen för bergteknik, Luleå tekniska universitet sedan 1993. Denna rapport innehåller en sammanfattning av genomfört arbete. Mekanisk bearbetning av berg kan förenklat betraktas som en inträngningsprocess genom samverkan mellan ett stelt borrverktyg och berget. Ett stort antal experiment har genomförts i vårt laboratorium vilka legat till grund för identifiering av krosszoner och spricksystem under inträngning av verktyg i en bergyta. Inträngningen ger upphov till en krossad och en uppsprucken zon. Borrverktyget tränger in i berget till ett visst djup om den inträngande kraften överstiger ett gränsvärde som beror på aktuell bergart och vertygets form. Utanför den uppspruckna zonen kan i princip tre olika spricksystem observeras nämligen medianssprickor, radialsprickor och sidosprickor. Fullt utvecklade radialsprickor på sidorna av verktyget kan nå ihop och samverka med medianssprickorna till ett system av median/radialsprickor. Med vår konceptuella modell som grund diskuteras inverkan av bergets mekaniska egenskaper och de olika faktorer som styr inträngningsförloppet summeras. Den uppspruckna zonen behandlas med en analytisk modell och sidosprickorna modelleras med boundary element metod kopplad med en brottmekanisk modell. Dimensionsanalytiska samband etableras som relaterar inträngningsdjup respektive längd på median/radialsprickor med olika storheter som karakteriserar den fysikaliska händelsen nämligen form och storlek på verktyget samt bergets fysikaliska egenskaper. Resultat i form av ekvationer som kombinerar teori och experimentell observationer ger en ny och djupare förståelse för inträngningsförloppets fysikaliska mekanismer. Den konceptuella modellen förs vidare till användbara formler och datorprogram för att beräkna inträngningsdjup, sprickzoner samt sidosprickornas och median/radialsprickornas längd för olika form på verktygen och olika bergarter med tillfredsställande noggrannhet.

CONTENTS

1 INTRODUCTION

The deep repository for spent nuclear fuel consists of a system of horizontal tunnels at a depth of about 400-700 meters in crystalline rock. Large vertical holes are bored in the floor of these tunnels for emplacement of canisters and surrounding bentonite buffer. The vertical holes are planned to be bored by means of a rotating crushing technique, while the tunnels will be excavated by either conventional drill and blast or by TBM-technique. In order to predict the saturation process of the buffer and the tunnel backfill the hydraulic regime of the rock closest to the openings has to be sufficiently well known, a hydraulic regime which is influenced by the structure of the fracture network that is created during excavation. It is well known that mechanical excavation damages the rock to a much less extent than drill and blast and this report presents a state-of-the-art on the knowledge of characteristic features of the disturbance caused by mechanical excavation. In most of the mechanical excavation methods the fundamental process is indentation of the rock by a bit and this report focuses the discussion on the topic of rock indentation.

Experiments have been carried out to map and quantify various rock indentation fractures. Four types of rock were indented at various levels of load by three different tools, i. e. hemispherical, truncated and cylindrical indenters. After indentation test, the specimens were cut into sections and fractures in the rocks were mapped by fluorescence discrimination method. Based on the experiments, a conceptual model concerning the fracture pattern caused by mechanical excavation was established. The indentation will cause crushing and damage to the rock and result in crushed zone and cracked zone. The indenter will penetrate the rock with a certain depth with a force over a threshold value. Outside the cracked zone there are basically three systems of cracks: median cracks, radial cracks, and side cracks. Fully developed radial cracks on each side of the indented area can connect with each other and join with median crack. This forms the so-called radial/median crack system.

Reasonable models for formulating the indentation fracture are proposed. The cracked zone is dealt with by an analytical fracture model. The side crack propagation is simulated by applying the boundary element method coupled with fracture mechanics. Several quantitative relationships are established by using similarity analysis in order to predict the indentation depth and the length of radial/median cracks induced by the three above-mentioned indenter types. This makes it possible to develop a quantitative relationship between indentation depth and crack length. Modification of the relationships to include the influence of confinement is discussed so that excavation at depths can be taken into account. The effects of tool shape,

rock properties, loading rate and pre-existing micro cracks, etc. on the fracture formation are also discussed.

2 PREVIOUS WORK AND OUR WORKING STRATAGY

2.1 PREVIOUS WORKS CONCERNING EXCAVATION-INDUCED CRACKS

Literature reviews concerning the excavation-induced-cracks were first performed by Pusch (1989) and later by Tan et al. (1994). Theoretical and experimental research work related to the rock fracture beneath an indenter was carried out by Kumano et al. (1982), Cook et al. (1984), Pang et al. (1990) and Lindqvist et al. (1994), among others. Although their research works improved the understanding of the mechanisms a great deal, it is still difficult to apply the results in estimating the crack distribution around an excavation contour.

In rock excavation engineering, one major requirement is to predict and improve excavation efficiency. This requirement has been directed to solving a problem of excavation depth. The model for excavation depth should result in an accurate relation between the force magnitude and force distribution exerted by the excavating tool and the induced cutting depth, which is able to suit various specific conditions in the field characterised by various kinds of machine heads and operating conditions, rock types as well as geological structures. Potts and Shuttleworth (1958), Evans (1962), Roxborough (1973), Nishimatsu (1972), and Roxborough and Phillips (1975) worked in this direction. Their efforts have been summarised in detail by Whittaker et al. 1992. Various formulas relevant to this subject have been developed. These formulas can partly fulfil the urgent demand for practical solution of the production problems. However, two things can be argued: 1) Most of the formulas did not take the mechanical behaviours of rock fracture into consideration but the fracture toughness of rock is an important parameter for describing the rock cuttability according to Gao (1990); 2) All of the above formulas predicted a zero value of cutting force when cutting depth approaches zero. This is contradicted by our common sense. A threshold cutting force relevant to the rock and the cutter is always required in practical cutting performance for any kinds of rock.

In addition, there are also some efforts to simulate rock cutting phenomena by applying fracture mechanics principles coupled with numerical approaches of Finite Element Method or Boundary Element Method (Hardy 1973, Zeuch et al. 1983, Saouma and Kleinosky 1984, Ingraffea 1987) and the Displacement Discontinuity Method (Hua 1990 and Sun et al 1992). The advantage of the numerical methods is that the complex stress state and the crack propagation paths in the rock cutting process can be calculated based on certain assumptions. The most important assumption in these models is that the fracture process zone can be ignored and the linear elastic fracture mechanics can be applied. All of the above works deepen our knowledge in

understanding the rock cutting mechanism, the discrepancy between the prediction and the experiments is, however, still significant. In other words, more efforts are still needed.

2.2 OUR WORKING STRATEGY

Although problems related to mechanical excavation were noted quite a long time ago and active studies have been pursued ever since, the industry is still faced with uncertainties in the prediction of boring or cutting speed and the cracks in the remaining rocks. Careful analysis indicates that this unsatisfactory state is a consequence of the lack of fundamental understanding of the mechanism of mechanical excavation and identification and quantification of basic controlling factors, to a large extent, due to the complication of the geology, geometry and the conditions in-situ in the rock excavation. Careful analysis of the practical excavation also indicates that the key factor of mechanical boring is the interaction between the machine's head and the rock. This interaction can be classified as two types: indentation type and drag bit type. For most of the hard rock, the machines normally used belong to the indentation or rotary crushing type. Rock indentation by a bit is, therefore, the basic process in the tunnel boring of medium and hard rocks.

In rock indentation the bit is forced into the rock, and the rock near the bit is crushed into small or large fragments, leaving subsurface cracks in the remaining rock wall. Rock indentation is actually the interaction between the rock and the indenter. In order to understand the indentation process, three aspects must be dealt with. They are the characteristics of the indenter, the properties of the rock and the environmental conditions of the indentation process. The mechanical tools can in most cases be assumed to be rigid during the interaction between the tool and the rock, since the rigidity of the tool is normally much higher than that of the excavated rocks. The tool can, therefore, be simply represented by a distributed load along the tool-rock contact boundary. In most practical situation, rock indentation is carried out under an environment similar to semi-infinitive rock mass.

The above understanding has led us from the field to the laboratory. In order to clarify the mechanism, numerous indentation tests, analytical and numerical works have been carried out at Luleå University of Technology. In our research the practical problem is simplified. The simplified problem has the following characteristics: the most important governing factors are involved, the environmental conditions in the experiment are controllable, the geological variations are kept to a minimum, and the geometrical configuration is made as simple as physically meaningful. This made it possible to do a meaningful laboratory test under controlled environmental conditions and to make an effective physical and mathematical analysis on the simplified problem. The samples of a controlled indentation experiment in the laboratory are normally prepared so that the radial displacement of the rock cylinder under indentation is approximately equal to that induced in a semi-infinite rock body under a given load (Lindqvist et al, 1994). In this

way the samples can be treated as a semi-infinite rock mass. It is the subsurface cracks in the remaining rock induced by indentation that must be taken into consideration when designing a repository for nuclear waste in the Swedish bedrock. Based on the experiment and a preliminary theoretical analysis, the crack pattern is found, in general, to be governed by macro mechanical properties of rock, if the characteristic sizes of the micro structure are smaller than the indenter. The micro structure of the rock plays an important role only in determining the details of the cracks. In this way, continuum mechanics can be useful in analysing rock indentation process. This lays out the foundation of the conceptual model of the indentation mechanisms given by Kou et al. (1994). More specific discussions about the indentation fracture have been presented by Kou et al. (1995a and 1995b). Numerical analysis has advantages to clearly present the stress distribution induced by indentation and therefore, can be beneficial in clarifying the mechanisms of the crack formulation (Tan et al. 1997). It compensates the limitation of experimental and analytical works. The above-mentioned works have resulted in models (*indentation crack models*) to better govern rock indentation and constitute the first important step of our project.

In order to approach the real practical problem we have to go out from the laboratory and back to the field step by step. The second step is therefore to advance the indentation crack model to describe the fracture system induced by TBM boring by taking secondary factors into consideration, which is defined as the *TBM crack model.* The third step is to establish a bridge between our crack model and the prediction of the hydraulic conductivity corresponding to the TBM induced-cracked area, which is defined as *TBM hydraulic model.* These three steps constitute the main strategy of our work. In many cases similar processes have to be repeated in order to fully understand the process of rock excavation by mechanical methods and to contribute to the development of the boring industry.

3 EXPERIMENTAL STUDY

Rock indentation is actually the interaction between the rock and the indenter. In order to understand the indentation process, three aspects must be dealt with. They are the characteristics of the rock, the characteristics of the indenter and the environmental conditions of the indentation process.

3.1 CHARACTERISTICS OF THE ROCKS

Four typical Swedish rocks were selected to represent different medium and hard rocks. They were Kallax gabbro, Bohus granite, Ekeberg marble and Lemunda sandstone.

The Kallax gabbro massif is dark grey with medium grain size. The results of modal analysis of two thin sections are given in table 3-1. The plagioclases have a composition of andesine - labradorite and a mean grain size of 0.9 mm. The pyroxenes, one with faint beige pleokroism and one with red brown pleokroism occur together. They often have inclusions of opaque minerals or feldspar and are clinopyroxenes. The olivine grains are full of cracks and surrounded by serpentine. There are some micro cracks in the plagioclase due to transformation to serpentine.

Table 3-1 Mineral composition of Kallax gabbro observed in two sections.

Compositions	1st (Vol. %)	2nd (Vol. %)
Plagioclase	61.6	53.8
Pyroxene (2 types)	23.8	29.2
Olivine	3.6	5.6
Biotite	6.9	tr[1]
Opaque minerals	2.8	4.9
Accesoirs	1.4	3.5
Serpentine, Chlorite	tr. [1)]	3.1

The Bohus granite is the name of a 20×90 km^2 large granite massif along the northern west coast of Sweden. It is a post tectonic granite with no signs of ductile deformation and shows well-developed orthogonal cleavages. The massif consists of a number of different intrusions with different colours, grain sizes and textures with both sharp and gradual transitions. Although it has different appearance, most modal analyses show that it is a

[1)] tr.= trivial

monzogranite. The rock mineral composition from a modal analysis of a thin section is given in table 3-2. The granite is usually massive but sometimes a diffuse layering could be seen. The tested material is light greyish red medium grained with large potassium feldspar individuals up to 10 mm. The microcline is pertithic, which means that inclusions of plagioclase due to exsolution could be seen. It varies in grain size up to 9.1 mm with a mean value around 1.8 mm. The larger grains often show twinning. Plagioclase with the composition of oligoclase has a grain size up to 3.4 mm. The quartz grains measure up to 3.6 mm. Other minerals have small grain size. Grain boundaries are relatively simple and undulating. Micro cracks occur mainly in quartz, but also appear in feldspar. They are either intragranular or transgranular. They are sometimes filled with a mineral of high interference colour, which is probably serizite. Some grain boundaries are marked with epidote. There are some alterations. Feldspar, mainly, plagioclase is seritizised in the centre and some of the biotite is altered to chlorite. The large grain size, the relatively simple grain boundaries and micro cracks make the rock easily cracked.

Table 3-2 Mineral composition of Bohus granite.

Compositions	Volume (%)
Microcline (perthitic)	37
Plagioclase (An 25-30%)	26
Quartz	31
Biotite	
Muscovite	6
Opaque minerals	
Accoirs	

The Ekeberg marble is from the province of Närke. The variety used is a fine- to medium- grained, well-recrystallized carbonate with occasional inclusion of larger grains of amphibole. The carbonate grains are comparatively similar in size and equally dimensioned. No pronounced anisotropy can be observed in the thin sections although amphiboles have a layered orientation. Mineral composition is given in table 3-3. Dolomite is the dominating carbonate mineral but one or two per cent of calcite also appears. Grain boundaries are wavelike, and the grains well interlocked.

Table 3-3 Mineral composition of Ekeberg marble

Compositions	Volume (%)
Carbonate	91.0
Amphibole	4.5
Mica (Phologopit)	3.5
Accessory minerals	0.9

The mean grain diameter of dolomite is 0.27 mm (0.02 - 0.98 mm). Amphibole, partly altered, has a grain size of 0.5 - 5 mm. Flakes of a colourless mica (phlogopite) appear occasionally with a grain size of 0.05 - 0.1 mm. They are to a certain extent oriented in the same direction as amphibole crystals. Apart from cleavage planes of carbonates, micro cracks following grain boundaries are sometimes observed. The porosity is very low. Due to the characteristics of the rock (mineral content, grain size, isotropy) stress will occur at many sites and the crack pattern is expected to be irregular on a local scale.

The Lemunda sandstone is quarried at the NE shore of lake Vättern. It is yellow to yellowish white and porous. Frequent sedimentary structures can be seen. Around 95 % of the rock composition is quartz. The rest is rock fragments (quartz, granite), weathered feldspar grains and minor amounts of small mica flakes, heavy minerals and clay minerals. The texture of the sandstone is shown in the photo (Figure 3-1) where black areas are pores and traces of grains lost during thin section preparation. Some of the quartz grains show their original sand grain form but in most cases there is a secondary growth of quartz on the original grain as can be seen in the photo. The grain boundaries between these secondary grown quartz are simple and straight. The mean grain size is 0.35 mm (minimum 0.05, maximum 1.09 mm). Void index determined in the laboratory according to ISRM standard tests is 5 %. (Void index is defined as the water content after drying in dessicator followed by 1 hour immersion in water). The pores and simple grain boundaries give the rock poor strength.

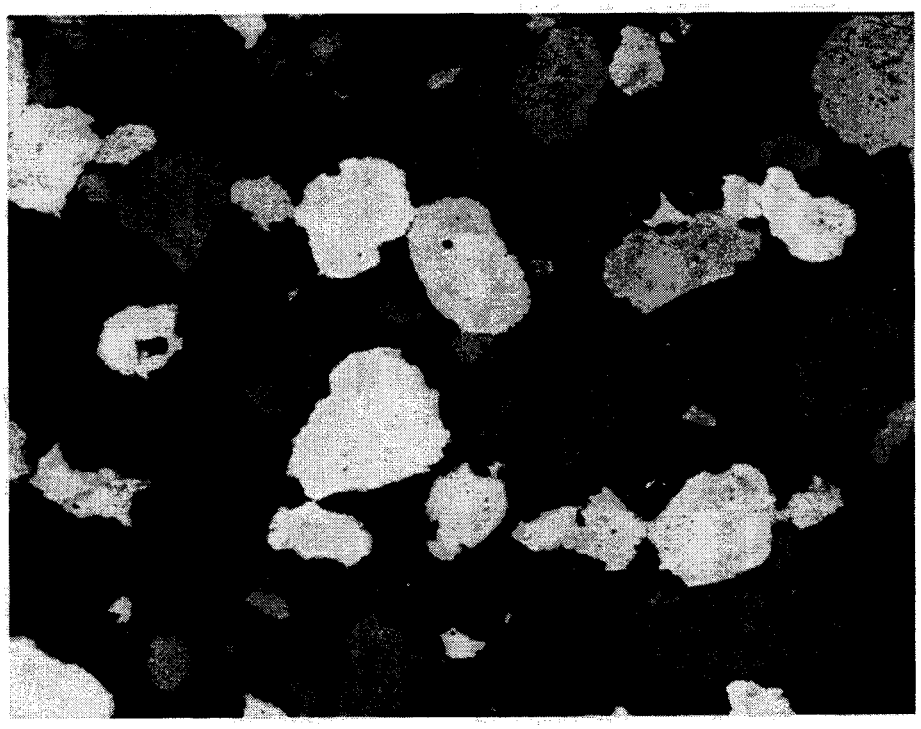

***Figure 3-1** Lemunda sandstone (× 63).*

The geological structures were avoided and the specimen material was identified as uniform as possible when the test samples were selected. Important rock mechanical parameters of these rocks tested for different purposes were previously accumulated and shown in table 3-4.

Table 3-4 Rock mechanical parameters[2].

Mechanical properties	Kallax Gabbro	Bohus granite	Ekeberg marble	Lemunda sandstone
Density, ρ (kg/m^3)	3052±12 (5)[1]	2634±8 (6)[2]	2848±9 (6)[2]	2243±32 (4)[2]
Uniaxial compressive strength, σ_c (MPa)	279±8 (5)[1]	152.8± 13.3 (6)[2]	160.4± 14.5 (6)[2]	55.1±15.9 (4)[2]
Young's modules, E (GPa)	98.9±3.6 (5)[1]	64.1±3.8 (6)[2]	84.4±2.6 (6)[2]	26.5±5.5 (4)[2]
Poisson's ratio, ν	0.31± 0.03 (5)[1]	0.31±0.06 (6)[2]	0.35±0.04 (6)[2]	0.38±0.06 (4)[2]
Critical energy release rate, bending test, G (J/m^2)	51.3±7.2 (18)[1]	100-110[4]	40.5±6.6 (4)[3]	113±49 (4)[3]

3.2 CHARACTERISTICS OF THE TOOLS

Three different types of indenters, a hemispherical, a cylindrical and a truncated simulating a worn hemispherical, were used in the indentation tests. The material of the indenter is hard alloy. The dimensions of the indenters are shown in Figure 3-2.

The indenters can in most cases be assumed to be rigid during the interaction between the tool and the rock, since the rigidity of the tool is much higher than that of the rocks. The tool can, therefore, be simply represented by a distributed load along the tool-rock contact boundary.

[2]The figures in square brackets [ ] indicate the data sources: [1] Vutukuri et al., 1983, [2] Holmberg and Forslund, 1989, [3] Ochterlony, 1986, and [4] Div. of Rock Mechanics, Luleå Univ. of Tech., 1993. The figures between parentheses ( ) indicate the number of tests for the corresponding average value.

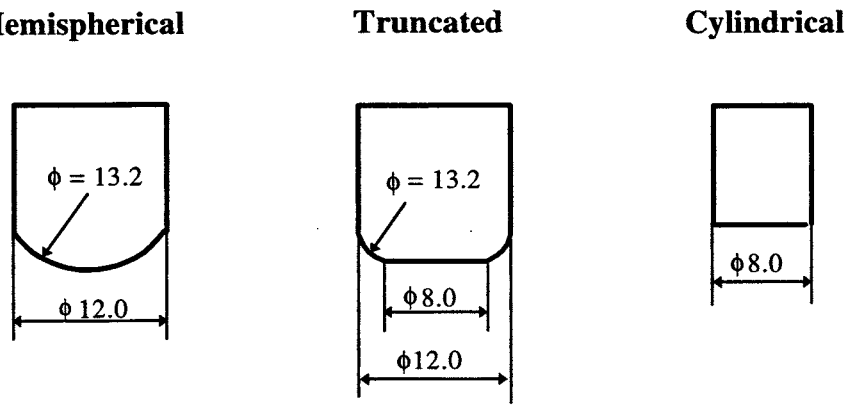

***Figure 3-2** Indenter types used in the experiments.*

3.3 INDENTATION ENVIRONMENT

It is typical in actual field operation that indenters penetrate into a semi-infinite rock mass. It is, however, rather difficult to guarantee the semi-infinite condition in laboratory due to the dimensional limitation of the specimen. Our strategy is to confine a cylindrical rock sample in a steel ring which is much stiffer than the rock, so that the deformation of the rock under the action of the indenter can be approximated to the desired.

Assuming that there is a semi-infinite rock mass with uniformly distributed radial stress of p applied at a cylindrical surface with radius of a, the radial displacement u_r of rock at radius r, with $r \leq a$, can be derived according to Hooke's law as

$$u_r = \frac{pa^2}{2G_r r} \qquad 3\text{-}1$$

where G is the shear modulus, which is related with Young's modulus E and Poisson's ratio ν by the following relation

$$G_r = \frac{E_r}{2(1+\nu_r)} \qquad 3\text{-}2$$

where the subscript r refers to rock. At the cylindrical surface, where r equals a, the displacement named u_r is therefore

$$u_R = \frac{p\,a}{2\,G_r} \qquad 3\text{-}3$$

The radial displacement of a steel annulus with the same magnitude of compressive stress p as the rock applied at the inner surface can also be calculated from Hooke's law as

$$u_s = \frac{pa}{2G_s} \frac{\frac{b^2}{a^2} + (1 - 2\nu_s)}{b^2 / a^2 - 1} \qquad 3\text{-}4$$

where a is the radius of the inner surface, and b is the radius of the outer surface of the annulus. The parameters with subscript s represent the corresponding mechanical properties for steel. When

$$u_R = u_s \qquad 3\text{-}5$$

the steel annulus can provide a confining effect in a manner approximately similar to a semi-infinite rock mass. Equations (3-1), (3-4) and (3-5) then give

$$\frac{b^2}{a^2} = \frac{1 + (1 - 2\nu_s) G_r / G_s}{1 - G_r / G_s} \qquad 3\text{-}6$$

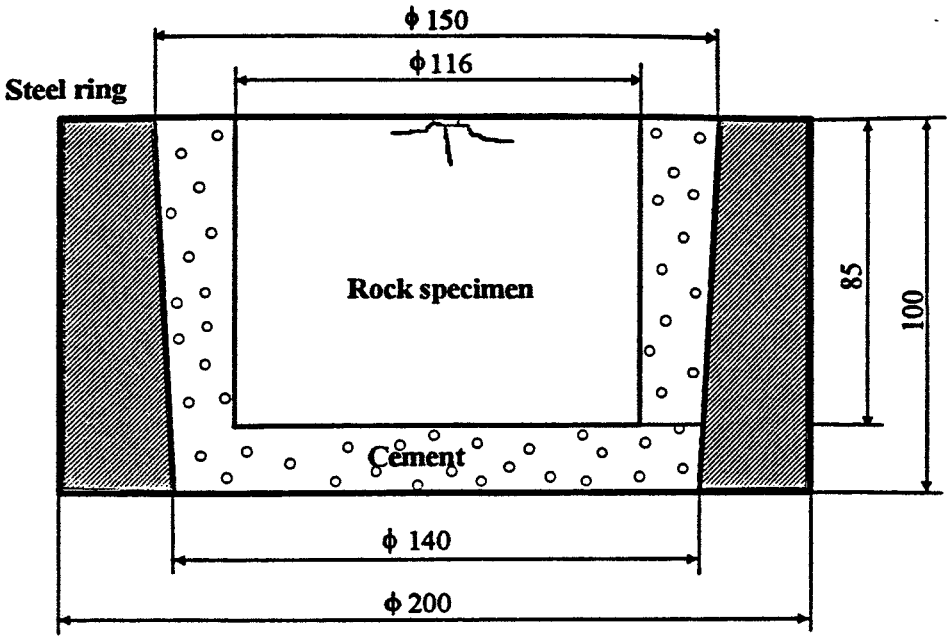

***Figure 3-3** Designed dimensions of steel ring, cement and rock sample.*

Equation (3-6) indicates that for given properties of rock and steel, it is possible to select the ratio between the inner and outer radii of a steel ring so that a confinement similar to the semi-infinitive case can provide to a rock cylinder. The outer radius b of the steel annulus can be calculated with a given inner radius $a = 75$ *mm* from Eqs. (3-6) and (3-2). The calculated outer

radii b of the steel annulus are 119, 98, 106 and 82 *mm* for Gabbro, Kallax, Bohus granite, Ekeberg marble and Lemunda sandstone respectively when the rock properties shown in table 3-4 and the properties of the steel ring, whose Young's modulus E, Poisson's ratio ν and the shear modulus G_s are 205 *GPa,* 0.3 and 78.9 *GPa* respectively, were used. In the experiment, we simply manufactured the steel annulus with outer radii b of 100 *mm* for all of the four kinds of rock. The rock specimens were cast in the steel tube using a prefabricated cement named Betec with uniaxial compressive strength of 70-80 MPa, Young's modules 15-20 MPa and Poisson's ratio 0.1. The designed steel ring, cement and rock samples are shown in Figure 3-3.

Betec is a fast hardening cement that expands about one percent during hardening. Twelve percent of water in weight was added. As the steel tube is short and open in both ends no significant stresses were expected to build up by the slightly expanding thin layer of cement between the steel tube and the rock specimen. Time between casting and indentation testing was at least 24 hours. The dimensions of the rock sample were selected to avoid crack propagation possibly longer than half way through the sample for the strongest rock types loaded to 100 -150 kN. Judgement was made from experience of previous tests by Lindqvist (1982), Wagner (1971) and Cook et al. (1984).

3.4 INDENTATION EXPERIMENT

In the experiment, two displacement controlled rock mechanics testing machines were used. They were Instron of 0 -100 kN and Instron 0-4500 kN. The latter was for tests beyond 100 kN of load. A load cell with the capacity 450 kN was used to measure the indentation force and a LVDT to measure displacement. A constant rate of indentation, 0.05 mm/s, was used for all the tests. The experimental set-up is shown in Figure 3-4.

The typical recordings of the load-penetration relation during the indentation are shown in Figures 3-5 to 3-7. In the context the word penetration is used as a synonym of indentation depth. Tests in gabbro and granite exhibit the typical brittle failure. The load has to reach a certain threshold value before the first chipping takes place followed by a major penetration. This effect is then repeated. Chipping is often associated with a dramatic penetration (Figure 3-5). Marble behaves in a more ductile manner (Figure 3-6).

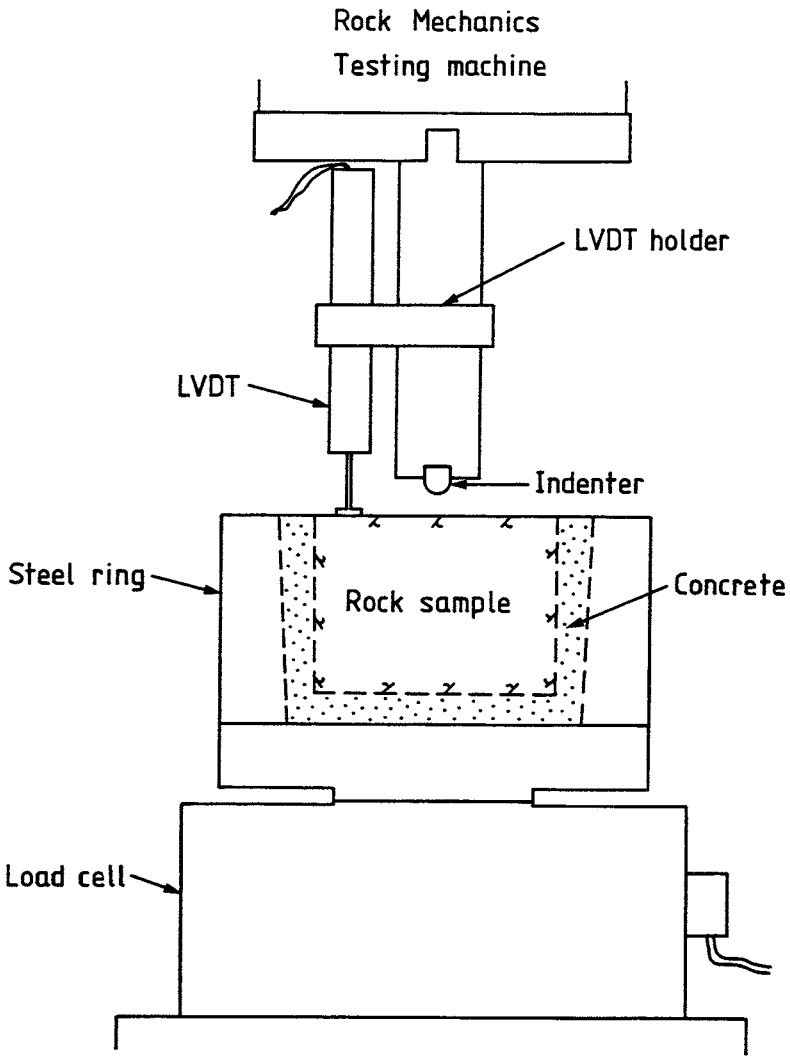

Figure 3-4 *Experimental set-up.*

Truncated and cylindrical indenters need to reach a threshold value before penetration starts. An interesting observation is that the resistance against penetration is lower for the cylindrical indenter compared with the truncated. The load- penetration curve for sandstone is however more linear for the hemispherical indenter and bilinear for the cylindrical or the truncated (Figure 3-7).

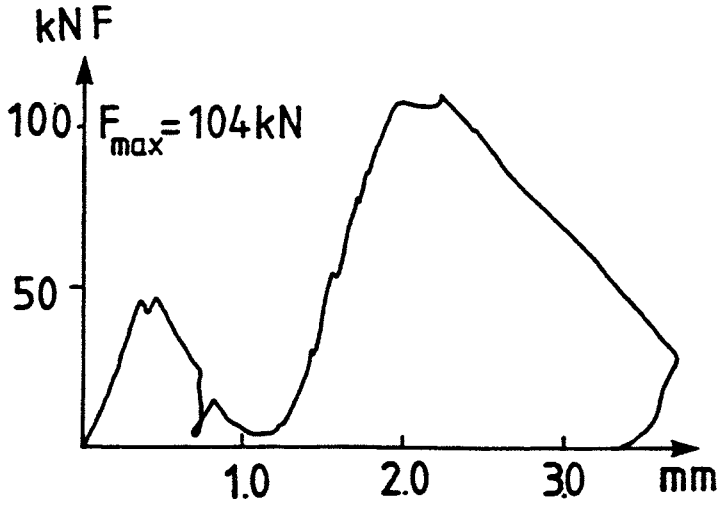

Figure 3-5 Load-penetration curve for gabbro by hemispherical indenter.

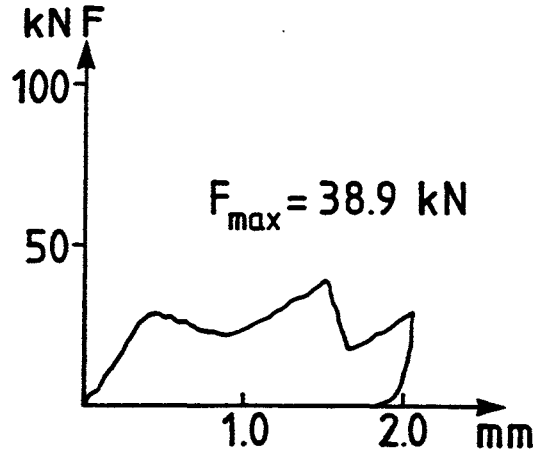

Figure 3-6 Load-penetration curve for marble by hemispherical indenter.

In order to observe the fracture system caused by indentation, the samples after indentation were cut into slabs with 3 - 4 *mm* in thickness. The specific cutting technique is shown in Figure 3-8. The cracks could then be observed through examination of each slab and the crack extension could be measured

by counting the width of each slab and the number of slabs. A fluorescent substance was introduced to successfully visualise the cracks in the slab.

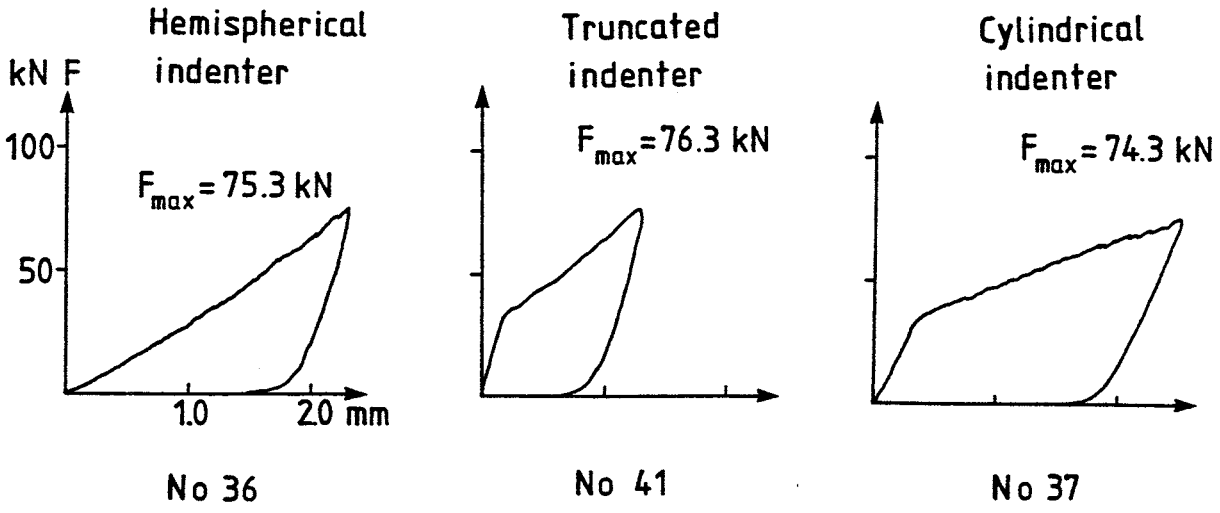

Figure 3-7 *Load-penetration curves for sandstone (sample no. 36, 41 and 37).*

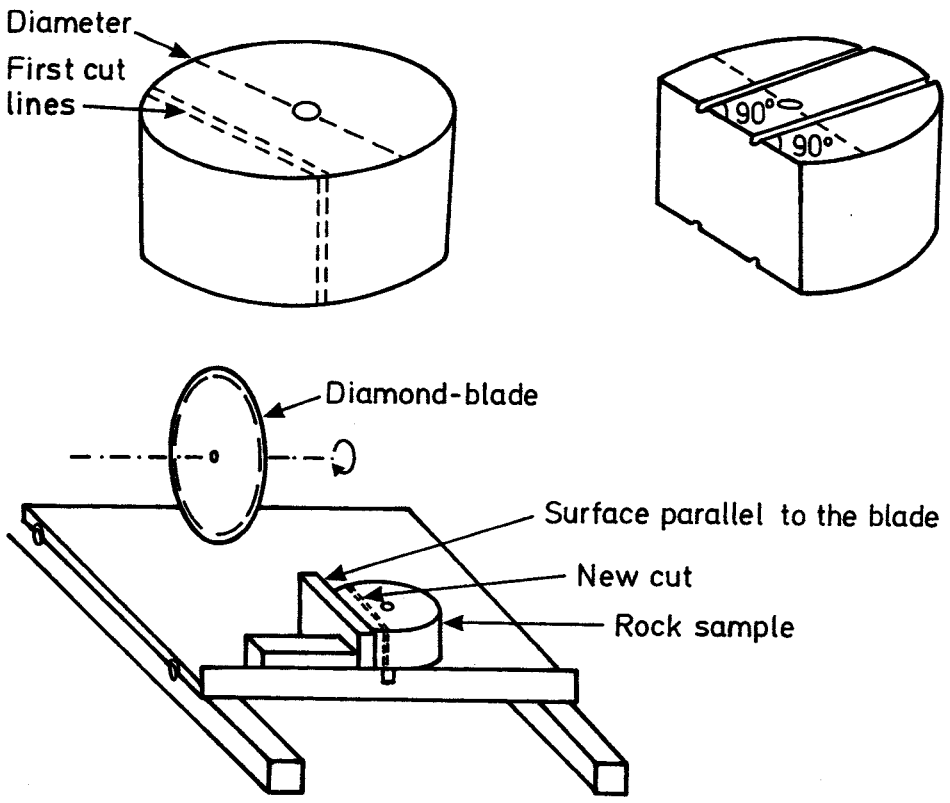

Figure 3-8 *Cutting of rock samples after indentation tests.*

Totally 63 samples of gabbro, granite, marble and sandstone have been indented by using hemispherical, truncated or cylindrical indenter. The minimum and maximum load used were 15 and 150 kN respectively. Discriminations of cracks have been made on 50 samples by using fluorescent penetrant and black light, but in the case of sandstone through natural light only. All slabs containing signs of crater formations were also photographed by using either normal light or black light or both. A total number of 600 black light and natural light photos are available from the test program. Typical photos of these rocks are given in Figure 3-9. The detailed descriptions about the tests have been presented by Lindqvist et al. (1994).

Sandstone, $F = 50$ *kN*

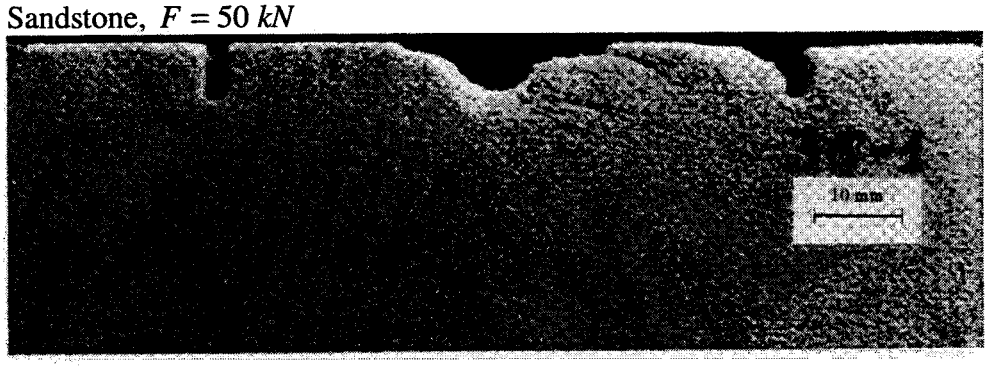

Marble, $F = 61$ *kN*

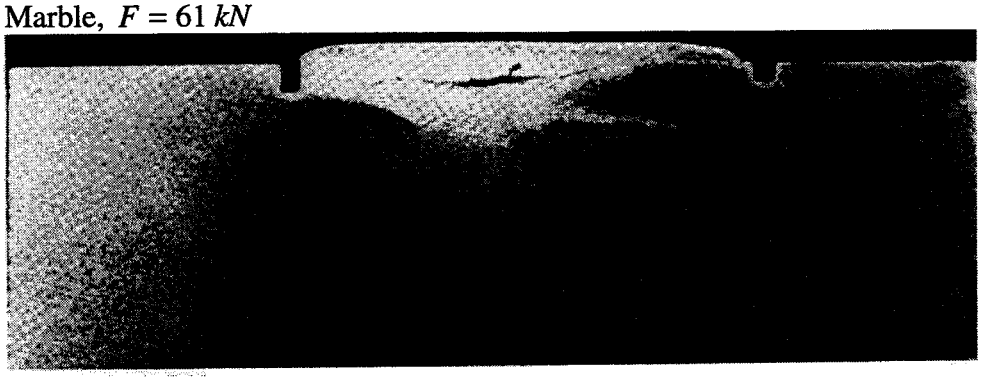

Granite, $F = 102$ *kN*

Figure 3-9 *Typical photos of fracture system induced by indentation into different rocks. The Photos here were taken from the central slabs of sandstone, marble and granite indented by a hemispherical indenter.*

4 FRACTURE SYSTEMS IN ROCK UNDER INDENTATION

From the above-mentioned experimental results, a general picture of fractures in rocks under indentation can be summarized in Figure 4-1. Underneath the indenter there are three zones, i.e. a zone of disintegrated and partly compacted rock fragments, a crushed zone, and a cracked zone. Outside the cracked zone there are basically three systems of cracks: median cracks, radial cracks, and side cracks. Sometimes Hertzian cracks (see Figure 2) are also observed in rocks under indentation with an axially-symmetric indenter. Fully developed radial cracks on each side of the indented area can connect with each other and join with median crack. This forms the so-called radial/median crack system. Many details could be added to this simple description, but the account offered does include the general effects.

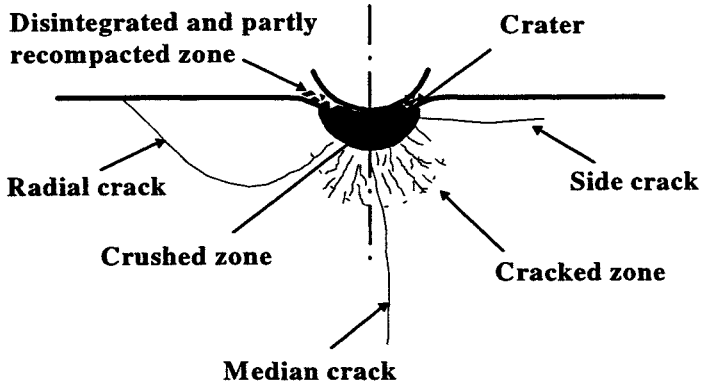

***Figure 4-1** General picture of fracture systems in rock under indentation.*

The various fractures shown in Figure 4-1 are defined as follows:

- *Crater* Cracks propagate from underneath the indenter to the surface outside the rock-indenter contact area forming a crater. The formation or enlargement of craters is sometimes due to side cracking and tilting of the rock fragments between the side crack and rock surface by a short crack.
- *Disintegrated and partly recompacted zone* The disintegrated and partly recompacted zone is formed by crushing and recompaction of rock material. This was verified by experiments carried out by Lai and Lindqvist (1980). This zone is treated as part of the crater fragments in the present work.
- *Crushed zone* The crushed zone is delineated by the whiteness in the photos taken from the slabs with fluorescent penetrant and black light. The rock is regarded as belonging to the crushed zone when, say, more than 90 per cent of the area in the black light photos is white. A difficulty

is that the developing procedures and photographing (thickness of developer, time of exposure, light intensity) can influence the size of the observed crushed zone.

- *Cracked zone* In the cracked zone, the whiteness in the photos is disintegrated. There are a lot of cracks in that zone but most of the cracks are rather short.
- *Hertzian crack* Hertzian or cone cracks are initiated outside the area of contact between rock and indenter. They propagate at an angle to the free surface of the rock and the crack face formed is like a cone.
- *Radial and median cracks* These two types of cracks develop radially from the indenting center. Radial cracks intersect with the rock surface and median cracks propagate into the rock.

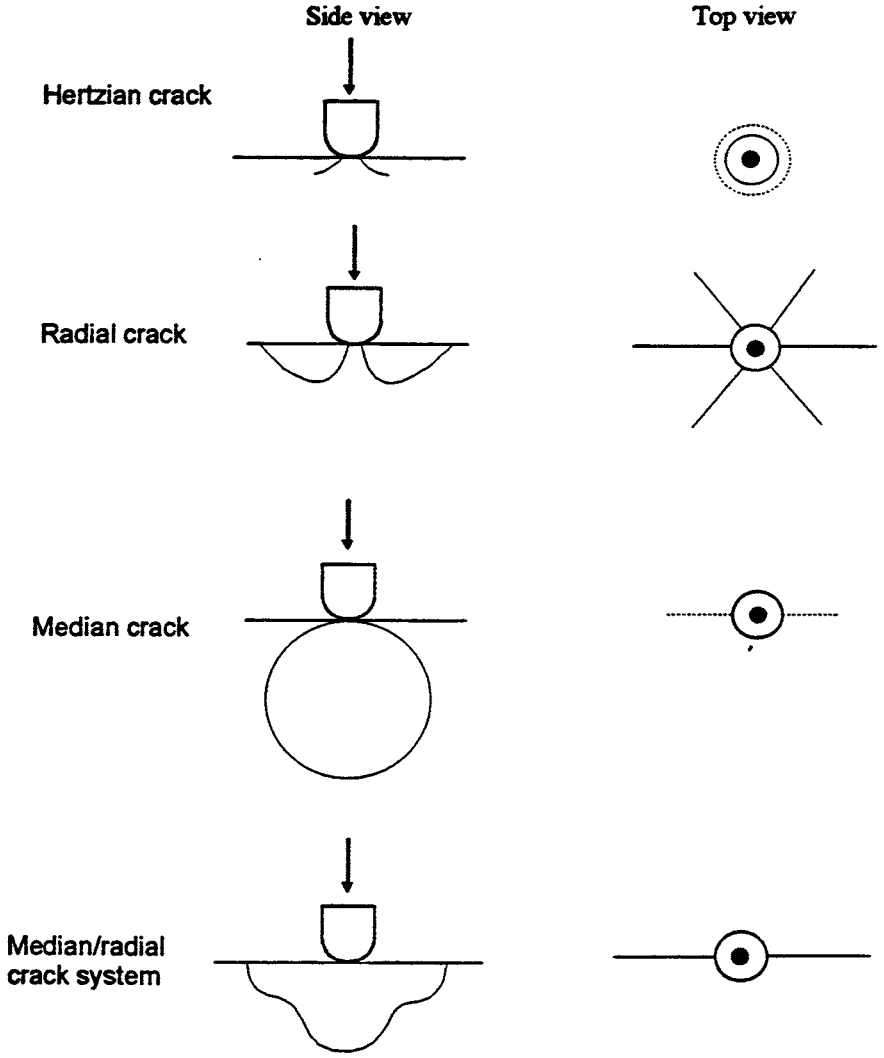

Figure 4-2 *Schematic description of Hertzian crack, radial crack, median crack and median /radial crack.*

- *Side cracks* Side cracks propagate from the indented area parallel or slightly angled to the rock surface. Side cracks form chips and they are considered to be the main rock removing fracture in rock drilling and boring.

The above-mentioned Hertzian crack, radial crack, and side crack are schematically shown in Figure 4-2.

The size of the crushed or the cracked zone and the lengths of various kinds of cracks are mainly dependent on the load magnitude. This can be seen from Figs. 4-3 to 4-7. The shapes of radial cracks of five different tests with the hemispherical indenter in gabbro are depicted in Figure 4-3. Between load levels, 104 kN and 123 kN, radial cracks on each side of the indented area connect to a median/radial crack system.

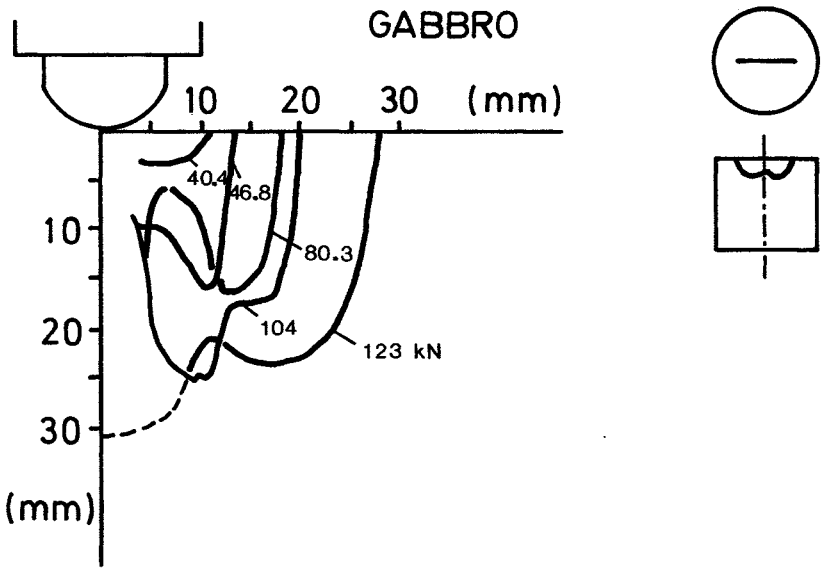

Figure 4-3 *The shape of radial cracks in gabbro induced by hemispherical indenter. The maximum load in kN corresponding to the crack shape is also shown in the figure.*

Quantitative values of indentation depth, length of side cracks and radial cracks with increasing load of hemispherical indentation in gabbro are shown in Figure 4-4. The fracture system in granite, sandstone and marble induced by the hemispherical indenter are qualitatively very similar to Figure 4-4.

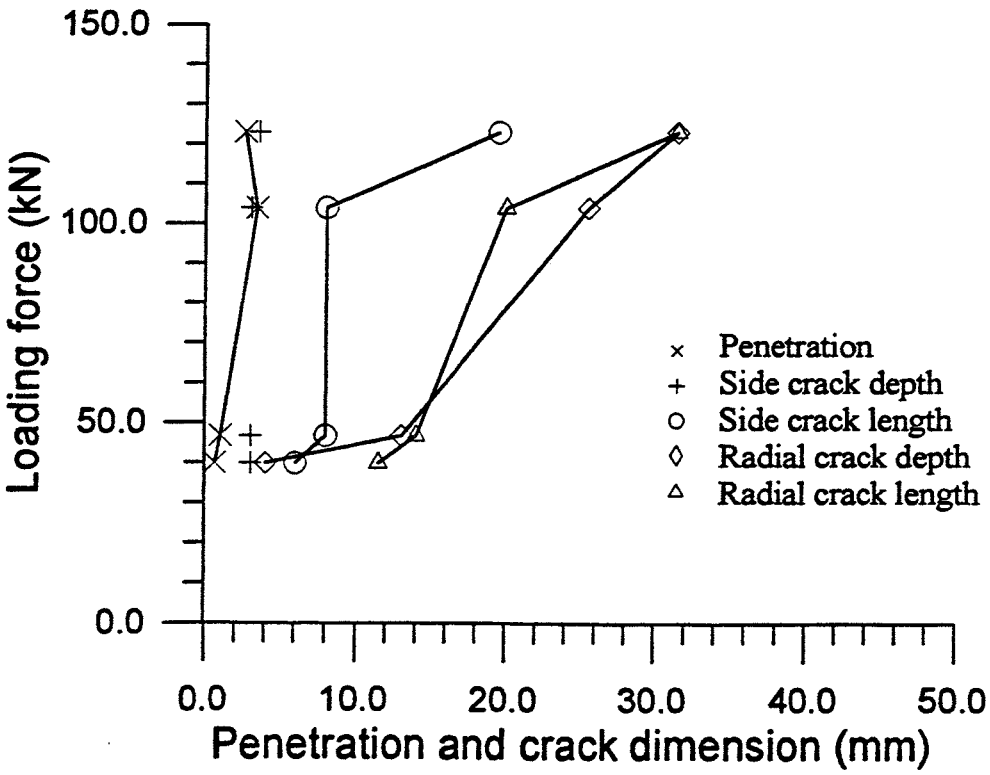

Figure 4-4 *Indentation depth and crack lengths in gabbro induced by hemispherical indenter.*

Side crack length versus load of hemispherical indenter for all the four rock types is shown in Figure 4-5. The staircase shape of the diagram of gabbro, granite and sandstone is associated with threshold values of chipping events. This gives evidence that side crack propagation is stepwise. Comparison of side crack length induced by the truncated and cylindrical indenters indicates that the truncated indenter gives shorter and the cylindrical indenter longer cracks than the hemispherical indenter at the same level of load.

The influences of increasing indentation load on radial crack depth are shown in Figure 4-6. Here crack depth is defined as the deepest position of the crack surface relative to the specimens' upper surface. Similar diagrams reveal that crack propagation is impeded by truncated and cylindrical indenters.

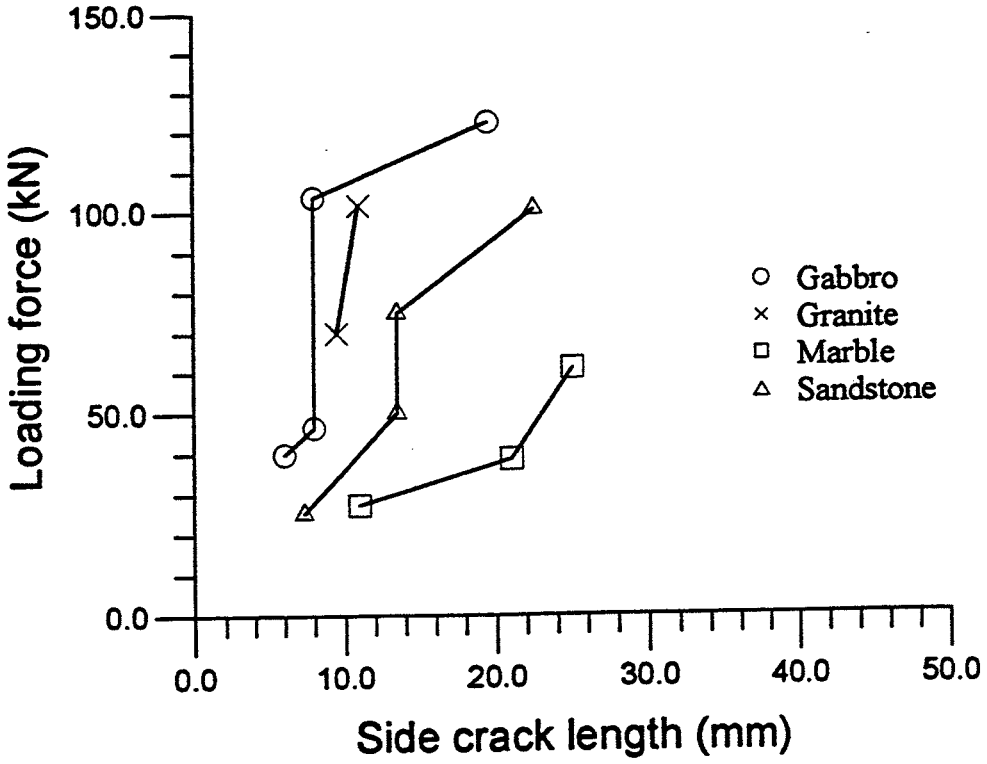

Figure 4-5 Side crack length versus loads for the four kinds of rock induced by the hemispherical indenter.

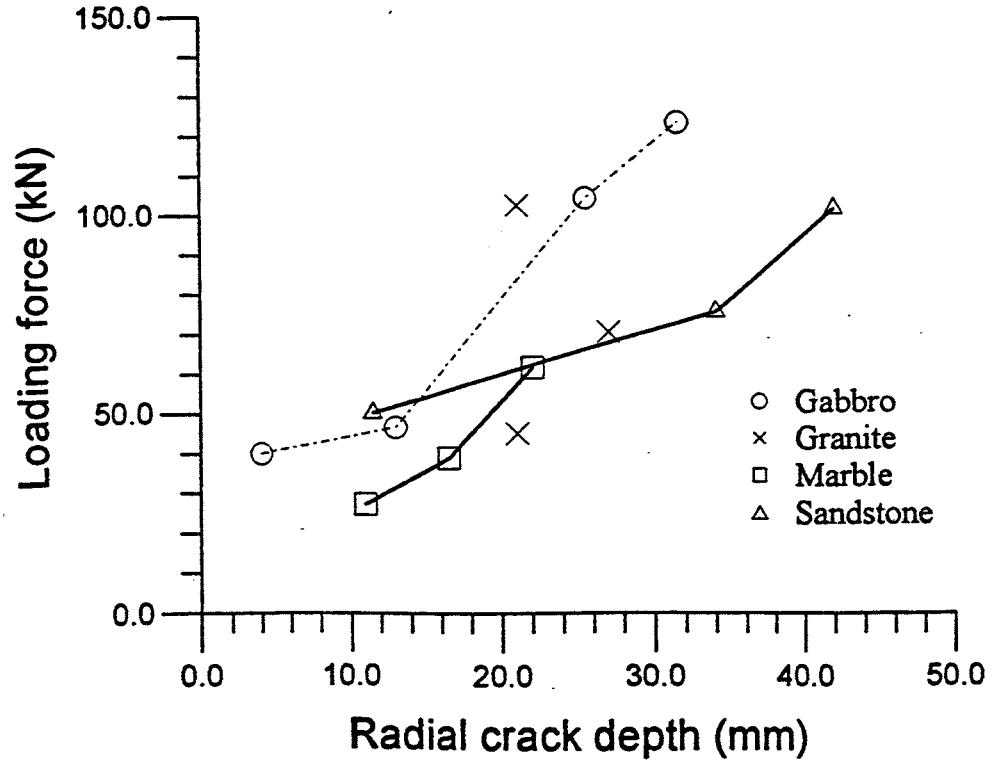

Figure 4-6 Loading force vs. radial crack depth induced by hemispherical indenter.

The above figures have shown the importance of the force magnitude for the fracture system. However, the properties of the rock and the geometry of the indenter play important roles as well.

Through the large number of experiments we have learnt the following:

- The load-displacement response curve obtained in the indentation test represents the interaction between the indenter and the rock. It reflects a combined reaction between the rock properties and the geometry of the indenter.
- The rock beneath the indenter undergoes severe compaction, and there is the formation of a crater, a crushed zone, a cracked zone and a number of different long cracks.
- The long crack system consists of radial crack, median crack, side crack and Hertzian crack. Radial/median crack is a fully developed long crack.
- The load has an important influence on indentation depth and fracture dimensions. High loads in general cause large fragments, and the formation of crater and fractures is often associated with critical threshold value of load.
- Indenter shape has an important influence on the crushing and fracture process. Cylindrical and truncated indenters create less cracks, shallower craters, and wider crushed zones beneath the indenter compared with hemispherical indenter in the load range of the present experiment.
- Rock composition and petrology also affect the patterns of craters, crushed zones and fractures to a certain extent. Coarse and crystal rocks, such as granite, reveal rich cracking. Porous rock (e.g. sandstone) gives more distinctly developed single cracks. However, the micro structures of the rocks have less influence on the fracture process and the crack pattern compared with the macro mechanical properties, if the characteristic sizes of the micro structure are smaller than the indenter. This is even clearer when we combine the present experiments with those carried out by Lindqvist (1982) previously.

5 ROCK BEHAVIOUR UNDER COMPRESSION RELATED TO INDENTATION EVENTS

Typical complete stress-strain curves of rock-like material under triaxial compression are shown in Figure 5-1 (Kou et al., 1990). In the figure, the compression is defined as positive. From the triaxial test results it is clear that:

1. The relationship between stress and strain is approximately linear below the stress σ_d, which is defined as the onset of dilatancy. Non-linear volumetric expansion additional to linear compression occurs at a stress higher than σ_d and finally the volumetric strain decreases with increasing stress. The stress will continue to increase until it attains the maximum value, which is defined as limit strength in the context.

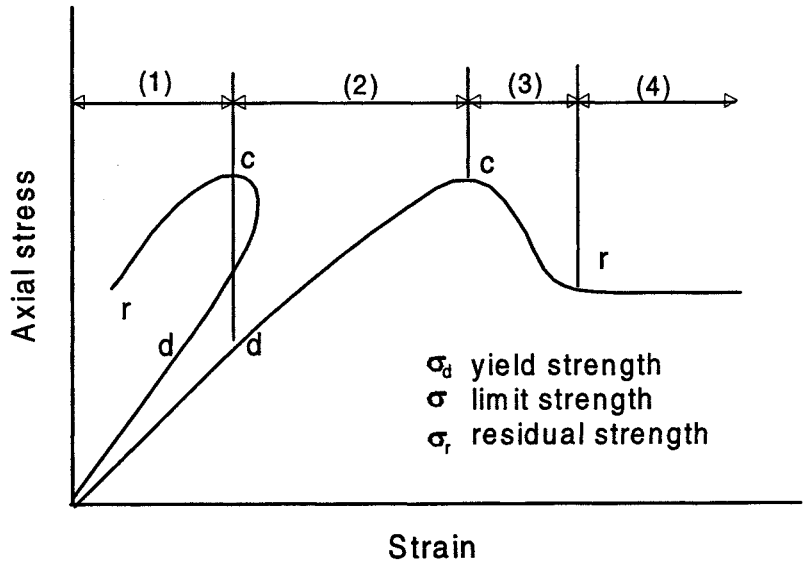

Figure 5-1 *Typical axial stress-axial strain curve (on the right) and axial stress-volumetric strain curve (on the left) of rock-like material under triaxial compression (Kou et al., 1990). (1) Elastic region, (2) initial damage region, (3) post-failure region, (4) shearing and slipping region. The stresses corresponding to the letters d, c, and r in the figure are yield strength (defined as the onset of dilatancy), limit strength, and residual strength, respectively.*

2. Beyond the limit strength, the rock material can still have load-bearing ability, i.e. the rock material cannot be disintegrated without extra force even if the load is reduced to zero. However, beyond the limit strength is an unstable region of the compression test since further deformation can

continue with decreasing load. The descending part of the stress-strain curve is called the post-failure region. The post-failure region corresponds to the localisation of the strain that started from weak points in the test specimen. During the course of strain concentration, a shearing and slipping band is gradually formed. This band is initiated at the weak points and intersects the specimen at a certain angle to its axis. Rock dilatancy continues to develop in this unstable process.

3. The bearing ability of the rock material does not decrease to zero with increased deformation in the post-failure region, but decreases to a certain stress value instead, which symbolizes the end of the rock disintegration in the shearing band. Afterwards, the deformation of the rock specimen is localized mainly in the band and the two parts of the specimen separated by the band are stress-relieved. The stress keeps nearly constant on the axial stress-strain plane with increasing strain, and so does the volumetric strain. The mechanism of deformation in the band is the same as the case with granular material, and so is the dilatation. This stress is defined as residual strength. It is caused by dilatation of the granular rock in the band and friction between the grains. It is obvious that the deformation of the specimen in this case will be mainly due to the relative slipping of the granular rock in the band, and the volumetric strain has therefore no significant variation.

4. Figure 5-2 shows typical stress-strain curves for sandstone in triaxial compression (Bieniawski, 1968). From the figure one may notice that all three strengths increase with increasing confinement. It seems reasonable from the tests (Bieniawski, 1968) to assume that the three strengths, i.e. yield strength, limit strength, and residual strength, have linear relationships with the values of confining stress.

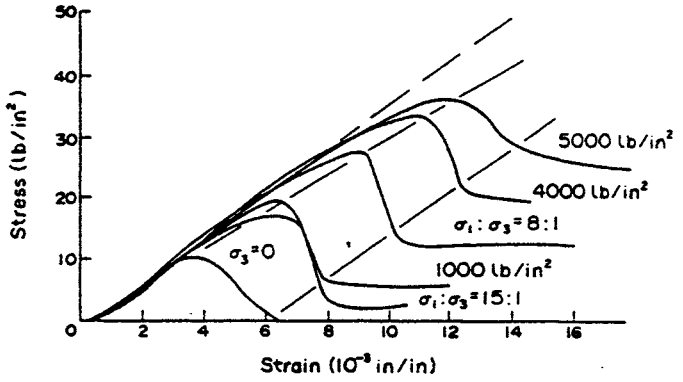

Figure 5-2 *Typical stress-strain curves for sandstone in triaxial compression (Bieniawski, 1968).* $1\ lb/in^2 \approx 6.90\ kPa$

We may now define the physical processes in the indentation related to the stress-strain relationship with some simplification:

1. Rock material behaves elastically in the far-indenter-field, where the main long cracks propagate.
2. The initial damage region is due to the growth and formation of micro cracks during deformation, and it, therefore, corresponds to the cracked zone.
3. In the post-failure region, the damage of the rock material has already amounted to such a level that no extra stress can be sustained by the material, and, therefore, this corresponds to the crushed zone.
4. In the shearing and slipping region the material is disintegrated into granular rock fragments without any cohesion between them. Part of the disintegrated material in the indentation process can be recompacted due to the combined action of the indentation force and the confinement from the wall of the crater. Therefore, this region of the stress-strain curves corresponds to the zone of disintegrated and partly compacted rock fragments.

Among the various fractures, the indentation depth plays an important role in the evaluation of rock excavation efficiency and the improvement of cutter design, the cracked zone may contribute significantly to the hydraulic properties of the EDZ, the length of the radial/median crack defines the boundary of the excavation-disturbed zone, and the side cracks are believed to be the main rock removal fractures in drilling and boring. Indentation depth and the fractures remaining in the rock wall are actually two aspects of one event. They are closely related to each other. We shall focus on discussing them in the rest of this report, so that the mechanisms of rock breakage under indentation load can be definitely explained.

6 NUMERICAL SIMULATION OF CRACKED ZONE

We assume that the indented rock mass is infinite, the rock material is uniform and isotropic, and the indenter is axial symmetric. Under these assumptions, the indentation problem is axisymmetric. The indentation stress field in rocks is dominated by compression. However, macro compression can cause local extension so that the pre-existing micro cracks can extend and result in the above mentioned cracked zone. In order to understand the mechanisms of the formation of the cracked zone, a splitting fracture model will be resorted. The theory of elastic contact developed by Hertz is to be used to determine the stresses caused by a hemispherical indenter. However, the interaction between cracks will simply be neglected.

6.1 SPLITTING FRACTURE MODEL

The splitting fracture model was used by Li and Nordlund, 1993. This model dealt with the extension of a plate-through crack with an initial length of 2 a_0 in plane-strain state, as shown in Figure 6-1a. The extended crack is named as splitting crack or wing crack.

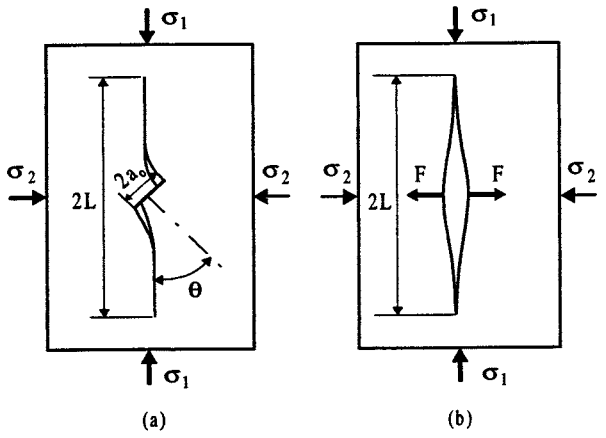

Figure 6-1 *Splitting fracture model: a) the fracture pattern of a single crack under compression, and b) the simplified fracture pattern (Li and Nordlund, 1993)*

The splitting cracks or wing cracks will be initiated at the tips of the originally closed pre-existing cracks and propagate in the direction of major compressive stress. For simplicity, the propagating crack is treated as a tensile fracture driven by a pair of equivalent wedge forces, F, on the two opposing surfaces of the crack (Figure 6-1b). The magnitude of the wedge force F can be expressed by

$$F = a_0 [(\sigma_1 - \sigma_2) f(\theta, \phi) - 2\sigma_2 \cos\theta \tan\phi] \qquad 6\text{-}1$$

where $f(\theta, \phi) = (1 + \cos 2\theta)\ (\sin\theta - \cos\theta \tan\phi)$, σ_1 and σ_2 are the major and minor principal stresses, and compression is defined as positive, θ characterizes the inclination of the pre-existing crack surface, a_0 is the half length of the pre-existing crack, and ϕ the friction angle of the rock material.

For a crack subjected to a wedge force F and a lateral stress σ_2 (Figure 6-2b), the stress intensity factor K_I is given by

$$K_I = \frac{F}{\sqrt{\pi L}} - \sigma_2 \sqrt{\pi L} \qquad 6\text{-}2$$

The wing crack propagates as long as the stress intensity factor is equal to the fracture toughness K_{IC}, which gives the length of the wing crack as

$$L_P = \frac{1}{4\pi} \left[\frac{\sqrt{K_{IC}^2 + 4F\sigma_2} - K_{IC}}{\sigma_2} \right]^2 \qquad 6\text{-}3$$

where L_P is the apparent length of the wing crack.

6.2 HERTZIAN STRESS FIELD

Consider an isotropic, linear elastic half space subjected to normal loading by a spherical indenter of radius R. We assume that

a) the dimension of the contact area is small compared with the dimension of each body,
b) the contact radius a is small compared with the relative radii of curvature of the surfaces, i. e. $a << R$.
c) the contact surface is frictionless, and only a normal pressure is therefore transmitted between them.

Under these assumptions, a mean interaction stress p_0 between the indenter and the rock is introduced, which is defined as

$$p_0 = F / (\pi a^2), \qquad 6\text{-}4$$

where F is the load and a is the radius of the contact circle. The normal contact stress p along the contact surface can be then obtained by using the Hertzian theory (Johnson, 1985)

$$p = \frac{3}{2} p_0 (a^2 - r^2)^{1/2} / a \qquad 6\text{-}5$$

where r is one of the cylindrical co-ordinates with the same origin of the contact circle and its z co-ordinate is perpendicular to the free surface with a positive direction downwards. The normal contact stress p can be also expressed in terms of the maximum contact stress p_m as

$$p = p_m(a^2 - r^2)^{1/2} / a \qquad 6\text{-}6$$

Obviously, $p_m = \frac{3}{2} p_0$. The stresses σ_r, σ_θ and σ_z along the z-axis can be expressed as

$$\frac{\sigma_r}{p_m} = (1+\nu)\left\{1 - (z/a)\tan^{-1}(a/z)\right\} - \frac{1}{2}(1+z^2/a^2)^{-1}, \qquad 6\text{-}7$$

$$\frac{\sigma_r}{p_m} = \frac{\sigma_\theta}{p_m}, \qquad 6\text{-}8$$

and

$$\frac{\sigma_z}{p_m} = (1+z^2/a^2)^{-1}. \qquad 6\text{-}9$$

The principal stress distribution in the rock is shown in Figure 6-2. This figure indicates a drop-shaped zone of compression. The depth of the compressive zone is a little over the contact radius ($1.7a$). Outside the compressive zone, σ_2 and σ_3 turn to be tensile and they drop off rapidly in magnitude compared to σ_1 after they reach to a larger value. The σ_1 is nearly in the radial direction from the origin O (see Figure 6-2) and compressive throughout the field. The stresses on the contact surface are largely compressive and similar in magnitude ($\sigma_1/\sigma_3 \approx 0.8$) but below the surface, the magnitude of σ_1 is much larger than the other two principal stresses.

As explained earlier, the indenter is treated as rigid since its stiffness is much higher than the rocks. The radius of the contact circle can be then calculated using

$$a = \left(\frac{3FR(1-\nu^2)}{4E}\right)^{1/3} \qquad 6\text{-}10$$

where E and ν are Young's Modulus and Poisson's ratio of the rock respectively. The displacement of the indenter in the elastic indentation can be approximated by

$$z = \frac{a^2}{R} \qquad 6\text{-}11$$

However, in our present analysis, only the principal stresses along lines running from the contact center in directions of 0°, 30°, 60° with the vertical direction are used. These stresses were calculated by Morton and Close (1922) with Poisson's ratio of 1/3.

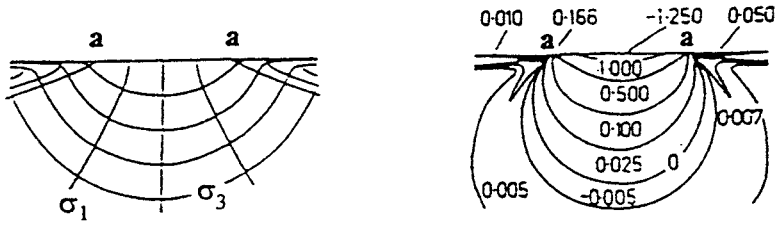

Trajectories of two principal stresses

Contour of σ_3

Figure 6-2 *Contours of the principal stresses in a plane containing the center axis (Lawn, 1968).*

6.3 SIMULATION OF CRACKED ZONE

The cracked zone in Bohus granite and Ekberg marble induced by the above-mentioned indentation experiments will be now analysed numerically by using the splitting model.

6. 3.1 Parameter studies

A number of initial small cracks are set in the Hertzian stress field. The fractures are assumed to develop in an axi-symmetrical plane. The parameters of the pre-existing cracks, i. e. the crack seeds, are the direction of the radial line denoted by ψ, the distance to the indenting center, r, the angle between the normal of the crack surface and the principal compressive stress, θ, and the half length of the crack seed, a_o. These parameters are schematically shown in Figure 6-3. It is expected that in a globally homogeneous rock the pre-existing micro cracks are distributed randomly and no special preferred direction exists. However, we shall focus our analysis on the cracks in the weakest direction. Cracks oriented in other directions or with different lengths can also be calculated in a similar way, which will lead to change in the critical loads or crack developments. In the present analysis, we shall discuss the pre-existing cracks with length $a_0 = 0 \sim 0.3$ mm located in three lines in the directions of $\psi = 0^o$, 30° and 60°, with distances of $r/a = 0, 1, 2, 3$ from the center of the indentation. The rock parameters used in this parameter study are those for Bohus granite and the initial crack length is 0.1 mm unless otherwise stated.

The magnitude of the frictional angle, ϕ, is taken as 30° for the two rocks modelled (Jaeger and Cook, 1979). The direction with maximum effective

shear stress is $\pi/4+\phi/2$. This means the pre-existing cracks with the orientation of $\theta = 60^o$ will be most easily initiated. On the other hand, a crack with orientation of $\theta = 0^o$ will always be suppressed and can never grow.

The fracture parameter K_{IC} in the model is taken from the crack simulation in the uniaxial and biaxial tests for the same type of granite rock presented by Li (1995). The value (1 MPa $m^{1/2}$) for granite is smaller than that measured in the laboratory (Tab. 3-4). Similarly a smaller value of 0.7 MPa $m^{1/2}$ of K_{IC} is used for the marble. The smaller K_{IC} in the model is caused by the relatively small scale of the cracks dealt with (less than a few dozens millimeters). The process zone in present case is much smaller than that of macro cracks, so is the fracture resistance.

The configuration of the splitting wing cracks is shown in Figure 6-3. Notice that only the stresses in the axi-symmetrical plane are counted.

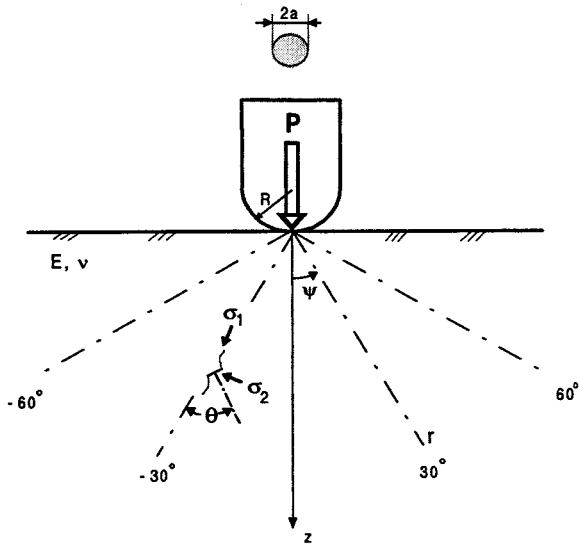

Figure 6-3. *Simulation of splitting cracks in an indentation field*

Figure 6-4 indicates the extension of pre-existing cracks under various loads. These crack seeds were set along different radial lines with different distance from the center point. The three sub-figures are for the distances *r/a* = 1, 2, 3 respectively. The cracks located at the center line ($\psi=0^o$) have longer extension compared to those at the side lines, except at very close distance (Figure 6-4a).

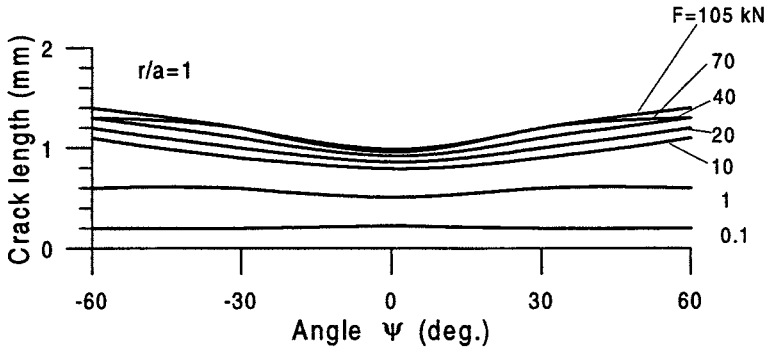

(a)

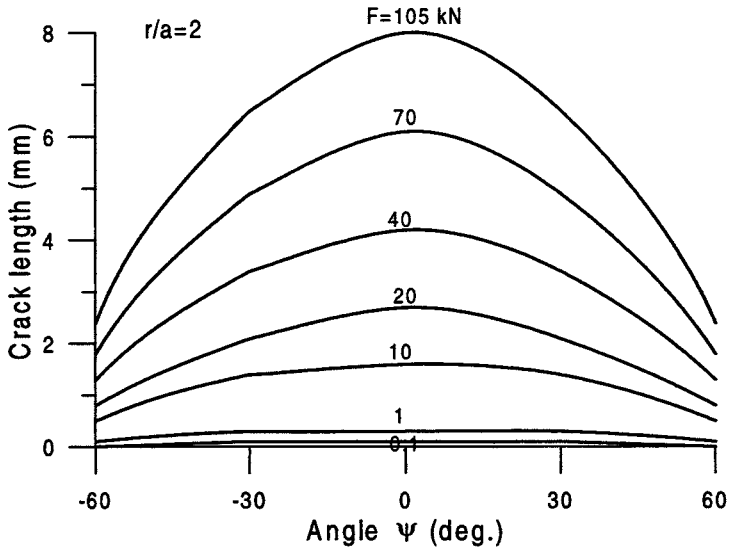

(b)

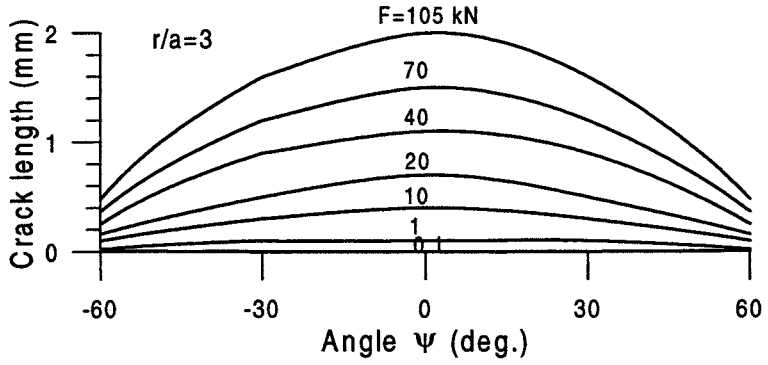

(c)

Figure 6-4 Fracture development along different radial lines and at different distances from the indenting center.

The crack extension under various loads for the crack seeds located along different radial lines at different distances from the center is shown in Figure 6-5. One can see that the cracks located at a distance away from the center have larger development. The variation of crack propagation along each line

is different. The center line varies most. The group curves obtained at different load levels in both Figs. 6-4 and 6-5 follow similar trend with loading: the larger the load, the longer the cracks become.

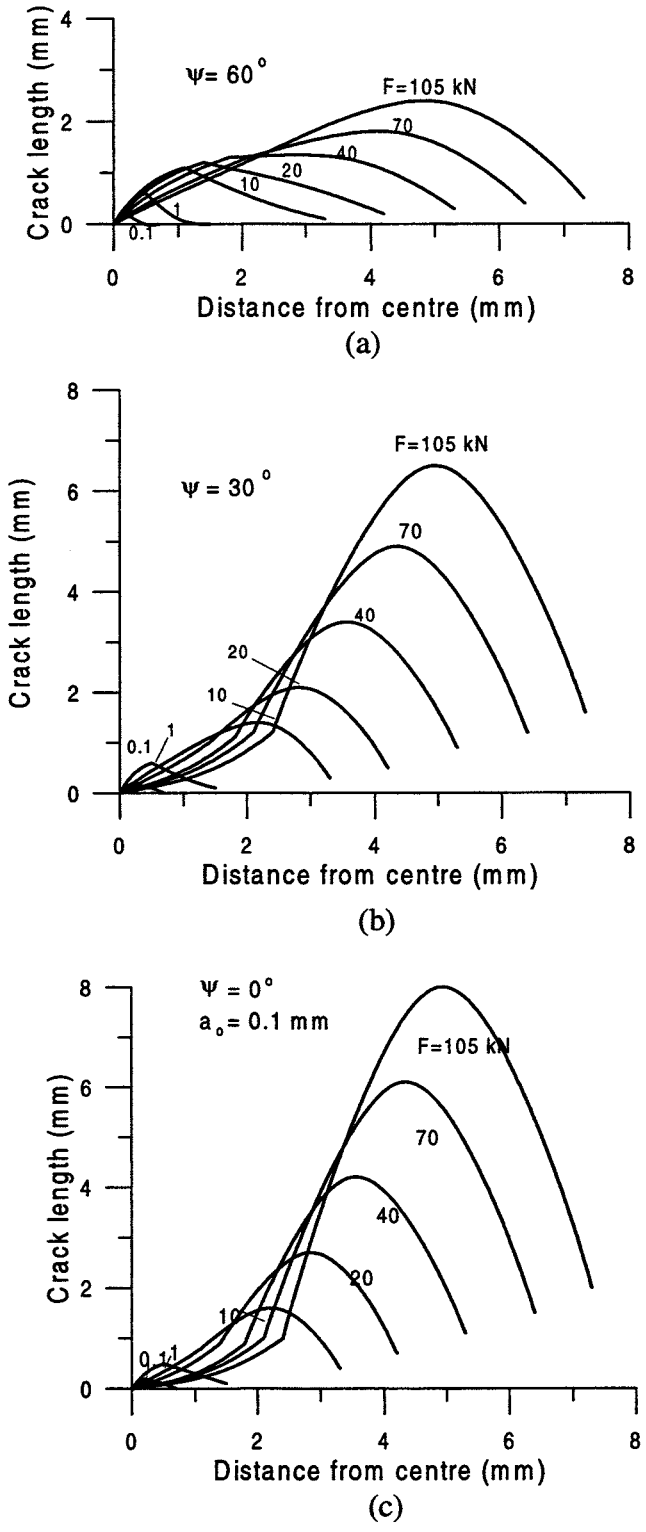

Figure 6-5 Crack development along three radial lines with the directions of $\psi = 0^o$, 30^o and 60^o. The length of crack seeds is 0.1 mm.

Based on the above discussions the cracking patterns can be shown schematically in Figure 6-6. The calculated fracture patterns form a fan-like distribution.

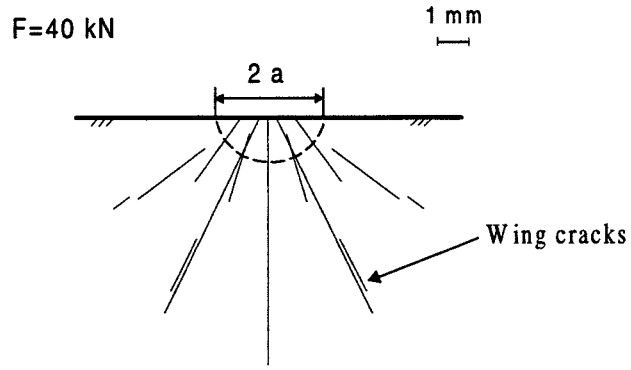

Figure 6-6 *Fracture pattern for some representative cracks*

The longer the pre-existing cracks, the longer the wing cracks grow, which is shown in Figure 6-7. When double the length of original cracks, the crack growth is more than doubled. Therefore size of the original crack has significant effect on the crack development.

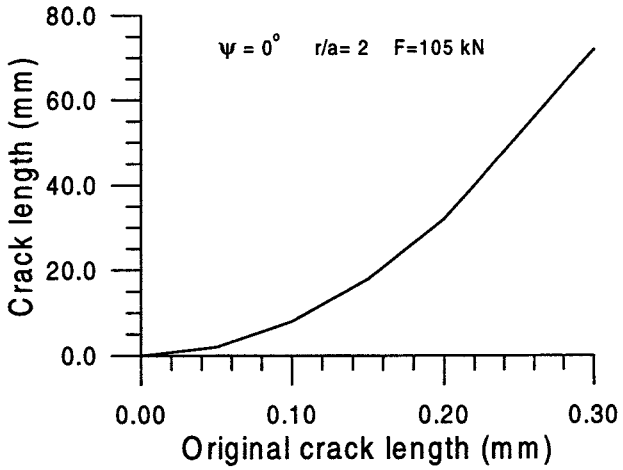

Figure 6-7 *Crack developments versus the length of the pre-existing crack*

The frictional angle ϕ affects the direction of the maximum effective shear stress for initiation of shear crack and the driving force on the crack surface (Eq. 6-1). An increase of ϕ from 30° to 60° will decrease the shear stress by half and the driving force drops to about 20% along the surface of the pre-existing crack with maximum effective shear stress. This in turn will reduce

significantly the crack propagation (Eq. 6-3). On the other hand, a much larger load is needed to drive the splitting crack on a surface with a large friction angle. Hence, a smaller friction angle makes the splitting crack grow more easily.

6.3.2 Numerical simulation of the cracked zone induced by indentation

The maximum depth of the cracked zone observed from the experiment is normally along the center line ($\psi=0^o$). This is in an agreement with the numerical results shown in Figure 6-5.

We may further take both the position of the pre-existing cracks and the extensions of the corresponding cracks into consideration with a similar calculation shown in Figure 6-5. In this way the furthermost position of the possible crack extension from the indentation center can be obtained, which gives the depth of the cracked zone that corresponds to a certain length of the crack seed. A comparison between the depths of the cracked zone in granite and marble numerically calculated by using several different lengths of crack seeds and those obtained by experiments is shown in Figure 6-8. This comparison indicates that the length of the pre-existing micro cracks is in the range of 0.15 to 0.20 mm for granite and 0.10 to 0.12 mm for marble.

Unfortunately, the quantitative data of the micro cracks in Bohus granite and Ekeberg marble are not available and therefore, it is difficult to justify the above results obtained by using the numerical model. However, the lengths of the simulated crack seeds with a range of 200 to 400 μm are within the range of magnitudes observed by Sprunt and Brace (1974) and Kranz (1983). They have shown that for the coarse-grained granite the length of pre-existing cracks is distributed among ten to one thousand μm with an average value of about 100 μm. Our simulated crack seeds are a few times longer than their average value. The lengths of the simulated crack seeds for the marble are relatively large, close to the average grain size of the rock. In addition, one should notice that shorter pre-existing cracks are inhibited once the longer ones start growing and the longer pre-existing cracks therefore play a major role in the specimen failure (Horii and Nemat-Nasser, 1985). Therefore, it sounds reasonable when the simulated crack seeds are larger than the average length of the pre-existing cracks.

The splitting fracture model was formulated in a uniform, compression dominated field and predicts the fracture propagation along the trajectory of the major principal compressive stress. While in the non-uniform indentation stress field, both principal stresses vanish when leaving from the indenting center. For a developing splitting crack, the resistance to fracture at the two tips is not identical. The upper tip near the indenting centre encounters larger confinement. Therefore the upper wing may be under-developed and contrarily the lower wing be over-developed. For simplicity, we consider only the stresses at the middle point of the original crack. This may cause the positions of the predicted cracks to be nearer to the indenter

than in practice. The non-uniform effect is trivial at the initial stage of cracking since the cracks are very short and the stress difference is negligible. The unsymmetric development of the wing crack might be accounted for by shifting the acting point of the wedge force from the middle according to the extent of unsymmetry. The two crack tips will not extend simultaneously. A bias of the splitting force will thus be incurred, and it varies also with fracture propagation. This will entail very complicated calculations.

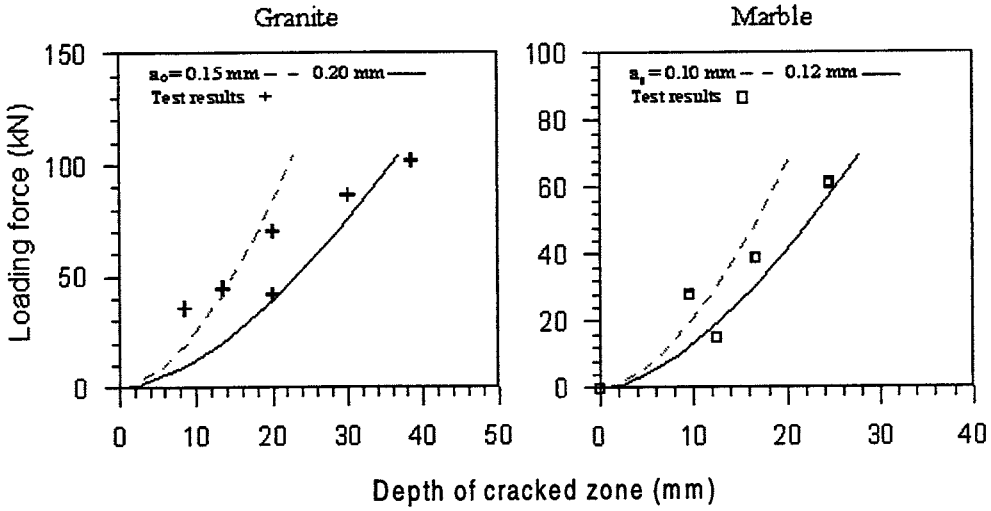

Figure 6-8 *Comparison of the simulated depth of the cracked zones with those obtained by experiment for granite and marble.*

7 NUMERICAL SIMULATION OF SIDE CRACKS

Fully developed side cracks cause chipping in rocks, form a crater and remove the rock. Otherwise they remain below, but close to the surface. Side cracks have a different driving mechanism and follow different cracking patterns compared with the so-called subsurface cracks which form the cracked zone and were discussed in the last chapter. As in the last chapter, the side crack will be discussed by using numerical method.

In general, a crack tip in an ideally linear elastic brittle material can be possibly subjected to a normal stress, an in-plane shear stress, an out-plane shear stress, or any other combination of them. The first three single loading configurations form the three basic distinct fracture modes of crack tip deformation, mode I, mode II and mode III. A combination of mode I and mode II forms a mixed mode I-II. Preliminary analysis of the chipping mechanisms indicate that side crack is a mixed mode fracture I-II. A modified criterion of the energy release rate will be used in this study to count the extension of this kind of fracture. The rock crushing in indentation has significant effect on the initiation and propagation of the side crack. It can not therefore be neglected in the numerical simulation. However, the indentation crushing is very complicated and a cavity model will, therefore, be introduced to simplify the calculation. To facilitate the analysis, this problem is simply treated to be quasi-static under plane strain condition.

7.1 MODIFIED ENERGY CRITERION

According to the energy criterion, a crack will propagate if

$$-\frac{d\Pi}{da} \geq G_c, \qquad 7\text{-}1$$

where Π is the potential energy of a system with a crack of length a and G_c is the critical energy release rate. In numerical analysis the energy release rate is calculated by

$$G = -\frac{\Pi(a+\Delta a) - \Pi(a)}{\Delta a}. \qquad 7\text{-}2$$

Once G reaches G_c the crack will extend. Equation (7-1) means that the energy needed for a unit extension of incremental crack is a material constant independent of the crack length. However, this material constant G_c depends on the crack mode.

A modified energy criterion was suggested by Shen and Stephansson (1994), which was developed to predict mixed mode I-II fracture. They defined a function

$$F(\theta)=\frac{G_I(\theta)}{G_{IC}}+\frac{G_{II}(\theta)}{G_{IIC}} \qquad 7\text{-}3$$

where θ is the direction angle of the fictitious crack made to the face of an initial crack; G_I and G_{II} are the energy release rates obtained by restricting the displacement discontinuity of the "fictitious" crack tip in normal and shear directions, respectively; G_{IC} and G_{IIC} are the critical energy release rates for crack mode I and mode II, respectively. According to their suggestion, once

$$F(\theta)\big|_{\theta=\theta_0,\max} \geq 1 \qquad 7\text{-}4$$

the crack will extend in the direction of maximum F value with a angle of θ_0 made to the face of the initial crack. This modified energy criterion can deal with fractures of either mode I, or mode II, or mixed mode I-II even under compression.

The fracture criterion was implemented in a Boundary Element Method, called Displacement Discontinuity Method (DDM). The program was used in the prediction of wing crack initiation, propagation and even the crack coalescence of multi-wing cracks (Shen, 1993).

7.2 THE DDM PROGRAM COUPLED WITH THE ENERGY CRITERION

The DDM is a very convenient tool in the representation of cracks. In the Boundary Element Method, a relative displacement between the two opposing surfaces is allowed (Crouch, 1976). Like all the techniques in the boundary element method, in DDM a problem is specified and solved in terms of surface values of the field variables of traction and displacement. The solution of the system is therefore very effective and a much shorter calculation time is required compared to the Finite Element Method (FEM), since only the boundary is discretized. The method restricts discretization errors to the boundary of the problem, and ensures fully continuous variation of stress and displacement throughout the medium. As a result of these characteristics, it is best suited for the description of linear material behaviour.

The DDM is based on the analytical solution to the problem of a constant discontinuity in displacement over a finite line segment in a plane of an infinite elastic body. Real boundary is thus discretised into many small elements of this type. We restrict ourselves to discuss the plane strain

problem. The displacement discontinuity, D_i, is defined as the difference in the displacements (u_i) between the two sides of an element (Figure 7-1), i.e.

$$D_s = u_s^- - u_s^+$$
$$D_n = u_n^- - u_n^+ \qquad 7\text{-}5$$

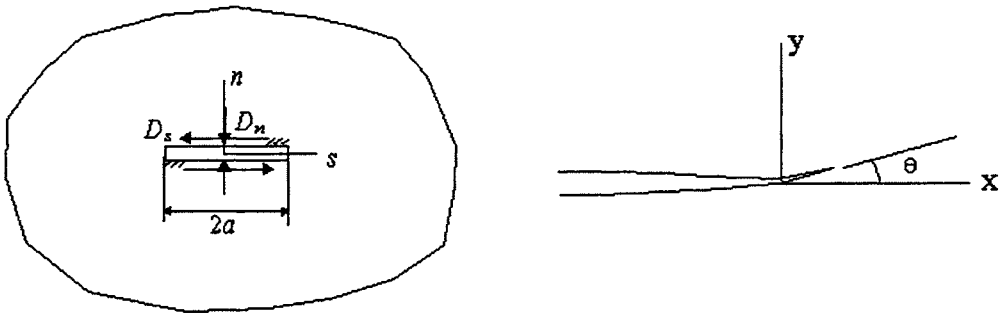

***Figure 7-1** DDM element and fictitious crack tip*

where the subscripts s and n represent shear and normal directions respectively, and plus and minus signs denote the upper and lower surfaces respectively. D_s and D_n are positive as illustrated in Figure 7-1.

Assume there is a single crack element with a length of $2a$, which is located at $y = 0$ and occupies a line segment $|x| \le a$. A constant displacement discontinuity with components of D_s and D_n occurs along the element. The displacements and stresses at an arbitrary point in the body were solved by Crouch and Starfield (1983) as

$$u_x = D_x\left[(1-2\nu)f_{,y} - yf_{,xx}\right] + D_y\left[2(1-\nu)f_{,x} - yf_{,xy}\right]$$
$$u_y = D_x\left[(1-2\nu)f_{,x} - yf_{,xy}\right] + D_y\left[2(1-\nu)f_{,y} - yf_{,yy}\right], \qquad 7\text{-}6$$

and

$$\sigma_{xx} = 2GD_x\left[2f_{,xy} + yf_{,xyy}\right] + 2GD_y\left[f_{,yy} + yf_{,yyy}\right]$$
$$\sigma_{yy} = 2GD_x\left[-yf_{,xyy}\right] + 2GD_y\left[f_{,yy} - yf_{,yyy}\right], \qquad 4\text{-}7$$
$$\sigma_{xy} = 2GD_x\left[f_{,yy} + yf_{,xyy}\right] + 2GD_y\left[-yf_{,yyy}\right]$$

where G is the shear modulus of the elastic material, f is a function of x and y, and

$$f(x,y)=-\frac{1}{4\pi(1-\nu)}\Big[y(\arctan\frac{y}{x-a}-\arctan\frac{y}{x+a})-$$

$$(x-a)\ln\sqrt{[(x-a)^2+y^2]}+(x+a)\ln\sqrt{[(x+a)^2+y^2]}\Big]. \qquad 7\text{-}8$$

The above results, both stress and displacement satisfy, of course, the equations in the mechanics of elasticity. Strains can be calculated by $e_{ij}=(u_{i,j}+u_{j,j})/2$ and the relationship between stress and strain is Hooke's law

$$\sigma_{ij}=2G\left[e_{ij}+\frac{\nu}{1-2\nu}e_{kk}\delta_{ij}\right] \qquad 7\text{-}9$$

where the Kronecker delta is defined as $\delta_{ij}=1$ if $i=j$; $\delta_{ij}=0$ if $i\neq j$. Notice in plane strain we have $e_{zz}=e_{xz}=e_{yz}=0$.

Knowing the analytical solution for a single crack element, the jth element, the numerical solutions are thus obtained for distributed displacement discontinuity on the problem boundary by summing the effects of all the elements (Crouch, 1976). For example, the shear stress and normal stress at the ith boundary element can be expressed as

$$\begin{aligned}\sigma_s^i&=\sum_j\left(A_{ss}^{ij}D_s^j+A_{sn}^{ij}D_n^j\right)\\ \sigma_n^i&=\sum_j\left(A_{ns}^{ij}D_s^j+A_{nn}^{ij}D_n^j\right)\end{aligned} \qquad 7\text{-}10$$

where A_{ss}^{ij}, etc., are the boundary influence coefficients determined by the elastic properties of the material and the geometry of the known boundary elements. Similarly, the shear and normal displacements at the ith boundary element are

$$\begin{aligned}u_s^i&=\sum_j\left(B_{ss}^{ij}D_s^j+B_{sn}^{ij}D_n^j\right)\\ u_n^i&=\sum_j\left(B_{ns}^{ij}D_s^j+B_{nn}^{ij}D_n^j\right)\end{aligned} \qquad 7\text{-}11$$

The B_{ss}^{ij}, etc. in Eq. (7-11) are also the influence coefficients similar to A_{ss}^{ij}, etc. in Eq. (7-10).

Equations (7-10) and (7-11) can be used inversely, i.e. the displacement discontinuity on the crack elements can be calculated for given u or/and σ on the prescribed boundary elements. This makes it possible to solve mixed boundary problems. These two equations can be for a system with N elements

$$\left.\begin{aligned} b_s^i &= \sum_j \left(C_{ss}^{ij} D_s^j + C_{sn}^{ij} D_n^j\right) \\ b_n^i &= \sum_j \left(C_{ns}^{ij} D_s^j + C_{nn}^{ij} D_n^j\right) \end{aligned}\right\} i = 1 \text{ to N} \qquad 7\text{-}12$$

where b^i represents either stress or displacement. Given the boundary values of stresses or displacements, the 2N basic unknowns (D_s and D_n) can be solved and the stresses or displacements at any point in the body are then obtainable by substituting $\left(D_s^i, D_n^i\right)$ into equations similar to Eqs. (7-6) and (7-7) and summing the effects of all the elements.

In addition to the above-mentioned stress or/and displacement boundaries, the boundary conditions for the existing cracks can have three alternatives:

i) for open cracks

$$\sigma_s^i = \sigma_n^i = 0 \qquad 7\text{-}13$$

ii) for closed cracks

$$\begin{aligned} \sigma_s^i &= K_s D_s^i \\ \sigma_n^i &= K_n D_n^i . \end{aligned} \qquad 7\text{-}14$$

iii) for cracks which have sliding along the crack surface

$$\begin{aligned} \left|\sigma_s^i\right| &= \sigma_n^i \tan\phi \\ \sigma_n^i &= K_n D_n^i . \end{aligned} \qquad 7\text{-}15$$

In the above equations K_s and K_n are the shear and normal stiffness of the crack, and ϕ is friction angle of the rock.

The boundary elements can be divided into two categories: one represents the cracks, which is named as fracture elements; the other represents the boundary of the problem, which is named as geometry boundary elements, such as the free surface of the rock specimen and the interface between tool and the rock. In the numerical calculation the system energy is obtained by

$$\Pi(a) = -\frac{1}{2}\sum_{i=1}^{m_1} a^i (\sigma_s^i D_s^i + \sigma_n^i D_n^i) - \frac{1}{2}\sum_{i=m_1+1}^{m_1+m_2} a^i (\sigma_s^i u_s^i + \sigma_n^i u_n^i) \qquad 7\text{-}16$$

where m_1 is the numbers of fracture elements and m_2 is that of the geometry boundary elements; a^i is the length of the ith element. The potential energy of the system Π calculated by Eq. (7-16) is actually also the function of the angle of the fictitious crack θ, and both G_I and G_{II} calculated from Eq. (7-2) by substituting the results obtained from Eq. (7-16), therefore, vary

with the angle θ. For a certain θ the value of F in Eq. (7-3) can reach to its maximum and the crack will then propagate if Eq. (7-4) can be satisfied.

The DDM program coupled with the above mentioned energy criterion (Shen, 1993) carries out the major procedures shown in Figure 7-2.

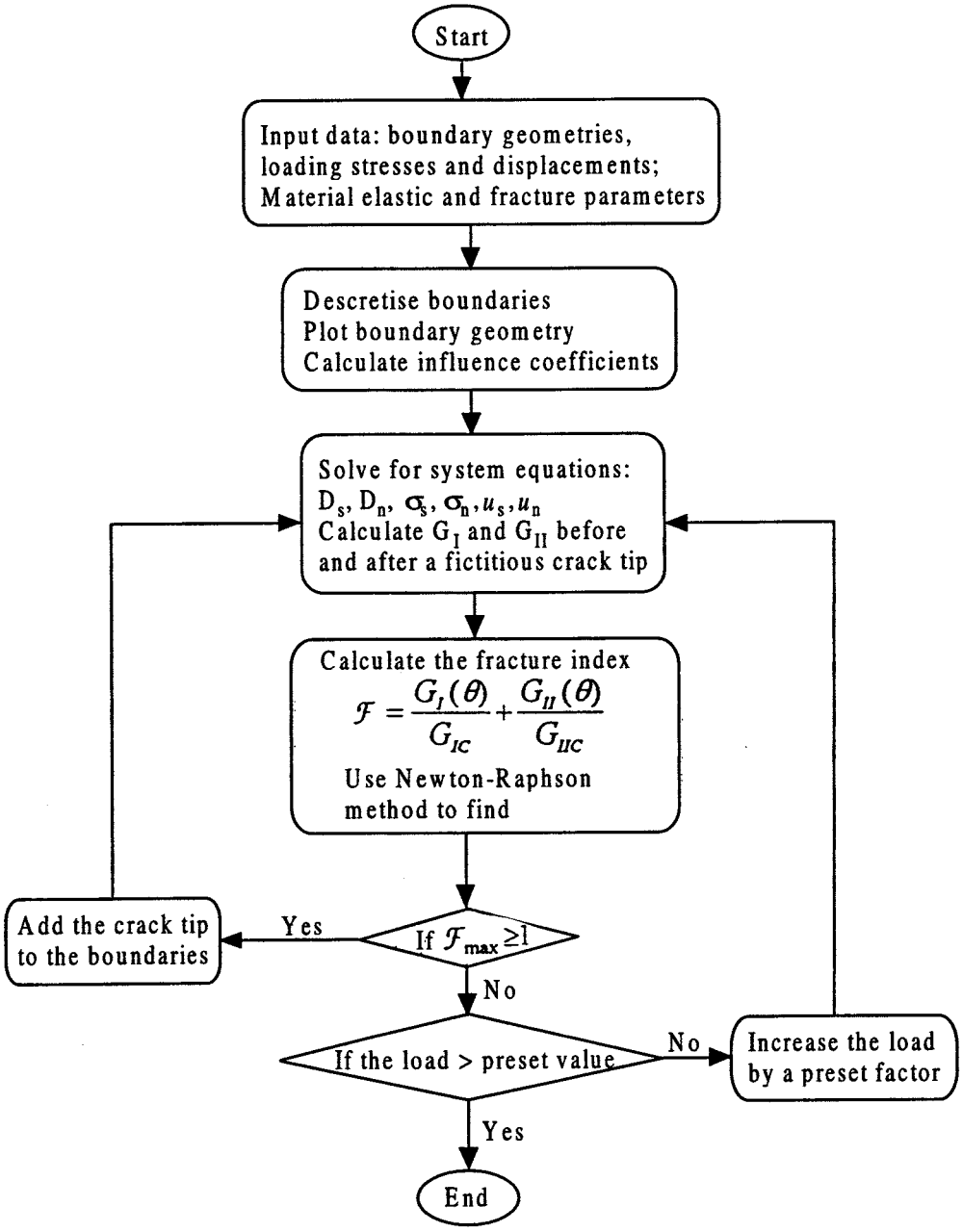

Figure 7-2. *DDM program coupled with the energy criterion.*

7.3 BOUNDARY CONDITIONS

It has been pointed out that the rock directly beneath the indenter is severely damaged or densely cracked accompanied by rock removal and

recompaction of small rock debris. In this so-called crushed zone, the rock is in a post-failure state (Kou et. al., 1994). Evaluation of the nominal contact pressure at the indenter-rock contact area shows a rather constant pressure with increasing load. The pressure established under a truncated indenter is higher than that under a hemispherical indenter for a given rock (Tan, 1996). This indicates that the geometry of the indenter determines the stress distribution and the local contact confinement. The rather constant pressure built up at the indenter-rock contact face indicates that the rock in the neighbourhood becomes yielded and behaves like a plastic material. This kind of material behaviour can not be handled by the Displacement Discontinuity Method.

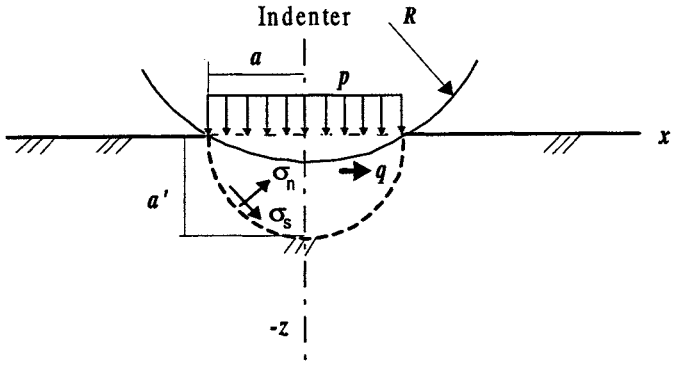

***Figure 7-3**. Expansion cavity model for the crushed rock.*

Similar to Yoffe (1982), a cavity model is introduced to approach this indentation problem including the crushed zone (Figure 7-3). In this model, it is assumed that the crushed rock is encased in the cavity and the material outside is elastic. Uniform vertical pressure p and lateral pressure q are established within the zone due to the plastic deformation. These pressures maintain the zone in a minimum strain energy state (Tan, 1996). This gives a relation between p and q as shown in equation (7-17),

$$q = \frac{vp}{1-v}. \qquad 7\text{-}17$$

The cavity size and shape are estimated from the indentation experimental results.

A nominal indenter-rock contact pressure, which is defined as the load over the projection area of radius a (Figure 7-3), is used to represent the vertical pressure p. The loading force is taken at the concerned points of the force-indenter penetration curves (Figure 7-4). However, the instantaneous penetration depth corresponding to the force is sometimes not a single value due to the load drop induced by the formation of small chips, which can be seen from the force-penetration curve for the hemispherical indenter shown in Figure 7-4. It is assumed that the previous indenter penetration or formation of crater has little influence on the later rock crushing and

therefore the previous penetration accompanied by the load drop is excluded in the calculation of the so-called the instantaneous penetration depth. For instance, the penetration at load point *c* in Figure 7-4 equals the line segment *ab* (≈0.5 mm). This applies just to the first few peaks. By doing so, the nominal contact area for a hemispherical indenter is calculated by

$$A_{Hem} = \pi\left[R^2 - (R-\Delta z)^2\right] \approx 2\pi R\Delta z \qquad 7\text{-}18$$

where Δz is the instantaneous indenter penetration corresponding to the load level; R is the radius of the indenter sphere.

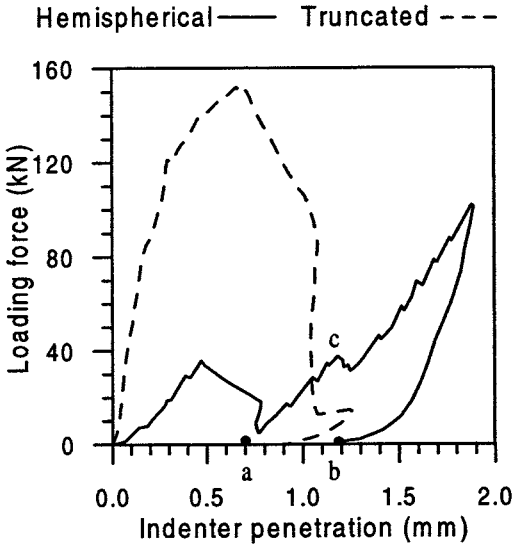

Figure 7-4. *The force-indenter penetration curves for granite indented by hemispherical and truncated indenters.*

Analogously the area for the truncated indenter is approximated by:

$$A_{Tru} = \pi\left[R^2 - (R - z_o - \Delta z)^2\right] \approx 2\pi R(z_o + \Delta z) \qquad 7\text{-}19$$

where z_o is the truncated height, which equals 0.6 mm in our experimental case.

The nominal indenter-rock contact pressure is calculated by

$$p = \frac{F}{A} \qquad 7\text{-}20$$

where, F is the loading force in indentation and A is the area calculated either by Eq. (7-18) for the hemispherical indenter or by Eq. (7-19) for the truncated indenter. The lateral pressure q can be obtained from Eq. (7-17).

The cavity assumes a semi-ellipsoid shape and its vertical radius a' (Figure 7-3) is measured from the photos of discriminated rock slabs cut after indentation test. The equivalent lateral radius a can be calculated from

$$\pi a^2 = A \tag{7-21}$$

once A is known from Eq. (7-18) or (7-19). A shape factor of the semi-ellipsoid is introduced to describe the shape of the semi-ellipsoid, which is defined as $k = a'/a$.

The stress on the flat surface can be transformed to those on the cavity boundary by using

$$\sigma'_{ij} = \alpha_{ik}\alpha_{jl}\sigma_{kl} \tag{7-22}$$

where i, ...l are the direction normal or tangential vectors of the cavity boundary or the flat surfaces, and α is the direction cosine between two vectors indicated by the subscriptions. Thus the normal and tangential stresses on the cavity boundary can be expressed as:

$$\begin{aligned}\sigma_{nn} = \sigma_n &= -q\cos^2(n\hat{}x) - p\cos^2(n\hat{}z) \\ &= -\frac{p\sin^2\theta}{\sin^2\theta + k^2\cos^2\theta} - \frac{qk^2\cos^2\theta}{\sin^2\theta + k^2\cos^2\theta}\end{aligned} \tag{7-23}$$

and

$$\begin{aligned}\sigma_{ns} = \sigma_s &= -q\cos(n\hat{}x)\cos(t\hat{}x) - p\cos(n\hat{}z)\cos(t\hat{}z) \\ &= \frac{(p-q)k\sin\theta\cos\theta}{\sin^2\theta + k^2\cos^2\theta}\end{aligned} \tag{7-24}$$

where σ_n and σ_s are the normal and shear stresses acting on the cavity boundary; θ is the polar angle of a point on the boundary curve; t and n are the unit vectors tangential and normal to the cavity boundary; $n\hat{}x$, $n\hat{}z$, etc. are the angles between the unit vectors on the boundary and the axes of the coordinates. Equations (7-23) and (7-24) provide the boundary stresses σ_n and σ_s on the cavity boundary once we know the parameters p, q and k. However, in the indentation fracture simulation, part of the boundary, where the rock specimen has no contact with the tool, is free from stress, and the boundary conditions are

$$\sigma_s = \sigma_n = 0. \tag{7-25}$$

Up to this stage we have got all the boundary conditions (Eqs. 23 to 25) for the indentation problem. The basic material properties involved are Young's modulus E, Poisson's ratio ν, the critical energy release rates, G_{IC} and G_{IIC}, the crack stiffness K_s and K_n, and the friction angle ϕ of the rock. The

material properties of the indenter will not appear in the calculation explicitly since it is assumed as rigid.

7.4 PARAMETER TESTS FOR SIDE CRACK SIMULATION

7.4.1 Discretising of the indentation boundary

To find a suitable way to discretise the indentation boundary of both free and loading surfaces, numerical tests were made using the DDM program. The classical solution of a uniform pressure on a semi-infinite body in plane strain is used as a standard for comparison (Johnson, 1985). The vertical stress along the center axis is written as

$$\sigma_z = -\frac{2p}{\pi}\left\{\tan^{-1}\frac{z}{a} + \frac{az}{a^2+z^2}\right\} \qquad 7\text{-}26$$

Four sets of boundary arrangements were made by using different discretising sizes for the loading and free boundaries whilst keeping the total widths of loading at 2 units and the free boundary by the two sides at 9 units. The stress was calculated for the four cases and is presented graphically in Figure 7-5.

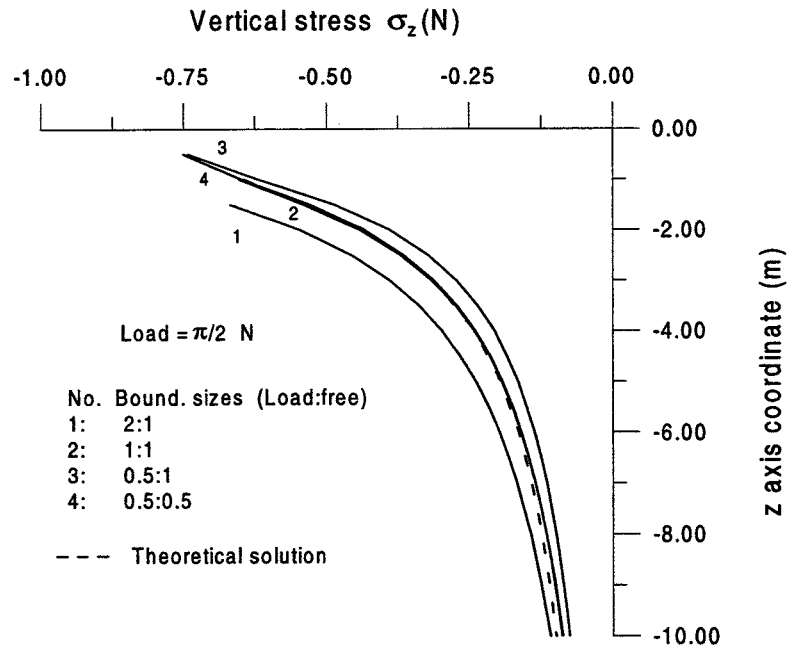

Figure 7-5. *Effect of boundary discretising on the indentation stress.*

The comparison between the results obtained by numerical simulation with varying boundary arrangements and the classic solution of this problem indicates that better accuracy is achieved using boundary arrangements 2

and 4. The results also indicate that no great difference when using uniform discretising of different boundary lengths in the two cases (see Figure 5). Therefore good accuracy can be obtained by using uniform elements.

For the cavity boundary, another calculation was made for the stresses around a hole in an infinite space subjected to a uniform pressure on its wall. The hole was divided into 24 elements, which is comparable to our cavity with 12 elements. The numerical solutions of the stresses are shown graphically against the theoretical solutions in Figure 7-6. It is seen that a good agreement is obtained between the analytical and the numerical calculations. Therefore it is reasonable to use this element arrangement for the cavity boundary.

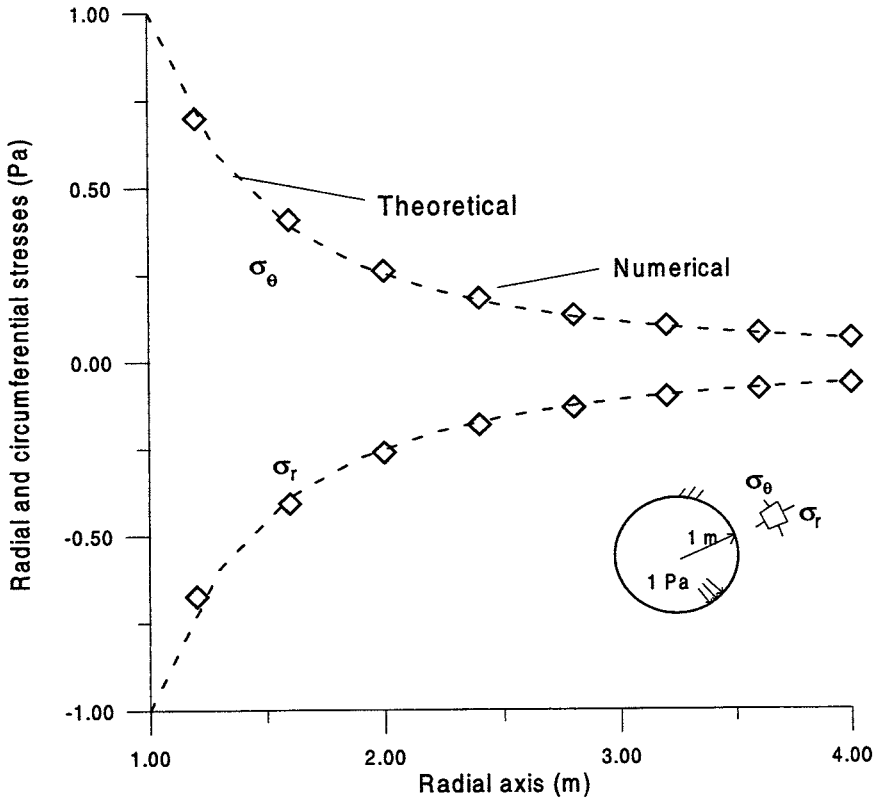

Figure 4-6. *Comparison of stresses between analytical solution and numerical calculation.*

7.4.2 Fracture model parameters

The modified *G*-criterion deals with both mechanisms of tensile and shear fracture. In the criterion it is proposed that the critical energy release rate differs between tensile and shear cracking. G_{IC} represents the energy release rate for mode I and G_{IIC} for mode II. G_{IC} is equivalent to the commonly adopted G_C which is usually obtained at mode I. G_{IIC} is not at present available from standard tests. There are many technical difficulties in producing pure shear cracking (Xu et al. 1996) and thus obtaining real G_{IIC}. One way to determine it is to carry out back simulation and calibration of

known shear fractures (Shen, 1993). Others have attempted to measure it from the shear stress-strain curve with generation of shear band in tri-axial tests (Hakami and Stephansson, 1990). In our study, the former is used. From the formula of the criterion (Eq. 7-3) we can see that different choices of G_{IIC}/G_{IC} may change the quantity F and hence the direction of crack propagation. The cracking mode may also be varied. It is therefore important to calibrate the material parameters for the material under the actual loading situation.

A sensitivity study of the ratio, G_{IIC}/G_{IC}, on crack propagation in uni-axial loading was carried out by Shen (1993). This showed that the cracking mode is affected by G_{IIC}/G_{IC} only when the ratio is in a low range of about 1 to 5. Above this range, G_{IIC}/G_{IC} has no influence on the crack mode or the priority for shear or tensile cracking. The stresses and orientation of the initial crack play a crucial role. Based on back calculation of shear cracks and other indirect results (Hakami and Stephansson, 1990; Li, 1991), it is expected that G_{IIC}/G_{IC} will generally be of the order of magnitude of 100. In the parameter test for our indentation situation, G_{IIC}/G_{IC} is varied from 10 to over 200 (Figure 7-7). It was observed that the side crack trajectories and their propagation mechanisms were not affected over this wide range of G_{IIC}/G_{IC}. Similar results have been obtained in the calculation of tensile fracture (Tan and Shen, 1995).

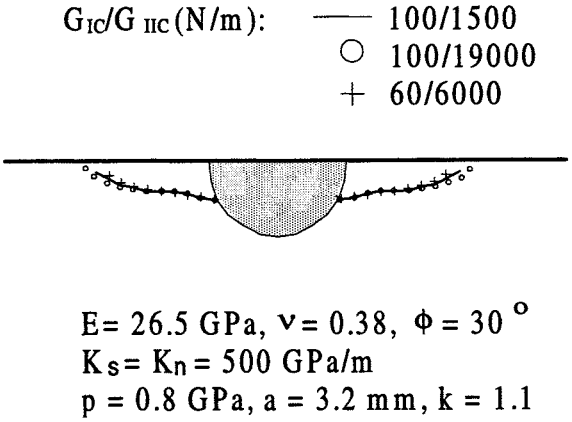

Figure 7-7. *Side crack propagation with various G_{IC}/G_{IIC}.*

The parameters, K_s and K_n, defined as the loads needed for achieving unit joint or crack normal closure and shear displacement respectively, are used for describing joint or crack behaviour. Laboratory shear tests can provide K_s and K_n behaviour curves. A general pattern is that K_n increases with loading and tends to infinity at high levels of load. K_s remains rather constant with loading, but becomes zero when global sliding occurs and the friction law is in effect. It has been reported that K_s and K_n can vary in a wide range from 10^5 to 10^{12} Pa/m depending on filling material in-between the joint and the roughness of the crack surfaces. It is generally understood that the quantity of stiffness is inversely proportional to the dimension of the

rock joint/fracture (Hökmark and Pusch, 1992). On the scale of indentation fractures, an order of magnitude of 10^2 to 10^3 GPa/m is reasonable. In DDM fracture modelling, a linear force-displacement model is used and a constant stiffness applied. This describes an average performance of the crack interface at certain load levels and crack scale. Proper values are required for the actual load and crack conditions. In the DDM crack model, K_s acts only during elastic contact; when the crack is open, zero shear force results; when the crack is sliding, the friction law governs the shear stress response (section 7.2). K_n affects the normal stress on the crack surface during both crack closure and sliding and the shear stress during crack sliding. When the crack is open, it becomes zero.

In our parameter tests, K_s and K_n were varied from 50 to 1500 GPa/m and the crack trajectories deviate a little from each other after some extension (Figure 7-8). It can be seen that with a large stiffness, the crack tends to follow a slightly curved path in the indentation field. With a small stiffness, the crack propagates further in the subsurface. The variation in trajectory becomes obvious only when a large change in fracture stiffness is introduced. This change in fracture stiffness causes a local change in the stresses near the crack, which in turn affects the crack trajectory. In the simulation of wing cracks, a large fracture stiffness makes the wing crack straighter and turns earlier in the direction of the compressive load (Shen, 1993). In the rock indentation situation, the trajectory differences become more evident with further crack developments; possibly due to the different loading and boundary situations. The former is under uniform loading from the far boundary, while the loading and free boundaries are very close to the cracks in the latter. Based on this test we shall use $K_n = K_s = 500$ *GPa/m* in our calculation.

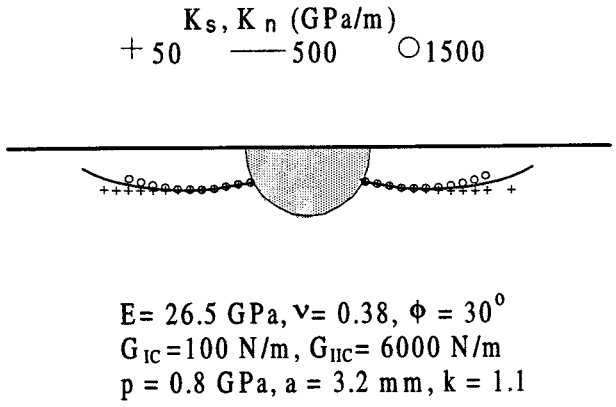

Figure 7-8. *Side crack propagation with various K_s/K_n.*

7.4.3 The friction angle

In the DDM model, the friction angle, ϕ, affects the sliding state of the crack surface. A larger ϕ causes high shear stresses and hence high resistance to

sliding. A parameter study of ϕ in uniaxial loading (Shen, 1993) has shown that this parameter does not greatly affect the crack mode, except when the crack orientation in relation to the direction of the compressive stress is close to ϕ, in which case the crack may easily grow in shear mode. Therefore, with different friction angles, cracks with certain orientations can be subjected to trajectory variations.

7.4.4 Cavity model parameters

In the cavity model, the rock within the cavity is subjected to plastic deformation. The ratio *q/p* is an indication of the lateral expansion of the yielded rock, which causes side crack in the surrounding rock. The crack trajectories are turned upward when *q/p* is varied from 0.5 to 1 (Figure 7-9).

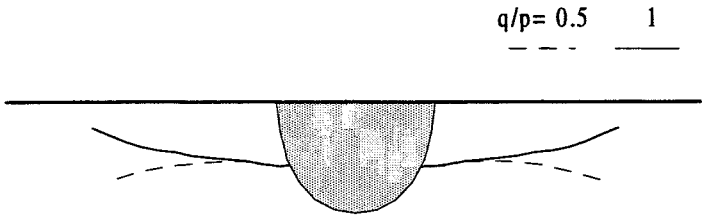

E= 26.5 GPa, Φ= 30°
$K_s = K_n$= 500 GPa/m
G_{IC}=100 N/m, G_{IIC}= 1000 N/m
p = 0.8 GPa, a = 4.5 mm, k = 1.4

Figure 7-9. *Side crack propagation with two different q/p ratios.*

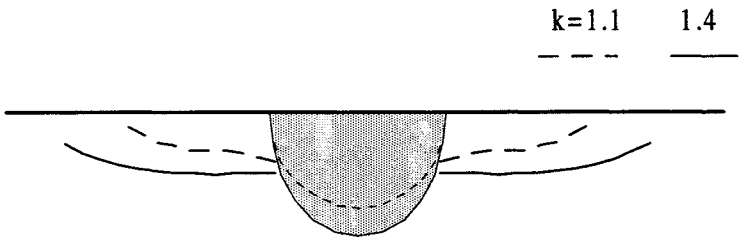

E= 26.5 GPa, ν= 0.33, Φ= 30°
$K_s = K_n$= 500 GPa/m
G_{IC}=100 N/m, G_{IIC}= 1000 N/m
p = 0.8 GPa, a = 4.5 mm

Figure 7-10. *Side crack propagation with two different cavity shapes.*

A similar change occurs when the cavity shape factor, *k*, is increased, i. e. a deepening of the cavity with its lateral radius unchanged. The depth of the initial crack that can form side crack is also increased when increasing the

cavity depth (Figure 7-10). The pressure ratio and the cavity shape factor are two parameters reflecting the rock behaviours during the post failure stage under the action of the indenter contact stresses and the confinement which is determined by the indenter shape and size, loading force and rock type.

7.4.5 Initial crack settings in the indentation field

In the crack simulation, initial cracks are assigned as seed cracks for starting the cracking. Slant or flat initial cracks are introduced at a certain depth close to the cavity boundary. The selection of these is based on experimental observations (Lindqvist et al. 1994). Simulated crack patterns vary with changing initial crack positions (Figure 7-11) and the energy release rate associated with the crack propagation varies considerably. Crack seeds lying in a middle position in Figure 7-11 with large energy release are liable to generate side cracks. The locations favouring side crack initiation are shifted a little upward or downward when the cavity shape and expansion pressure are changed (e.g. Figure 7-10). Therefore both the stress and initial crack affect crack propagation. Side crack trajectories are expected to vary somewhat since the micro cracks in the rock are distributed with different positions and orientations. This leads to a scattered pattern of side crack development and may be the reason why the side crack trajectories never repeat themselves under identical loading conditions in real indentation tests.

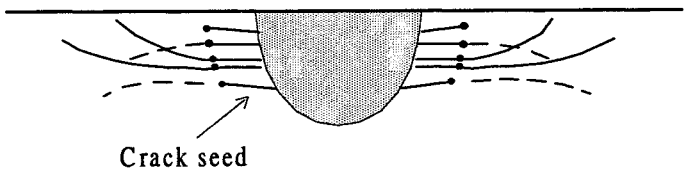

$E = 26.5$ GPa, $\nu = 0.33$, $\phi = 30^{\circ}$
$K_s = K_n = 500$ GPa/m
$G_{IC} = 100$ N/m, $G_{IIC} = 1000$ N/m
$p = 0.8$ GPa, $a = 4.5$ mm, $k = 1.4$

Figure 7-11. *Side crack propagation with different initial crack positions.*

The crack mode varies in the indentation field. The initial cracks with the positions shown in Figure 7-12 are driven by tension instead of shear as was the case in the previous examples. The crack surfaces are almost perpendicular to the direction of the principal tensile stress induced primarily by indentation loading and secondarily by propagation of existing cracks. Even some original shear cracks may become tensile at later stages of their development. Initial cracks in other than the above-discussed directions or far from the indenting point may not extend at all. Therefore, the mode of the propagating cracks is determined by both the local stresses and the crack tip orientation in relation to the stress field.

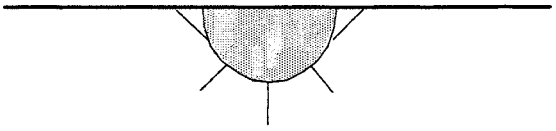

E= 26.5 GPa, ν = 0.38, ϕ= 30°
$K_s = K_n$ = 500 GPa/m
G_{IC} =100 N/m, G_{IIC} = 6000 N/m
p = 0.8 GPa, a = 3.2 mm, k = 1.1

Figure 7-12. *Side crack propagation with tensile mechanism.*

To facilitate numerical calculations, an initial crack of finite length (2 to 4 mm) is used. This length is, in general, larger than the mean size of mineral grains and internal flaws in rock. Numerical tests have been made with different initial crack lengths (Figure 7-13). It can be seen from Figure 7-13 that the variation of the initial crack length within a certain range does not much influence side crack trajectories. However, if the initial crack, which is often modelled as a straight line, is too long, the trajectories will definitely be different from those induced by shorter seeds. The former causes a flater crack and the later develops into a curved crack. Based on numerical trials, a length of three elements was selected and used in the simulations.

Number of elements
○ 2 —— 3 + 4

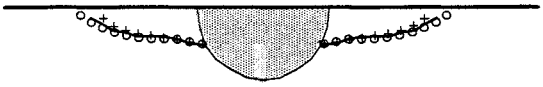

E= 26.5 GPa, ν = 0.38, ϕ= 30°
$K_s = K_n$ = 500 GPa/m
G_{IC} =100 N/m, G_{IIC} = 6000 N/m
p = 0.8 GPa, a = 3.2 mm, k = 1.1

Figure 7-13. *Initial side crack length and crack propagation.*

7.5 SIMULATION OF SIDE CRACKS INDUCED BY INDENTATION

The side/chipping cracks in granite, marble and sandstone with hemispherical and truncated indenters have been simulated. The boundary elements are arranged in the manner described in section 7.4. The cavity model is implemented in the DDM program for simulation of the crushed

zone. The basic rock properties used were given in Table 3-4 and the model parameters are listed in Table 7-1.

Table 7-1. Rock and model parameters used in side crack simulations

Case	Rock	Indenter	F (kN)	p (GPa)	a (mm)	k	ϕ (deg.)	G_{IC} (J/m^2)	G_{IIC} (J/m^2)
a	Sandstone	Hemispherical	25	0.4	4.5	1.1	30	110	6000
b		Truncated	76	0.5	7.0	1.4			
c	Marble	Hemispherical	60	0.5	6.2	0.9	30	40	1500
d		Truncated	103	0.9	6.0	1.2			
e	Granite	Hemispherical	102	0.9	6.0	0.8	30	100	20000
f		Truncated	150	1.4	5.8	1.1			

As explained in 7.3, the indentation parameters p and a are calculated from the peak load in the curve of load-indenter penetration. k is based on measurements of the crushed zone from photos of the slabs. The fracture stiffness, K_s and K_n, are based on previous experience (Shen, 1993; Crouch and Starfield, 1983). Other elastic properties of rock are obtained from the standard laboratory tests described in Table 3-4.

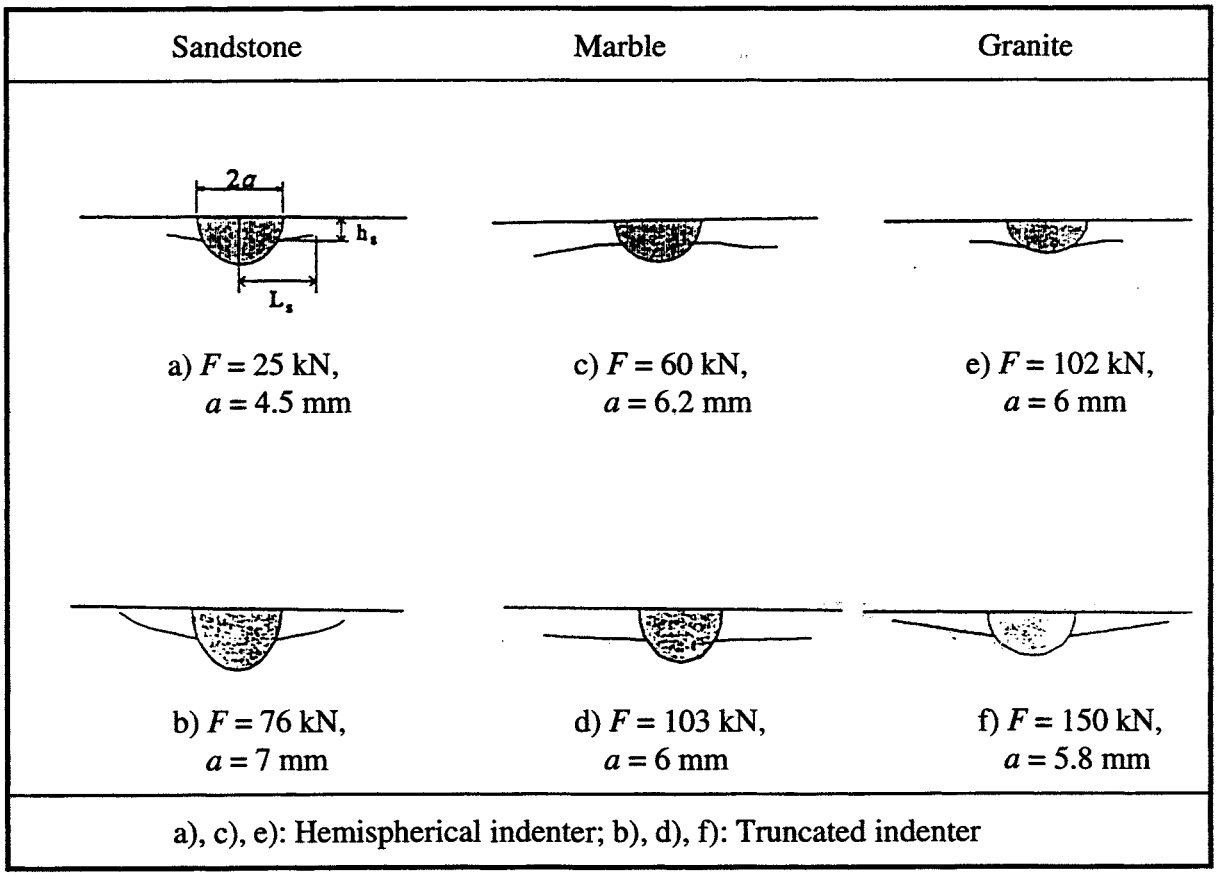

Figure 7-14. *Side cracks in sandstone, marble and granite — simulation results.*

In the crack simulation using the DDM model, a number of initial cracks are introduced around the cavity. The cracks, which grow roughly parallel to or intersect with the surface and cause large energy release, are considered as side cracks. The simulated cracks are shown in Figure 7-14 and the crack lengths are listed in Table 7-2. Comparison of the simulated cracks with those from indentation experiments (Figure 3-9) indicates that the simulated cracks follow roughly similar patterns to the experimental ones. The simulations indicate that propagation of the shear cracks are in general stable but not the tensile cracks. Tensile cracks cause an energy release much greater than the critical value.

The granite is rich in micro cracks. The propagation of a major shear crack in granite induces many side branches, which consumes extra energy and inhibits the development of the major crack. The aperture of the crack surface may also differ. A much smaller load is needed to generate side cracks in marble. The back-calculated G_{IIC} for the marble is much smaller than that for the granite.

The curved trajectories of the side cracks result from the local stresses around the crack tip due to the crack development. The indentation stress field is a little different from that without the cracks. For some cases, tensile stress is developed at the crack tip, as the two surfaces of the side crack separate from each other. These results were also observed in real rock indentation tests (Lindqvist et al. 1984). Chipping can therefore involve both shear and tensile mechanisms.

Table 7-2. Length of side cracks from simulation and indentation tests

Case	Indentation experiment (mm)		DDM simulation (mm)	
	L_s	h_s	L_s	h_s
a	7.3	1.5	7.7	2.5
b	16.0	4.0	18.5	4.9
c	25	7.0	21	3.1
d	23	4.5	19	4.0
e	11.0	2.0	11.0	3.7
f	16.5	3.5	14.0	3.5

7.6 DISCUSSIONS

7.6.1 Crushed zone and the cavity model

Unlike a hemispherical indenter, cylindrical and truncated indenters have a flat surface at the head. The contact situation is different and a stiff force-indenter penetration behaviour is observed. The peak load and the

corresponding contact pressure with major chipping are considerably higher. Therefore it is the tool geometry that characterises the three-dimensional contact and loading state. The development of rock yielding and crushing beneath indenters of different shapes will therefore differ to a certain extent.

A convex shaped zone with crushed or severely damaged rock is produced by all these indenters. In the crushed zone, micro-cracking, shear and slip occur along and within the mineral grains. A whitish zone with dense, crossed fissures is observed in photos of sectioned slabs. Ductile behaviour is observed under a hemispherical indenter where stable nominal contact pressure is maintained. The formation of the crushed zone starts at a rather small load and the zone extends gradually, maintaining a semi-spherical shape. The situation for the flat bottomed indenters is a little more complex. A large confinement is formed and the development of rock crushing commences mainly at the corner of the indenter. Cracking and rock crushing extend gradually towards the side and downward and finally connect below the indenter. A cone shaped zone immediately beneath the indenter is much less damaged compared to the crushed rock surrounding it. This gradual change in the shape of the crushed zone for this type of indenter may require some adjustment of the cavity parameter in the crack simulation.

Major chipping or cracking interrupts loading as well as development of the crushed zone. The contact pressure then rebuilds, resulting in redistribution and compaction of loose particles (Lundqvist, 1981). The next loading may have a larger peak load due to greater confinement or higher cracking resistance at a deeper location. Rock yielding and crushing are very localised.

It is noted that the formation of small chips and cratering around the indenter head may cause incomplete indenter-rock contact. The estimated nominal contact pressure will therefore be a little smaller than the real pressure. Since the exact contact area is very difficult to measure, this calculation provides an approximate result.

The calculation of rock indentation stresses under the influence of a crushed zone is very difficult because the shape and size of the zone are not known a priori. Numerical methods, such as Finite Element Method, can be employed to calculate the evolution of stress and strain with the extension of the crushed zone provided that the total stress and strain relationships are specified. A simplified approach is to employ a cavity model. This has been used extensively in the indentation study of metals and ceramics (Chiang et al. 1982; and Johnson, 1985). The cavity model proposed by Yoffe (1982) for brittle material specifies the stress response in the crushed zone. The relationship between the size and shape of the crushed zone and the contact loading stress is not available and experimental or empirical results have to be used. In our present simulation, these parameter values are taken from indentation experiments. Due to the limited number of tests, formulae relating these parameters are not established and their values may be

subjected to some errors. Further work is needed in order to establish and calibrate these relationships more accurately.

7.6.2 Side crack simulation and the fracture model

For the F-criterion, G_{IIC} is the critical energy release rate when a unit surface is generated under shear deformation and can be reckoned as a material property parameter in fracture. The ratio, G_{IIC}/G_{IC}, depends upon the rock dislocation behaviour (Shen, 1993); G_{IIC} is about two orders higher than G_{IC} (Cherepanov, 1979 and Li, 1991). This can be explained by the fact that macro shear cracks in the rock may contain many more micro cracks scattered in a band around it compared with tensile cracks. Therefore we expect that more energy will be spent due to friction and deformation around the fracture surfaces. Shear fracture is hardly seen in some materials, such as ceramics, metals and cement, but is pronounced in brittle and porous rock (Jung, et al., 1992 and Shen, 1993). So far there is no standard experimental method for determining G_{IIC}. Although new methods have been proposed to generate pure shear cracks, the shear fracture toughness has not yet been obtained (Luong, 1992). An indirect way to obtain G_{IIC} can be to calculate the energy spent in the formation of a shear band in the tri-axial tests (Hakami and Stephansson, 1990). The value of G_{IIC} was in the range of 10,000 to 80,000 J/m^2 at a confinement pressure of 20 to 80 MPa in granite rock. Whilst this method might not be very accurate in creating a pure shear band and thus in calculating the energy, it does however provide a rough estimate of G_{IIC}. In our side crack simulations, G_{IIC} was obtained through back calculation from side cracks with different loading forces and indenter types. In the course of back calculation, a wide range of G_{IIC} values were tested. For instance, the values used in sandstone ranged from 1 kJ/m^2 to over 10 kJ/m^2. No distinct change in the trajectories of the side cracks occurred. The same results were found for the granite. Therefore, side crack development is not affected by the wide changes in G_{IIC}. It can be seen that the magnitudes of G_{IIC} of granite obtained from our back calculations are of the same order as those reported by Hakami and Stephansson (1990).

The plane strain assumption and two-dimensional fracture model have been used in the indentation fracture simulation. In the rock indentation and fragmentation, the cracks and chips are formed in an axi-symmetric or three-dimensional stress situation. Fracture mechanics models for axi-symmetric and three dimensional situations are desired in order to study more closely the rock indentation and fragmentation problems.

7.6.3 Possibility of simulating median and radial cracks and the cracks induced by TBM using the present numerical model

Some attempts have been made to simulate the median crack by introducing a seed crack directly below the cavity. The crack propagated downward roughly along the center axis, but kept on growing. This infinite growth

suggests that the static fracture model with control of either load or displacement could not closely describe the process of the median crack and the present model is, therefore, not suitable for simulating this type of cracks.

Unlike the side and median cracks, radial cracks initiate next to the indenter and intersect with the free surface. With growth of the crack, the depth of the crack front increases at the beginning and then decreases gradually to zero. Similar to median cracks, radial cracks are driven by tensile stresses on the horizontal plane and also exhibit some unstable features. This pattern of crack development and the stress condition deviate very much from the crack shape in the plane strain state and could hence not be properly simulated with the present 2-D fracture model.

In an underground tunnel, the working face includes both the tunnel front and the side wall. A front cutter may mostly act on a ridge and generate grooves, while the side cutters break rock in an inclined position. This makes the loading and cracking situation somewhat different from those modelled in the laboratory. However, it is believed that the same mechanisms of fracture are at work. The model presented here has the flexibility to specify other geometry boundaries apart from a flat boundary.

8 FORMULATION OF MODELS FOR INDENTATION DEPTH AND RADIAL/MEDIAN CRACKS

We shall discuss the indentation depths and the lengths of the radial/median cracks in various rock types caused by various kinds of indenter in this chapter. Instead of numerical methods used in the previous discussion on cracked zone and side cracks, which met difficulty in analysing the median and radial cracks as explained earlier, similarity analysis will be resorted to. The discussion will start with a short explanation of the understanding of the indentation mechanisms, which constitutes the basis for the simplification of the physical problem.

An indenter penetrates rock by expending a great amount of energy in crushing the rock. The force displacement response is therefore closely related to the fractures in the rock induced by the indenter (Figure 4-1). The increasing load causes the closure of the pre-existing flaws in the rock at the very beginning, followed by elastic deformation of the rock surface, and the formation of crushed and cracked zones. In this stage, movement and dilatation of the rock fragments in the crushed zone are restrained by the surrounding intact rock. In order to break the rock, the force must be further increased. This causes intense comminution of the rock fragments and the comminuted rock in the crushed zone will then be partly recompacted under the combined action of the lateral confinement and the normal stress caused by the indenter. The moving and dilating tendency of rock fragments in the crushed and cracked zones will push the surrounding rock outwards and up and therefore results in radial, median and side cracks. During the process of rock fracturing the indenter will gradually penetrate into the rock. When the side cracks reach the rock surface, the surrounding rock which offered the lateral confinement at the earlier stage, together with part of the rock underneath the indenter, will quickly move away forming the so-called chips. At that moment the strain energy stored in the rock will convert into the kinetic energy of the rock chips, so that they move away at a rather high speed. The movement of the indenter meets therefore less resistance in this case. The force acting on the indenter is thus reduced to a lower value and the indenter penetrates the rock to a great depth within a short time. The continued motion of the indenter will then repeat the above-explained process.

In any case the indenter will penetrate into the rock with increasing load and the cracks will remain in the rock. Indentation depth in the context of this report is defined as the permanent displacement of the indenter on the force-penetration curve after unloading, which is shown in Figure 8-1 as OP on the abscissa and represented by z in the present context. The length of the radial/median cracks is defined as the distance from the indentation center on the original rock surface to the furthest position of the cracking within

the rock specimen. Similarity analysis will be used in this chapter. Two indentation events are considered to be similar if corresponding characteristic physical quantities, such as stress, strain, etc., lie at corresponding spatial locations. This statement implies that the corresponding states of the fractures lie at corresponding locations in the rock specimen, and, therefore, corresponding (dimensionless) indentation depths and the lengths of radial/median cracks should be the same for similar indentations.

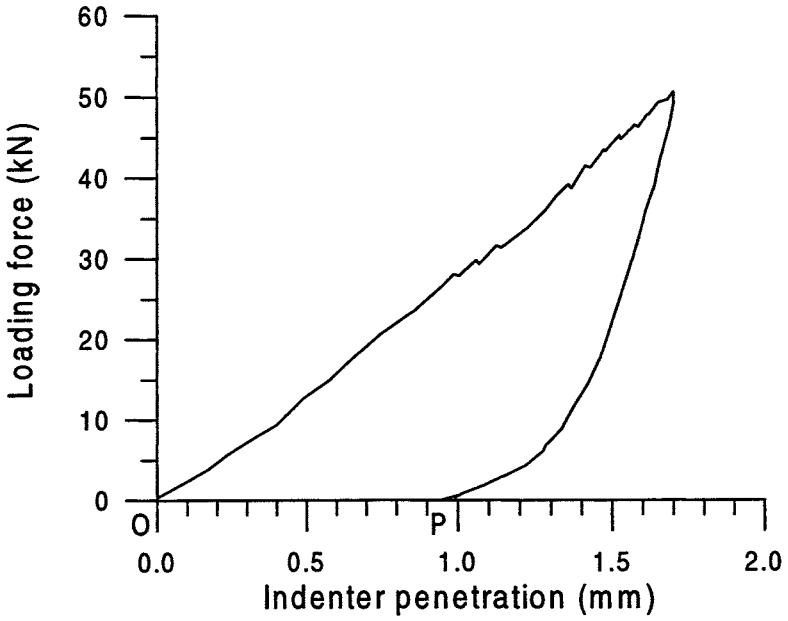

Figure 8-1 *Typical force-penetration curve recorded when an indenter penetrates rock. In the figure, OP on the abscissa is defined as indentation depth.*

8.1 ASSUMPTIONS

In many practical cases in engineering geology our knowledge is still limited when describing the behaviour of the objects to be examined. To achieve effective analyses, the problem must be simplified, even if the most sophisticated computational methods are used. Rock indentation is actually the interaction between the rock and the indenter. In general, this is a very complex problem. In order to simplify the analysis certain assumptions must be applied based on our understanding of the indentation mechanisms. They are concerning the geometry of the specimen, the properties of the rock and the indenter, and indentation process. These assumptions are as follows.

Semi-infinite rock. This is granted by the careful design of our specimens as described in chapter 3. Under this assumption the geometrical similarity between rock samples is satisfied automatically. It is, therefore, possible to

characterise the rock only by its material properties without the necessity of taking its geometry into consideration.

Homogeneous and isotropic rock material. Due to this assumption no inhomogeneous material scale needs to be considered in the analysis, and the mechanical properties of rock material are not a function of the coordinates.

Constitutive similarity for different rocks. By constitutive similarity, we mean that the various rocks may have different mechanical properties, but they have identical scaled strength and stiffness properties, so that stress normalised by the corresponding Young's modulus is identical for all strains for these rocks, i.e. similarity exists in the stress-strain curves or constitutive properties. In other words, the stress-strain curves for different rocks are identical when the stress in Figure 5-1 is normalised by the uniaxial compressive strength or Young's modulus of the individual rock.

Rigid indenter. This assumption is reasonable since in indentation tests the Young's modulus of the indenter material is normally three to five times higher than that of the rock. According to this assumption the indenter can be characterised only by its geometrical shape, without taking its material properties into consideration. A hemispherical indenter can therefore be characterised by the diameter of the cylinder part, d, and the diameter d' of the hemispherical surface with its centre on the central axis of the cylinder. Diameter d' can be represented by a nondimensional quantity $\bar{d}$ defined by $\bar{d} = d'/d$. The other indenters can be treated in a similar way. Obviously, the tool slenderness (height/diameter) has no influence on rock fracture in normal indentation events close to actual practical use.

Concerning the indentation process there are three assumptions:

Static load. The word "static" or "quasi-static" implies that the time of response of rock indentation is not important. In this case the strain rate effects of the strength and the density of the rock, ρ, namely the inertia, have no influence on the results. In TBM boring, percussive drilling and excavations using other indenter types, the typical maximum speed in practice is 8 to 10 m/s. This speed is 3 to 4 orders lower than the stress wave velocity in the rock. We simply, therefore, assume that the static results can be a good approximation to the practical cases. This argument can be confirmed by the experiment carried out by Evans & Wilshaw (1977). According to their results a quasi-static approach provides a reasonable damage prediction for ceramics at velocities $\leq$ 160 m/s; while a dynamic approach appears to be tenable at high velocities $\geq$ 400 m/s.

Isothermal. Temperature effects will be neglected in this case. This is possible since the elevation of the temperature in the rock is rather low and exerts no significant influence on the mechanical properties of either the rock or the indenter.

Neglect of friction between the indenter and the rock.

8.2 SIMILARITY ANALYSIS OF INDENTATION DEPTH AND CRACK LENGTH

Indentation depth will be discussed first. It is clear from the above assumptions that the problem is axisymmetric and the governing parameters that control the indentation depth can be formulated in Table 8-1 based on the above discussions. The first parameter is the indentation load magnitude. The next two parameters are related to the indenter geometry, which affects the load distribution. The next four characterise the rock material, and the last one is the response parameter. The geometry of the rock sample is not necessarily considered due to the assumption of a semi-infinite rock mass. The simplification has helped us to identify the eight most important governing parameters or factors that reflect the essence of the indentation events. The maximum force F and the characteristic size of the indenter d are chosen as fundamental dimensions for the indentation process.

Table 8-1 Physical parameters governing indentation depth

No	Parameter	Dimensions	Description
1	F	F	Maximum indentation force
2	d	L	Characteristic size of the indenter
3	d_i	1	Other nondimensional geometrical parameters of the indenter normalized by d
4	d_g	L	Grain size
5	σ_0	FL^{-2}	Uniaxial compressive strength of the rock
6	σ_i	1	Stresses normalized by the uniaxial compressive strength
7	E	FL^{-2}	Young's modulus
8	G_{IC}	FL^{-1}	Critical energy release rate with crack of mode I
9	z	L	Indentation depth

We assume there is a physical law of the form

$$f(F,d,d_i,d_g,\sigma_0,\sigma_i,E,G_{IC},z)=0, \qquad 8\text{-}1$$

which provides a relationship between these quantities. Only seven independent dimensionless products can be formed from the nine quantities. There is an equivalent physical law between the independent dimensionless quantities according to the well-known π theorem in similarity analysis (Baker et al., 1978). The relation between the seven π terms can be written as follows:

$$\frac{z}{d}=f(d_i,\frac{d_g}{d},\sigma_i,\frac{E}{\sigma_0},\frac{F}{\sigma_0 d^2},\frac{G_{IC}}{\sigma_0 d}). \qquad 8\text{-}2$$

The dimensionless quantity, $\frac{d_g}{d}$, should not be included for homogeneous and isotropic material since $\frac{d_g}{d}$ approaches zero, and σ_i and $\frac{E}{\sigma_0}$ will disappear for the rock materials with a constitutive similarity between them. Eq. (8-2), therefore, becomes

$$\frac{z}{d}=f(d_i,\frac{F}{\sigma_0 d^2},\frac{G_{IC}}{\sigma_0 d}). \qquad 8\text{-}3$$

Eq. (8-3) is a functional relationship which characterizes the indentation depth. The term d_i requires geometrical similarity between different indenters. The so-called corresponding force is denoted by $\frac{F}{\sigma_0 d^2}$. The characteristic material property is specified by $\frac{G_{IC}}{\sigma_0 d}$. The term $\frac{z}{d}$ is used to explain the corresponding indentation depth.

Compared with the physical process involved in the indentation depth, the extension of radial and median cracks may be classified as a "far-field" event. Some of the pertinent physical parameters which control the "far-field" phenomenon of rock indentation are different from those in Table 8-1. The importance of the same physical parameters can also be different in the two cases. The characteristic size of the indenter is more important in determining the "near-field" phenomenon. However, the effect of the indenter "sharpness" cannot be neglected according to the experiment (Lawn et al, 1976) and this is expressed by the nondimensional geometrical parameters of the indenter normalized by its characteristic size, namely d_i. The parameters related to the yield of material are not so important as the previous case, but the elastic constants of the rock, i.e. Young's modulus E and Poisson's ratio ν, should be taken into account. The response parameter in this case is the crack length c.

An approach similar to that adopted in the discussion about the indentation depth leads to the following functional relationship between π terms:

$$c^{3/2}(\frac{EG_{IC}}{1-\nu^2})^{1/2} / F = f(d_i, \frac{E}{\sigma_0}, \frac{F}{\sigma_0 d^2}) \qquad 8\text{-}4$$

The assumption of constitutive similarity between the four kinds of rock is still imposed as we did previously when discussing the indentation depth. We may then have a relationship of crack length for an indenter specified by d_i as follows:

$$c^{3/2}(\frac{EG_{IC}}{1-\nu^2})^{1/2} / F = f(d_i, \frac{F}{\sigma_0 d^2}) \qquad 8\text{-}5$$

The functional relationships Eqs. (8-3) and (8-5) will be examined and calibrated by experiment.

8.3 FORMULATION OF A MODEL FOR INDENTATION DEPTH

It was found from the experimental data that the dimensionless quantities $\frac{z}{d}$ and $\frac{G_{IC}}{\sigma_0 d}$ in Eq. (8-3) can be combined to form one quantity, and the dimensionless physical law can, therefore, be further simplified as

$$\frac{zG_{IC}}{d^2\sigma_0} = f(d_i, \frac{F}{\sigma_0 d^2}), \qquad 8\text{-}6$$

where the rock's response to indentation is $\frac{zG_{IC}}{d^2\sigma_0}$, the external force is $\frac{F}{\sigma_0 d^2}$ and the parameter d_i expresses the requirement of geometrical similarity between different indenters. If we restrict the discussion to any one of the applied indenters in the previously described experiment in Chapter 3, the requirement of geometrical similarity between the indenters is satisfied automatically. Eq. (8-6) can then be formally expanded in a Taylor series in a power of $\frac{F}{\sigma_0 d^2}$ as

$$\frac{z}{d}(\frac{G_{IC}}{\sigma_0 d}) = c_0 + c_1(\frac{F}{\sigma_0 d^2}) + c_2(\frac{F}{\sigma_0 d^2})^2 + \ldots \qquad 8\text{-}7$$

In Eq. 8-7, the coefficients c_1, c_2, c_3,... depend on the indenter shape. As we mentioned previously, a hemispherical indenter can be characterized by the diameter of the cylinder, d, and the diameter d' of the hemispherical head

surface; a truncated indenter can be characterized by d, d', and d'', where d is the diameter of the cylinder, and d' and d'' characterise the diameter of the truncated hemispherical surface and the ending circular plane, respectively; and in the case of a cylindrical indenter the only characteristic parameter is its diameter. Therefore, c_i can be expressed as a function of d_i in the form

$$c_i = c_i(\frac{d'}{d}, \frac{d''}{d}).$$

In practice $\frac{d'}{d}$ is greater than 1, and $\frac{d''}{d}$ is between 1 and zero. While $\frac{d''}{d}$ approaches zero, c_i are the values for a hemispherical indenter; while $\frac{d''}{d}$ approaches 1, c_i are for a cylindrical indenter. A detailed search for the complete expression of the functions $c_i(\frac{d'}{d}, \frac{d''}{d})$ by using mechanics and mathematical tools is beyond the scope of the present report, and an empirical solution will be resorted to instead. The experimental results can then be arranged in terms of the nondimensional parameters as shown in Figs. (8-1) to (8-3) for hemispherical, truncated, and cylindrical indenters, respectively.

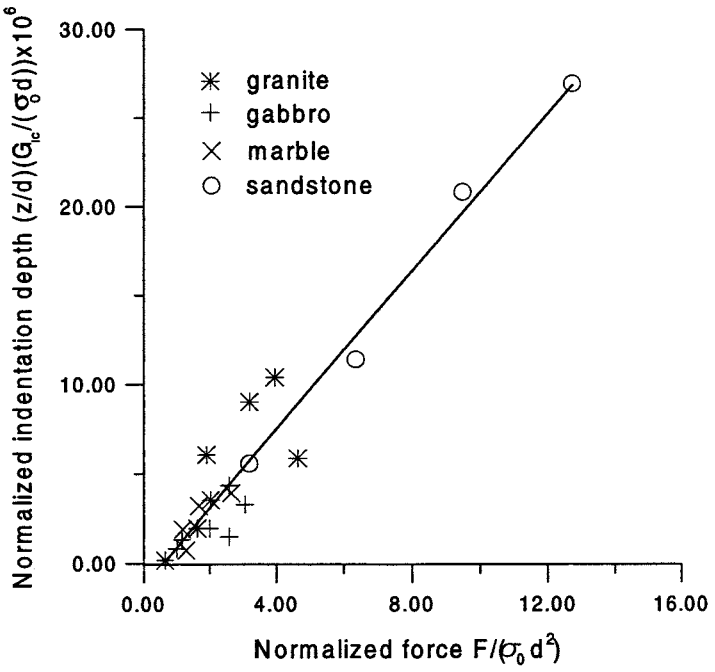

Figure 8-1 *Indentation depth vs. indentation force in nondimensional form for the hemispherical indenter.*

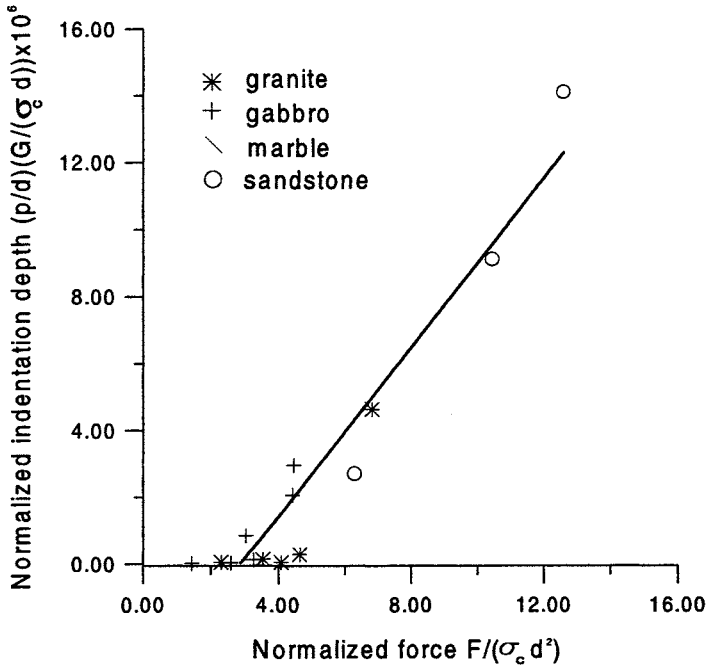

Figure 8-2 *Indentation depth vs. indentation force in nondimensional form for the truncated indenter.*

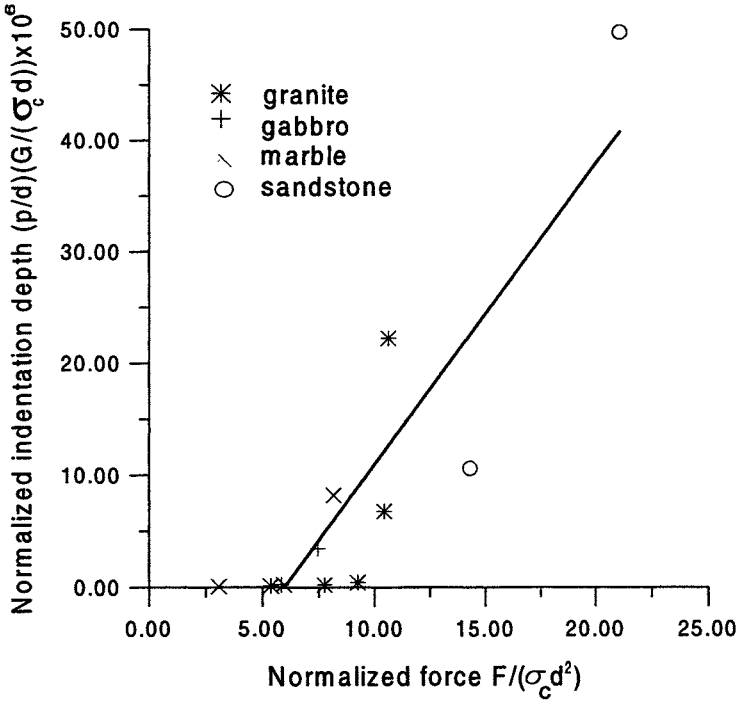

Figure 8-3 *Indentation depth vs. indentation force in nondimensional form for the cylindrical indenter.*

From these figures it is clear that the first two terms on the right side of Eq. (8-7) are sufficient to describe the experimentally obtained relationships. When the variables are in SI units, i.e. the force is in the unit of N, the stress

is in Pa, the energy release rate is in J/m^2 and the length in m, it is better to rewrite Eq. (8-7) as follows:

$$\frac{z}{d}(\frac{G_{IC}}{\sigma_0 d})*10^6 = c_0 + c_1(\frac{F}{\sigma_0 d^2}) \qquad 8\text{-}8$$

A comparison of the dimensionless data with the functional relationship Eq. (8-8) gives three pairs of c_i for describing the indentation depth induced by different indenters. From the data obtained by using the hemispherical indenter, we obtain

$$c_0 = -1.27, \quad c_1 = 2.24, \quad \text{with } r = 0.97, N = 20. \qquad 8\text{-}9$$

where, $\frac{d'}{d}$=1.1 and $\frac{d''}{d}$=0; from the data obtained by using the truncated indenter, we have

$$c_0 = -3.63, \quad c_1 = 1.26, \quad \text{with } r = 0.96, N = 15, \qquad 8\text{-}10$$

where $\frac{d'}{d}$=1.1 and $\frac{d''}{d}$=0.67; and from the experimental results by using the cylindrical indenter

$$c_0 = -16.0, \quad c_1 = 2.69, \quad \text{with } r = 0.88, N = 12, \qquad 8\text{-}11$$

where $\frac{d''}{d}$=1. For the cylindrical indenter d' has no definition theoretically but however, d' has always a certain value practically, which means that a clean cylindrical indenter seldom exists in field.

These formulas are valid when the force F is so large that the right sides of the formulas are not negative, which means that the indentation depth z must be equal to or greater than zero. In the above expressions, r is the correlation coefficient and N the number of data samples.

Different shapes of indenter will cause different load distributions along the contact surface between the indenter and rock. This will affect the indentation depth, especially since indentation depth is a near-indenter-field phenomenon. This statement is expressed by the four equations, i.e. Eqs. (8-8) to (8-11), for the three different types of indenter. Two points should be emphasized: firstly, once $\frac{d'}{d}$ is fixed, the values of $\frac{d''}{d}$, which vary from 0 to 1, will determine the values of c_i, and the so-called truncated indenter will, therefore, give various values of c_i depending on the specific value of $\frac{d''}{d}$ with the hemispherical and the cylindrical cases as its

limitation; secondly, once $\frac{d''}{d}$ is fixed, for example in the case of a hemispherical indenter, the values of $\frac{d'}{d}$ will also affect the values of c_i, and therefore, the obtained specific values of c_i above can only be applied to the cases where the indenters are geometrically similar to those used in our experiment. However, it is worth noticing that both the intercepts c_0 and the coefficients c_1 in Eq. (8-8) are independent of the rock types and the size of the indenter diameter. In principle the semi-empirical and semi-theoretical formulas, Eqs. (8-8) to (8-11), are valid for a rather large category of rock similar to those used in the experiment with various diameters of the above-stated indenter and various magnitudes of indentation force. Therefore, these formulas can have wide applications.

The predicted indentation depths in the four types of rock when a hemispherical indenter has been used with various magnitudes of load are shown in Figure 8-4. The intercepts on the ordinate show the threshold of the force required to start penetration for different types of rocks. They are 4.5 kN for Lemunda sandstone, 12.4 kN for Bohus granite, 13.1 kN for Ekeberg marble, and 22.7 kN for Kallax gabbro with an indenter diameter of 12 mm. However, the order can be changed at a high load level. For example, at a load of 300 kN, the indentation depths for these four kinds of rock are in the order of marble, gabbro, granite, and sandstone, from the largest to the smallest. Therefore, the load level control is important both in machine design and in practical operation if one wishes to obtain a maximum indentation depth in each percussion or rotation round.

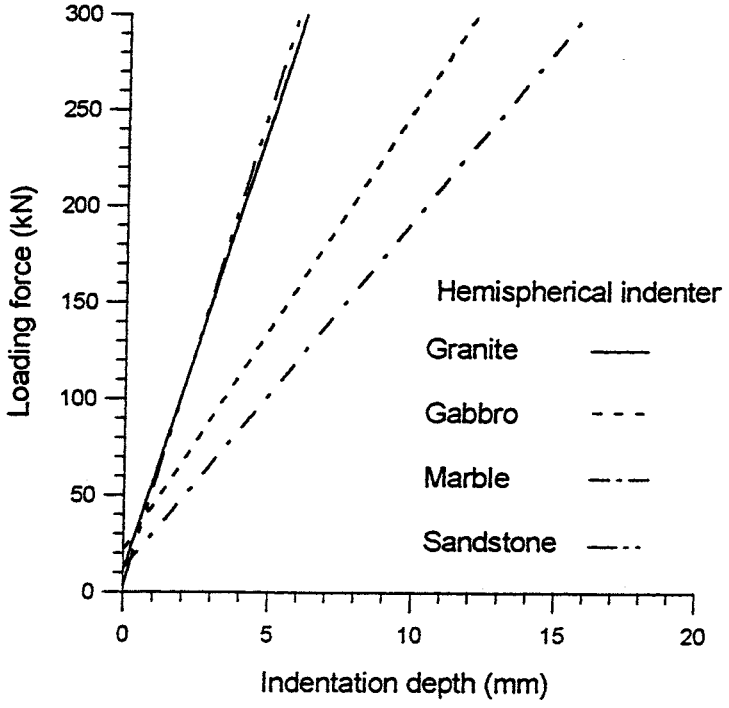

Figure 8-4 *Relationship between indentation depth and loading force for different rocks when a hemispherical indenter has been used. The curves are the prediction by Eqs. (8-8) and (8-9).*

From Eqs. (8-8) to (8-11), we may also have relationships between indentation depth and loading force for a particular rock with different indenter types. For example, the loads required to start penetrating the granite rock are 12.4, 63.3, and 130.7 kN for hemispherical, truncated, and cylindrical indenters, respectively, with an indenter diameter of 12 mm. In Bohus granite, a hemispherical indenter produces the largest indentation depth among the three indenters with the same magnitude of indentation force all the way up to 300 kN, which stresses the importance of sharpening blunt indenters.

8.4 FORMULATION OF A MODEL FOR THE LENGTH OF RADIAL AND MEDIAN CRACKS

The right side of Eq. (8-5) can be expanded in a Taylor series in powers of $\frac{F}{\sigma_0 d^2}$. The experimental results can then be arranged in terms of the nondimensional parameters as shown in Figure 8-5 for the hemispherical indenter.

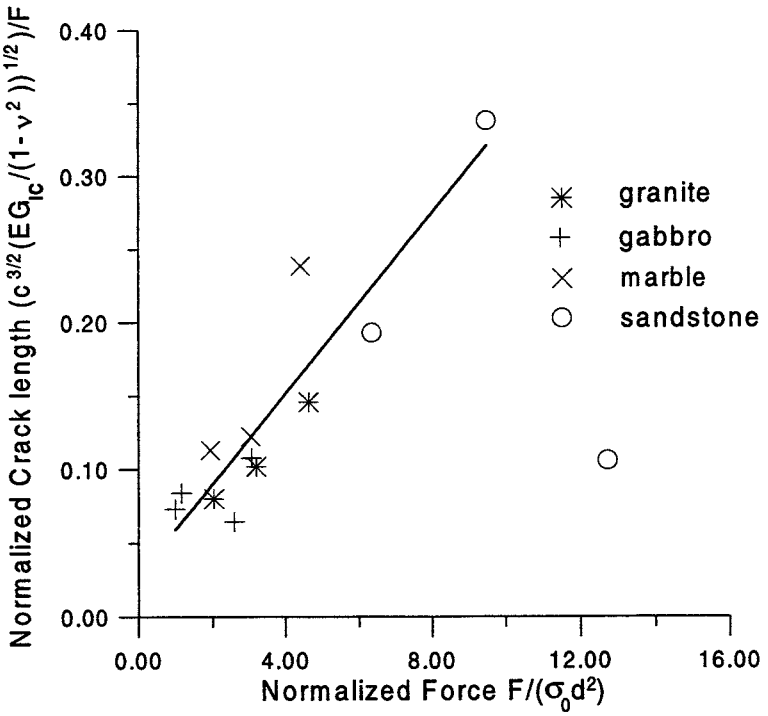

Figure 8-5. *Radial/median crack length vs. indentation force in nondimensional form for the hemispherical indenter.*

From this figure one can see that the first two terms of the Taylor series are sufficient to describe the relation between the nondimensional length of radial/median cracks and the indentation force. Similar situations have been obtained for the truncated and the cylindrical indenters. In this way, Eq. (8-5) will be rewritten as

$$c^{3/2}(\frac{EG}{1-\nu^2})^{1/2} / F = a_0 + a_1(\frac{F}{\sigma_0 d^2}). \qquad 8\text{-}12$$

The coefficients a_0 and a_1 in Eq. (8-12) vary with the indenter type and can be expressed formally as

$$a_i = a_i(\frac{d'}{d}, \frac{d''}{d}). \qquad 8\text{-}13$$

where $i = 0$ and 1. These coefficients can be specified by comparison with the experimental results for each individual indenter type, and this gives the following three equivalent equations:

for the hemispherical indenter,

$$a_0(1.1,0) = 0.0280, \quad a_1(1.1,0) = 0.0309, \quad N = 12, \quad r = 0.84, \qquad 8\text{-}14$$

for the truncated indenter,

$$a_0(1.1,.67) = -0.0581, \quad a_1(1.1,.67) = 0.0400, \quad N = 5, \quad r = 0.43, \qquad 8\text{-}15$$

and for the cylindrical indenter,

$$a_0 = -0.0163, \quad a_1 = 0.0116, \quad N = 7, \quad r = 0.71. \qquad 8\text{-}16$$

The variables are in SI units. In addition, all of these formulas in this chapter are valid when the force F is so large that the right sides of the formulas are not negative, which means that c must be equal to or greater than zero. The radial/median crack lengths predicted by using Eqs. (8-12) and (8-14) for the four types of rock when using a hemispherical indenter with various magnitudes of load are shown in Figure 8-6, together with the test results. The crack lengths in sandstone are the longest among the four rocks, followed by marble, granite, and gabbro for the same magnitude of load. Among the three types of indenter with the same magnitude of load, the hemispherical one produces the longest lengths of radial/median cracks, followed by the truncated and the cylindrical indenters.

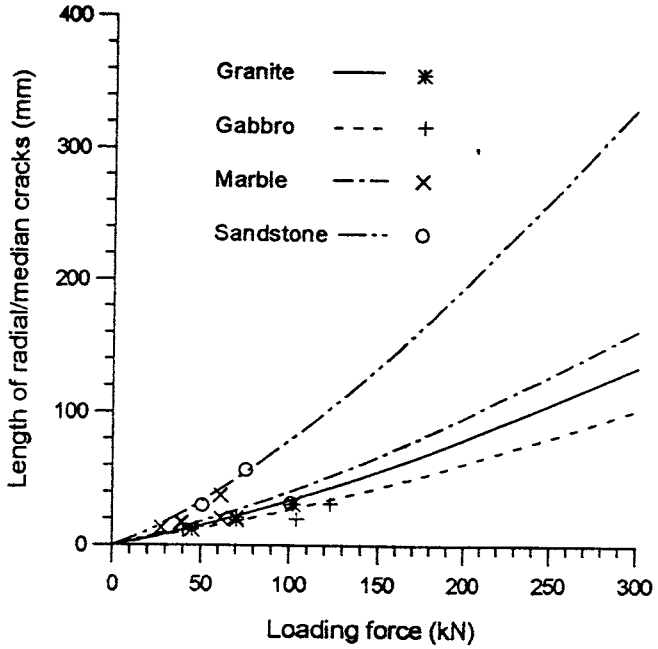

Figure 8-6. *Relationship between radial/median crack length and loading force for different rocks when a hemispherical indenter has been used. The curves are the prediction by Eqs. (8-12) and (8-14), and the symbolized points represent the results from the experiments.*

8.5 DISCUSSION ON THE SELECTION OF MECHANICAL PARAMETERS OF ROCK IN THE MODELS

Rock behaviour under the action of mechanical tool indentation is described in the present report by only three parameters in the near-field, namely compressive strength, Young's modulus, and energy release rate (or equally fracture toughness). In the far-field, Poisson's ratio is added for prediction of the long cracks induced by indentation. This treatment is based on two considerations: a) these parameters are basic for describing the characteristics of most rocks under the action of compressive load; b) the parameters employed in the formulas are readily obtainable from simple tests in an ordinary rock mechanics laboratory. This also makes it possible to simplify the problem to a great extent, so that simple and meaningful results can be obtained without sacrificing accuracy and rigour too much. However, discontinuities and material anisotropy can have major effects on excavation depth and the length of remaining cracks in the rock caused by mechanical tools in some special cases, but this is not taken into consideration in the present report.

9 DISCUSSIONS

9.1 LENGTH OF RADIAL/MEDIAN CRACKS RELATED TO INDENTATION DEPTH

When Eqs. (8-8) and (8-12) are treated as simultaneous equations, we may obtain the relationships between the crack length and indentation depth for the three typical indenters. Figure 9-1 shows the relationship between the length of the radial/median cracks and the indentation depth induced by a hemispherical indenter in the four different rocks, where the ending point of each curve corresponds to 300 kN.

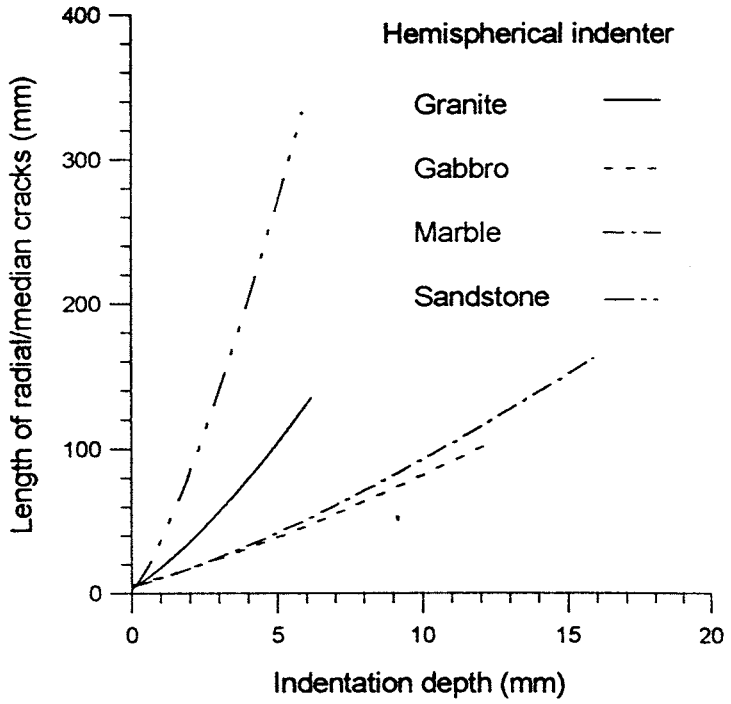

Figure 9-1. *Relationship between radial/median crack length and indentation depth for different rocks when a hemispherical indenter has been used.*

From this figure, one may notice that:

- cutting gabbro with a hemispherical indenter produces the shortest crack length among the four rock types with the same indentation depth, followed by marble, granite, and sandstone.
- the increasing rates of the crack lengths with increasing indentation depth are different for different rocks. The Lemunda sandstone has the highest increasing rate, followed by Bohus granite, Ekeberg marble, and Kallax

gabbro. This is determined by the combination of the mechanical properties of the rock in question.

Based on the above observation it is easy to understand that one could possibly produce a shorter crack length by having a short indentation depth for each cut. This explains why the worker has a certain possibility of controlling crack lengths with careful operation of the machine. The "careful operation" here means that each rotation round has a smaller advance with smaller thrust. This should be considered in practical operations in both percussive drilling and full face boring.

Figure 9-2 shows the relationship between the length of the radial/median cracks and the indentation depth induced by the three different indenters in granite, where the ending point of each curve also corresponds to 300 kN.

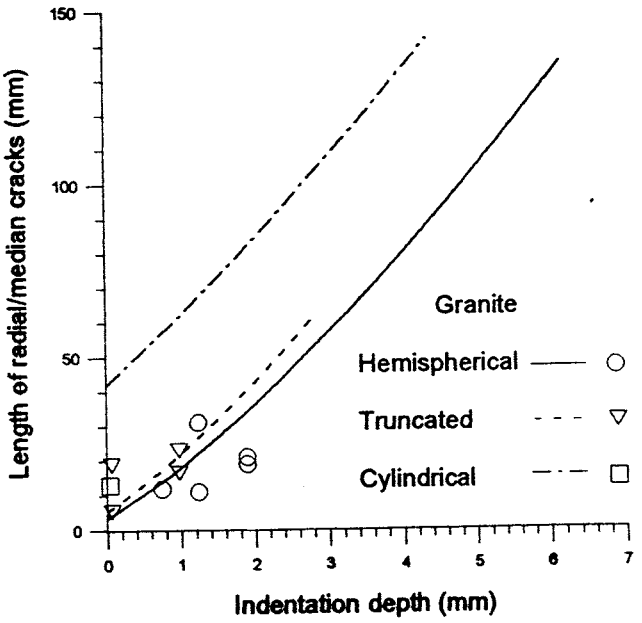

Figure 9-2. *Relationship between radial/median crack length and indentation depth in granite when a hemispherical indenter, a truncated indenter, or a cylindrical indenter has been used.*

From this figure one can notice that:

- To cut rock with a hemispherical indenter always produces the shortest crack length among the three indenter types with the same indentation depth, followed by the truncated and the cylindrical indenter. This indicates the importance of resharpening the buttons in order to obtain fewer remaining cracks in the rock wall.
- There is a considerable difference in the crack lengths induced by the three different indenters when the indentation depths approach zero. This difference is caused by the indenter shapes. The hemispherical and the cylindrical indenters belong individually to extreme cases, with the truncated one in between with a variation depending on its shape, i.e. the

value of $\frac{d''}{d}$. However, the increasing rates of the crack length with increasing indentation depth are almost the same for the different indenters. This indicates the strong dependence of these relationships, which relate the crack length to the indentation depth, on the mechanical properties of the rock.

9.2 MECHANISMS OF INDENTATION-INDUCED SIDE CRACK AND CHIPPING

As pointed out in our conceptual model (Kou, et al 1994), the chipping corresponding to the sawtooth-like shape in the figures for indentation depth vis. indentation force (see Figure 3-6, for example) occurs during loading rather than unloading. The unloadings in the figure were caused by the rapid increase of penetration due to chipping. This kind of chipping is caused by a fast lateral expansion of the rock compressed in all three directions underneath the indenter. This part of the rock, which is in the state of post-failure, constitutes a local soft region and flows easier. The flow along the circumferential direction under the indentation action pushes the rock shell with the pressure q and separates it from the rock body. The dilatation of the rock underneath the indenter can also play a similar role as the local soft region. These mechanisms were equivalently recognised by our numerical analysis. The numerical analyses have shown that side cracks can be initiated from the side of the crushed zone and grow to the surface during loading, which is in agreement with the experiment. Actually, in rock indentation tests, side cracking or chipping is often observed during loading. Side cracks have been observed to be initiated not exactly at the bottom, but by the side of the crushed zone (Lindqvist et al., 1994).

However, there might be other kinds of chips induced by residual stress and formed at unloading. Indentation tests on glass and some other crystal materials using sharp indenters have shown that side cracks are formed during unloading (Lawn and Wilshaw, 1975). It has also been observed that in rock indentation tests with a cone shaped head, a complete chip was formed when the load was quickly withdrawn (Li and Gao, 1986). This was, however, not reported as being a typical event in indentation experiments using blunt indenters (Lawn and Wilshaw, 1975; Lindqvist et al., 1994). Some theories have been formulated to describe the formation of side cracks during unloading (Chiang, et al. 1982 and Yoffe, 1982). The driving force is ascribed to the inconsistency of recovery between the crushed or damaged (yielded) material beneath the indenter and the elastically deformed material surrounding it. Residual stresses caused by the expansion of a yielded zone can be solved using the elasto/plasticity theory (Hill, 1951) and modified to fit the semi-infinite plane situation (Chiang, et al. 1982). Tensile stresses are generated below the surface near the damaged zone, which explains, in principle, the initiation of lateral cracks. In this study, however, a simplification has been made to consider only cracks caused by loading.

9.3 EFFECT OF CONFINEMENT ON INDENTATION DEPTH AND CRACK LENGTH

Confinement is an important factor affecting rock fracture under indentation. We may simply modify Eq. 8-8 or Eq. 8-12 to include its influence on the indentation depth or on the length of radial/median crack. If the confining stress is not too high, the failure criterion in triaxial compression can be given quite accurately by:

$$\sigma_c = \sigma_0 + q\sigma_p, \qquad 9\text{-}1$$

where σ_c, σ_0 and σ_p are triaxial compressive strength, uniaxial compressive strength, and confining stress, respectively. This linear relationship has been verified by experiments (for example Kou et al., 1990, Bieniawski, 1968). According to the experimental results, the coefficient q for structured coal (Kou et al., 1990; Kou et al., 1993) can vary between 1.3 and 3.9, and it was set to 5 for Sierra granite by Cook et al. (1984). A general conclusion from the research on the influence of confining stress on the energy release rate of various types of rocks using various testing methods is that an increasing confining stress definitely results in an increase in the measured energy release rate (Whittaker et al., 1992). Unfortunately we have not had any accurate relationship on the variation of energy release rate with confinement until now and have simply set it as invariant. In this way Eqs. (8-8) to (8-11) can be rewritten as follows:

for the hemispherical indenter

$$\frac{z}{d}\left[\frac{G}{(\sigma_0 + q\sigma_p)d}\right] * 10^6 = -1.27 + 2.24\left[\frac{F}{(\sigma_0 + q\sigma_p)d^2}\right], \qquad 9\text{-}2$$

for the truncated indenter

$$\frac{z}{d}\left[\frac{G}{(\sigma_0 + q\sigma_p)d}\right] * 10^6 = -3.63 + 1.26\left[\frac{F}{(\sigma_0 + q\sigma_p)d^2}\right], \qquad 9\text{-}3$$

and for the cylindrical indenter

$$\frac{z}{d}\left[\frac{G}{(\sigma_0 + q\sigma_p)d}\right] * 10^6 = -16.0 + 2.69\left[\frac{F}{(\sigma_0 + q\sigma_p)d^2}\right]. \qquad 9\text{-}4$$

According to these equations, the bearing capacity of rocks will increase depending on the depth from the earth's surface. For example, the critical bearing capacity of Bohus granite is about 1155 MPa on the earth's surface. Underground at a depth of 300 m from the surface, where 20 to 25 MPa of extra confining stress could be achieved due to tectonic pressure according to the test at Äspö Laboratory (SKB, 1994), the critical bearing capacity of

the same rock can reach 1.65 to 1.82 times that, i.e. 1911 to 2100 MPa. In the above deduction, q was set to 5 and $\sigma_0 = 152.8$ MPa. While taking into account the increase in energy release rate with increasing confining stress, the increase in critical bearing capacity can be even higher. The critical bearing capacity was obtained when the indentation depth z approached zero in Eq. (9-4). From this argument we may deduce that: firstly, the indentation depths predicted by Eqs. (8-8) to (8-11) are overestimated if the indentation is carried out underground; secondly, there is a possibility of increasing the penetration depth by reducing the confining stress, for example when the indenter works in the neighbourhood of a free surface or of any other weak plane. This also leads to the well-known hole deviation especially in percussive drilling. It also means that a much more effective breakage can be achieved in rock cutting if multi-free surfaces around the cutter can be created so that less confinement is realised.

In a way similar to that treated in the discussion about the indentation depth, the relationship between the crack length and indentation force, Eqs.(8-12) to (8-15), can be modified to include the influence of confining pressure as follows:

for the hemispherical indenter with $\frac{d'}{d}$=1.1,

$$c^{3/2}\left(\frac{EG}{1-\nu^2}\right)^{1/2} / F = 0.0280 + 0.0309\left[\frac{F}{(\sigma_0 + q\sigma_p)d^2}\right], \qquad 9\text{-}5$$

for the truncated indenter $\frac{d'}{d}$=1.1 and $\frac{d''}{d}$=0.67,

$$c^{3/2}\left(\frac{EG}{1-\nu^2}\right)^{1/2} / F = -0.0163 + 0.0116\left[\frac{F}{(\sigma_0 + q\sigma_p)d^2}\right], \qquad 9\text{-}6$$

and for the cylindrical indenter,

$$c^{3/2}\left(\frac{EG}{1-\nu^2}\right)^{1/2} / F = -0.0581 + 0.0400\left[\frac{F}{(\sigma_0 + q\sigma_p)d^2}\right]. \qquad 9\text{-}7$$

According to these equations, the length of a crack in a rock produced by a certain load will decrease depending on the depth from the earth's surface. Using a similar argument to that for the indentation depth, we may also deduce that: firstly, the crack lengths predicted by Eqs. (8-12) to (8-15) are overestimated if the indentation is carried out underground; secondly, there is a possibility of reducing the crack length by increasing the confining stress, for example when the indenter works in the neighbourhood of a rock mass with extra confining stress. The extra confining stress can be offered not only by tectonic pressure but also by the neighbouring tools. Figure 9-3

shows a cross-section of a crack pattern in Öjeby granite caused by a triple tungsten carbide kerf cutter. The tungsten carbide cutter was filled with hemispherical carbide inserts with a tip radius of 16 mm. The spacing between two cutters is 40 mm. The total load was 250-300 kN. In the figure, side cracks coalesce with each other. The median crack under the intermediate cutter was depressed. The coalescence of side cracks is due to the combined action of multi-indenters. The suppression of the long crack (radial/median crack) under the intermediate cutter can now be explained by taking the confinement into account. If there were two cutters in action simultaneously, the length of the crack could be estimated by Eq. (9-5). The confining stress could be added by taking the action of the other cutter into account. The confining stress for the formation of the crater induced by the other cutter is not significant. However, this confining stress increases with depth and then decreases again after a certain depth. Therefore, it will suppress the crack length according to Eq. (9-5). In the case shown in Figure 9-3, there are three cutters in action simultaneously. The rock under the intermediate cutter sustains a higher confinement than that under the edge cutters due to the superposition of the extra confining stresses induced by both edge cutters. The confinement in this case is introduced by the operation. Therefore, we call it operation-induced-confinement. From this argument, we may deduce that the cracks remaining in the rock wall can be reduced by the combined action of multiple cutters working simultaneously, that longer cracks will be produced under the edge cutters, and that the lengths of the cracks vary since the simultaneous action of multiple cutters seldom occurs in reality.

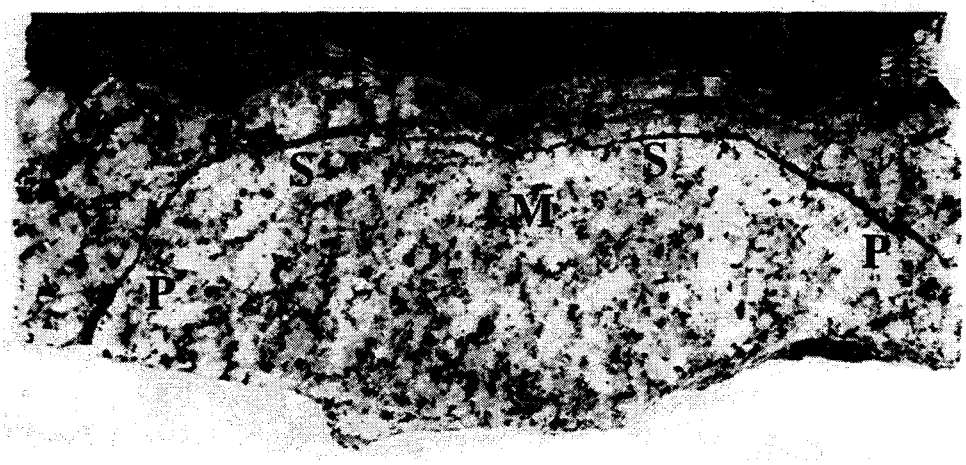

Figure 9-3 *Cross-section of crack pattern caused by a triple tungsten carbide kerf cutter (Lindqvist and Rånman, 1980). S denotes side cracks, M median crack and P was named as prism crack, according to Lindqvist and Rånman.*

There are more examples to show the effect of the confining stress:

- the crack is inflected towards the rock surface due to less confinement from the upper side of the crack;
- a quasi-static indentation process can be transformed to a dynamic process by a very quick release of the confinement, and this is also the reason for the transformation of the indentation mode from stability to instability;
- the radial/median cracks can split the specimen into pieces before the formation of rock chips at the surface due to low confinement;
- the lengths of the cracks in a given rock induced by a given load may vary to quite a large extent due to the variation of confining stresses;
- the lengths of cracks might be greatly suppressed when the tools work deep underground;
- the lengths of cracks might be very long when the cutters or button bits work in the area close to joints, free surfaces, or other weaknesses, etc.

Equation (9-1) provides a means of modifying the formulas to calculate the indentation depth and crack length due to the influence of axial symmetric confining pressure. In the case of arbitrary three-dimensional stresses a Mohr-Coulomb criterion can be invoked but this will, however, not be discussed in the present report.

9.4 SHAPE OF INDENTER RELATED TO PENETRATING EFFICIENCY AND CRACK LENGTHS

One can see from Eqs. (8-8) to (8-11) that a sharper indenter needs a smaller threshold force in the same rock. In general, a spherical indenter is therefore more effective in penetrating rock than a cylindrical one. As an example, an indentation test in Bohus granite to a maximum force of 200 kN will produce different indentation depths for different indenters with a diameter of 15 mm. The calculated depths are 3.85 mm, 1.22 mm, and 0 mm for hemispherical, truncated, and cylindrical indenters, respectively, according to Eqs. (8-8) to (8-11). However, in most cases the assignment of a simple index of sharpness will not be so straightforward. A hemispherical indenter is more efficient at low loads compared with the other two, but the situation might be changed at high loads. According to these deduced formulas, an originally sharp indenter with a worn tip penetrating into rock may act much like a blunt indenter, and the threshold force required to penetrate the rock will, therefore, be increased. Conversely, an originally cylindrical indenter can wear to a shape much like a truncated or even a hemispherical one, and its threshold force in penetrating rock can, therefore, be decreased. This should be considered by designers of drill bits and TBM cutters.

9.5 INFLUENCE OF LOADING RATE ON INDENTATION RESULTS

The loading rate might influence the results of indentation due to the effects of the stress wave in the rock produced by the impact of the TBM disc cutter. Literature reviews on the difference between dynamic and static indentation were conducted first by Kou et al. (1989) and then by Zhang &

Kou (1990). Dynamic indentation tests for ceramic material with indenter speeds of approximately 20 to several hundred metres per second show that dynamic and static indentation have basically the same crack pattern and the same fracture sequence (Chaudhri & Kurkjian, 1986, Chaudhri & Walley, 1978, Frank & Lawn, 1967, Evans et al., 1978); but in dynamic indentation several layers of side cracks and a deeper crushed zone with a depth-width ratio of 0.8 (in static cases this ratio is normally 0.5) have been observed; dynamic indentation has a smaller plastic zone but a larger fracture area compared with the static indentation for the equivalent impression radius. Some authors (Frank & Lawn, 1967) observed that the radial cracks and the side cracks can be generated without any plastic deformation, and that the cross-angle of Hertzian cracks is significantly smaller than that generated in static indentation. However, according to Evans & Wilshaw (1977) a quasi-static approach provides a reasonable damage prediction at velocities less than 160 m/s; while a dynamic approach appears to be tenable at high velocities larger than 400 m/s. In the present discussions on rock breakage by indentation the maximum speed is 8 to 10 m/s. We, therefore, simply assume that the static results can be a good approximation of the cases in TBM boring, since the speed is 3 to 4 orders lower than the stress wave velocity in the rock.

We believe that the quasi-static approach can capture the essential information, and the above discussions explain why we treat this problem by neglecting loading rate effects. However, it is worth noting that loading rate effects on rock breakage are more complicated than the above discussions. For example, in addition to the effects on rock parameters, both the average fragment size after breakage and the energy absorption effectiveness vary with loading rate, which was pointed out by Zhang (1994). Therefore, on the whole the quasi-static approach is still an approximation, and more detailed approach concerning this subject would be needed.

9.6 EFFECTS OF PRE-EXISTING FRACTURES IN ROCK ON THE PRESENT MODELS

Successful application of the models established in the present report to a specific problem depends on three aspects:

a) the understanding of the mechanisms involved in the establishment of these models;
b) a selection of pertinent variables by which the rock in the field can be related to that tested in the laboratory;
c) the accuracy with which the rock tested in the laboratory is equated to that in the field.

We have explained a) and b) in the context. The third aspect will be focused on in this section.

The mechanical properties of rock are most readily obtained from laboratory experiments on specimens of rock. These specimens usually have

dimensions of approximately 30 to 500 mm and contain a sufficient number of structural particles, crystals and amorphous particles joined by cementing materials. Although the properties of the individual particles in the specimen may be different from one another and the individual crystals themselves are often anisotropic, such a specimen with a large amount of particles is grossly homogeneous since these particles and the grain boundaries interact in a sufficiently random manner. In addition to the structural particles, fractures, either pre-existing or induced by stresses, play an active, dramatic and vitally important role in practical rock excavation.

Rock fractures can be quite large, such as bedding planes, faults, joints, folds and other larger discontinuities, and cause the greatest concern in rock engineering. The predicted indentation depth, size of the cracked zone, length of the side crack, and length of the radial and median crack can be either increased or reduced in the vicinity of these structures depending on the relative positions of the indenter and the structures. This subject has been discussed by many authors, among them Pusch (1995). In general a wealth of knowledge concerning mechanical excavation design is available, which we can use once the geological structures are clearly known. The most difficult problem is how to detect these structures in advance inexpensively and quickly. However, this topic is beyond the discussion of our present report.

Fractures can also be rather small in dimension compared with the characteristic dimension of the target problem and such fractures are called micro cracks. All kinds of rock and rock-like material contain micro cracks. Micro cracks finally become macrocracks and lead to fracture of rocks under the action of increasing load. Therefore, rocks with nearly the same composition and different amounts of micro cracks may differ widely in properties. This has been noticed by many authors for quite a long time, for example Brace (1965), Walsh (1965a & b), Walsh (1966), Goldsmith (1973), Brace (1976), Budiansky & O'Connell (1976), Nelson et al. (1977), Houpertt (1979), Kou (1980), Alm et al. (1985), Kou & Alm (1986), Kou & Alm (1987), and Kou (1987). Through these works it can be concluded that a previous excavation-induced damage can lower the compressive strength, Young's modulus and energy release rate of the rock to be excavated if the number of micro cracks is sufficiently big. However, this does not necessarily mean that this damage can make the next excavation easier or the next excavation-induced cracks longer. For example in mechanical excavation, a sharp indenter penetrating a rock with a large number of micro cracks can act much like a blunt indenter and the subsurface cracks will therefore be reduced, as discussed previously (Kou et al 1994). The influence of damage on excavation is more complicated than that on rock properties. Zeuch et al. (1983) have performed several tests to investigate the influence of pre-existing damage on cutting behaviour which suggest that experiments on intact rock may provide an adequate measure of the response, despite the presence of pre-existing damage. The indentation phenomenon was recently observed on specimens with pre-existing damage at Luleå University (Prikryl & Kou, 1996). Artificial cracking by heating

was introduced to both granite and diorite specimens originally taken from Äspö Hard Rock Laboratory. The test results indicated that the crack pattern caused by indentation remained the same in heated and non-heated samples. The main difference observed was that a higher load was necessary for crater formation in non-heated samples compared with the heated ones but heated samples usually had shorter side cracks. We believe that further experimental work will be required to validate this observation.

10 SUMMARY AND CONCLUSIONS

A great number of experiments carried out at Luleå University depict a general picture of fractures in rocks under indentation. In this picture, there are three zones, i.e. a zone of disintegrated and partly compacted rock fragments, a crushed zone, and a cracked zone just underneath the indenter. Outside the cracked zone there are basically three systems of cracks: median cracks, radial cracks, and side cracks. Sometimes Hertzian cracks are also observed in rocks under indentation with an axially-symmetric indenter. Fully developed radial cracks on each side of the indented area can connect with each other and join with the median crack. This forms the so-called radial/median crack system. An indenter penetrates rock by expending a great amount of energy in crushing the rock. The force-displacement response is a reflection of the fractures in the rock. In any case the indenter will penetrate into the rock with increasing load and long cracks will remain in the rock.

The fractured states of the rock under indentation can be related to its constitutive behaviour. The crushed zone corresponds to the post-failure region of the rock material under compression, and the boundary of the crushed zone is therefore characterized by the limit strength of the rock. The cracked zone corresponds to the initial damage region. The main long cracks, such as the side cracks and the radial/median cracks, propagate correspondingly in the elastic region. The cracked zone and the main long cracks can therefore be simply treated by using elastic fracture mechanics.

A rather stable contact pressure is noticed on the contact face of a hemispherical indenter, showing ductile behaviour of the crushed rock. For a truncated indenter, the pressure variation is large at the beginning and tends towards a more stable situation with loading and rock crushing. The nominal contact pressure under a hemispherical indenter is lower than that under the truncated. A cavity model has been applied to describe the expansion of rock in the crushed zone and then to obtain the resulting stress field outside the zone. Rock crushing causes large tensile stresses around the outside of the cavity. The expansion extent of the crushed rock is affected by the zone shape and Poisson's ratio of the rock. Side cracks grow in preferred locations relative to the load and crushed zone situations. Side cracks grow in a mixed mode; shear and/or tensile driving forces can contribute to their formation. Rock properties and the cavity shapes of the crushed zone affect the side crack patterns. A deeper cavity causes deeper and longer side cracks. Large cavity expansion makes it easy for the side cracks to develop and go upward.

The size of the cracked zone caused by an indenter can be modelled numerically by a splitting fracture model. The fracture model predicts a fan

like pattern of subsurface fractures, which agrees with indentation experiments.

Semi-theoretical relationships between the indentation force and either the indentation depth or the length of the radial/median cracks have been established by using similarity methods for hemispherical, truncated, or cylindrical indenters, respectively. The relationships take into consideration the rock properties, the diameter of the indenters, and the indenter shape. With these relationships it is possible to predict the indentation depth and the induced crack length. These relationships also make it clear how the critical threshold values are associated with the formation of indentation depth and crack lengths in different rocks induced by different indenter types. Good agreement between the model and the experimental data is obtained.

A combination of these two categories of relationships, which describe the force-indentation depth relation and force-crack length relation respectively, results in relationships between indentation depth and crack length. These relationships indicate that resharpening blunt indenters can reduce cracks with the same rate of advance. They also indicate that a smaller indentation depth in each rotation round will produce shorter cracks. These are important to be considered in practical operation. One of the key rock mechanical parameters in the prediction of both indentation depth and crack length is the compressive strength. A modification of the uniaxial compressive strength obtained in ordinary rock mechanics laboratories makes it possible to include the influence of confinement, and, therefore, excavation in deep underground operations can be taken into account. It is also possible to explain why the simultaneous action of several indenters in mechanical excavation can produce shorter crack lengths compared with that by single indentation while taking the operation-induced-confinement into consideration.

REFERENCES

Alm, O., Jaktlund L.-L. and Kou Shaoquan, 1985. The influence of microcrack density on the elastic and fracture mechanical properties of Stripa granite. *Physics of the Earth and Planetary Interiors*, Vol. 40, pp 161-179.

Baker, W. E., Westine, P. S. and Dodge, F. T., 1978. *Similarity methods in engineering dynamics*. Hyden Book Company, Inc., New Jersey.

Bieniawski, Z. T., 1968. Propagation of brittle fracture in rock. Basic and Applied Rock Mechanics. *Proc. 10th Symp on Rock Mechanics*. Texas,

Brace W. F., 1965. Some new measurements of linear compressibility of rocks. *J. Geophys. Res.*, Vol. 70, No. 2, pp 391-398.

Brace, W. F., 1976. Direct observation of dilatant voids in rock. *The effects of voids on material deformation*, AMD, Vol. 16, pp 1-12.

Budiansky, B. and O'Connell, R. J., 1976. Elastic moduli of a cracked solid. *Int. J. Solid Structures*. Vol. 12, pp 81-97.

Chaudhri M. M. and Kurkjian C. R., 1986. Impact of small steel spheres on the surface of "normal" and "anomalous" glasses. *J. Amer. Ceram. Soc.*, Vol. 69, **No.** 5, pp 404-410.

Chaudhri M. M. and Walley S. M., 1978. Damage to glass surfaces by the impact of a small glass and steel sphere. *Phil. Mag.*, A Vol. 37, **No.** 2, pp 153-165.

Cherepanov, G. P., 1979. *Mechanics of Brittle Fracture*, McGraw-Hill Inc.

Chiang, S. S., Marshall, D. B. and Evans, A. G., 1982. The response of solids to elastic/plastic indentation, *J. Appl. Phys.* Vol. 53 No. 1, pp 298-317.

Cook, N. G. W., Hood, M. and Tsai, F., 1984. Observation of crack growth in hard rock by an indenter, *Int. J. Rock Mech. Min. Sci. & Geomech. Abstr.*, Vol. 21 No. 2, pp 97-107.

Crouch, S. L. and Starfield, A. M., 1983. *Boundary Element Methods in Solid Mechanics*, George Allen & Unwin, London.

Crouch, S. L., 1976. Solution of Plane Elasticity Problems by the Displacement Discontinuity Method, *Int. J. Num. Methods Engng.*, Vol. 10, pp 301-343.

Div. of Rock Mechanics, 1993. Rock mechanics datafile.

Evans, A. G. and Wilshaw T. R., 1977. Dynamic solid particle damage in brittle materials: an appraisal. *J. Matr. Sci.* Vol. 12, pp 97-116.

Evans, A. G., Gulden, M. E. and Rosenblatt, M., 1978. Impact damage in brittle materials in the elastic-plastic response regime. *Proc. R. Soc. London.* A. Vol. 361, pp 343-365.

Evans, I. 1962. A theory of the mechanics of coal ploughing, *Proc. Int. Symp. of Min. Res., G. Clark*, (Ed.), Pergamon Press, London, Vol. 2, pp 761-798.

Frank F. C. and Lawn B. R., 1967. On the theory of Hertzian fracture. *Proc. Roy. Soc.*, A Vol. 299, pp 291-306.

Goldsmith, W., 1973. Wave transmission in rocks,. *Rock Mechanics Symposium*, AMD, Vol. 3, pp 73-128.

Guo Hua, 1990. *Rock cutting using fracture mechanics principles*, PhD Thesis, University of Wollongong, N. S. W., Australia.

Hakami, H. and Stephansson, O., 1990. Shear fracture energy of Stripa granite—results of controlled triaxial testing, *Engng. Fract. Mech.* 2, Vol. 35, No. 4/5, pp 855-865.

Hardy, M. P. 1973. *Fracture mechanics applied to rock.* PhD thesis, University of Minnesota, Michigan.

Hill, R., 1951. *The mathematical theory of plasticity*, Oxford, Claredon Press.

Holmberg, M. and Forslund, J., 1989. Bergmekanik parameterbestämningar på Bohusgranit, Ekebergmarmor samt lumundasandsten, Internal report of the Division of Rock Mechanics, BM 1989:01 (in Swedish).

Horii H. and Nemat-Nasser, S. 1985. Compression induced microcrack growth in brittle solids: axial splitting and shear failure, *J. Geophy. Res.*, Vol. 90, No.B4, pp 3105-3125.

Houpertt, R., 1979. The fracture behavior of rocks. *Proc. 4th Int. Congr. Rock Mech.*, Montreux, Vol. 3, 1, pp 107-114.

Howarth, D. F. and Bridge, E. J., 1988. Technical note: Microfracture beneath blunt disc cutters in rock, *Int. J. Rock Mech. Min. Sci. & Geomech. Abstr.*, Vol. 25 No. 1, 35-38.

Hökmark, H. and Pusch, R., 1992. Koppling av mekaniska egenskaper till diskontinuiteter av olika ordning, SKB Arbetsrapport 92-71 (in Swedish).

Ingraffea, A. R. 1987. Theory of crack initiation and propagation in rock, Fracture Mechanics of Rock, B. K. Atkinson, (Ed.), Academic Press Geology series, pp71-110.

Jaeger, J. C. and Cook, N. G. W., 1979. *Fundamentals of Rock Mechanics*, Chapman and Hall, London.

Johnson, K. L., 1985. *Contact Mechanics*, Cambridge University Press.

Jung, S. J., Mohamed, E. and Whyatt, J. K., 1992. The study of fracture of brittle rock under pure shear loading, *Proc. of Rock Joint Symp.*, Berkely, U. S. A., pp 468-475.

Kou Shaoquan, 1980. Review on effects of micro cracks on the mechanical properties of rock. *Advances in Mechanics*, Vol. 10, No. 2/3, pp 89-98 (in Chinese).

Kou Shaoquan and Alm O., 1986. Effect of micro cracks on the tensile strength of granite. Proc. *SPT2 Conference* , Vienna, Austria. July 1-3, pp 709-719.

Kou Shaoquan and Alm O., 1987. Micro cracks and the tensile strength of granite. *Acta Mechanica Sinica,* Vol. 19, No. 4, pp 366-373 (in Chinese).

Kou Shaoquan, 1987. The effect of damage due to thermal cracking on the deformation and failure of granite. *Acta Mechanica Sinica*, Vol. 19, No. 6, pp 550-556 (in Chinese).

Kou Shaoquan, Ding Yansheng, Chen Li, Tao Jun and Ye Dongying, 1993. Effects of confining stress and pore fluid on the mechanical properties of burst coal. *Science in China* (series A), Vol. 23, No. 3, pp 263-270 (in Chinese).

Kou Shaoquan, Lindqvist P.-A. and Tan Xiangchun, 1994. Conceptual model of crack structure in rock caused by mechanical excavation. SKB Project Report PR 44-94-022.

Kou Shaoquan, Lindqvist, P. A. and Tan Xiangchun, 1995a. Mechanics of rock breakage under indentation load. *Bergmekanikdagen*, pp149-170.

Kou Shaoquan, Lindqvist, P. A. and Tan Xiangchun, 1995b. An analytical and experimental investigation of rock indentation fracture. Proc. *The 8th International Congress on Rock Mechanics*, 25-29 Sept. Tokyo, Japan, pp 181-184.

Kou Shaoquan, Lindqvist, P. A. and Tan Xiangchun, 1996. Formulation of models for indentation depth and crack length in mechanical excavation of rock, *SKB report,* HRL-96-20.

Kou Shaoquan, Ye Dongying and Ding Yansheng, 1990. A constitutive model for structured coal based on fracture and damage mechanics. *Engineering Fracture Mechanics*, Vol. 35, No. 4/5, pp 835-843.

Kou Shaoquan, Zhang Zongxian and Yu Jie, 1989. Rock fracture induced by an indenter. *Chinese J. Rock Mechanics and Engineering*, Vol. 8, No. 4, pp 275-285 (in Chinese).

Kou, Shaoquan, 1995. *Some basic problems in rock breakage by blasting and indentation,* Ph. D thesis, 1995:180D, Luleå University, Sweden.

Kranz R. L., 1983. Micro cracks in rock, *Tectophysics*, Vol. 100, pp 449-480.

Kumano, A. and Goldsmith, W., 1982. An analytical and experimental investigation of the effect of impact on coarse granular rocks. *Rock Mechanics*, Vol. 15, pp 67-97.

Lawn, B. and Wilshaw, R., 1975. Review indentation fracture; principles and applications, *J. Mater. Sci.* Vol. 10, pp 1049-1081.

Lawn, B. R., 1968, Hertzian fracture in single crystals with the diamond structure, *J. Appl. Phys.*, Vol. 19 No. 10, pp 4828-4836.

Lawn, B. R., Fuller, E. R. and Wiederhorn, S. M., 1976. Strength degradation of brittle surfaces: sharp indenters. *J. Am. Ceram. Soc.* Vol. 59, No. 5-6, pp. 193-197.

Li, C. and Gao, S., 1986. Effects of tensile and unloading-induced cracking behind rotary drilling cutters on the breakage of rock, *J. of Central South Inst. of Min. & Metallurgy*, Vol. 2, pp 14-20 (in Chinese).

Li, C. and Nordlund, E., 1993. Deformation of brittle rocks under compression —with particular reference to micro cracks, *Mech. of Mater.*, Vol. 15, pp 223-239.

Li, C., 1995. Micromechanics modelling for stress-strain behaviour of brittle rocks, *Int. J. for Num. & Anal. Meth. in Geomech.*, Vol. 19, pp 331-344.

Li, V. C., 1991. Mechanics of shear rupture applied to earthquake zones, *Fracture Mechanics of Rock*, Atkinson K. B. (ed). Academic Press, London, pp 351-428.

Lindqvist, P-A, Suarez del Rio L. M., Montoto M., Tan Xiangchun. and Kou Shaoquan, 1994. Rock indentation database-testing procedures, results and main conclusions. SKB Project Report PR 44-94-023.

Lindqvist, P-A., Lai, H. H. and Alm, O., 1984. Indentation fracture development in rock continuously observed with a scanning electron

microscope, *Int. J. Rock Mech. Min. Sci. & Geomech. Abstr.*, Vol. 21 No. 4, pp 165-182.

Lundberg, B., 1974. Penetration of rock by conical indenters, *Int. J. Rock Mech. Min. Sci. & Geomech. Abstr.*, Vol. 11, No. 209-214.

Lundqvist, R. G., 1981. Hemispherical indentation and the design of "button" bits for percussive drilling. *Proc. 22nd Symp. Rock Mech., Cambridge (AIME)*, pp 219-222.

Luong, M. P., 1992. Shear fracture of rocks in mode II and mode III, *Eurock '92*. Thomas Telfoud, London, pp 36-41.

Maurer, W. O., 1967. The state of rock mechanical knowledge in drilling, *Proc. 8th Symp. Rock Mech.*, New York, pp 355-395.

Morton, W. B. and Close, L. J., 1922. Notes on Hertz's theory of the contact of elastic bodies, *Phylosophycal Magzine*, Vol. 43, pp 321-329.

Nelson, A. C. and Wang, C. Y., 1977. Non-destructive observation of cracks in stressed rocks. *Int. J. Rock Mech. Min. Sci. & Geomech. Abstr.*, Vol. 14, pp 103-107.

Olsson, O. and Winberg, A., 1996. Current understanding of extent and properties of the excavation disturbed zone and its dependance of excavation method. *Proceeding of the Excavation Disturbed Zone Workshop*, Sept. 20, Winnipeg, Manitoba Canada, pp 101-112 .

Ouchterlony, F., 1986. Brottseghetsdata (in Swedish).

Pang, S. S. and Goldsmith, W., 1990. Investigation of crack formation during loading of brittle rock. *Rock Mechanics and Rock Engineering*, Vol. 23, pp 53-63.

Pang, S. S., Goldsmith, W. and Hood, M., 1989. A force-indentation model for brittle rocks. *Rock Mechanics and Rock Engineering*, Vol. 22, pp 127-148.

Paone, J. and Tandanand, S., 1965. Inelasticity deformation of rock under a hemispherical drill bit, *Proc. 7th Symp. Rock Mech.*, New York (AIME), pp 149-174.

Potts, E. L. J. and Shuttleworth, P. 1958. A study of ploughability of coal, with special reference to the effects of blade shape, direction of planning to the cleat, planning speed and the influence of water infusion. *Tran. Inst. Min. Engr.*, London, Vol. 117, pp. 520-548

Prikryl, R. and Kou Shaoquan, 1996. Fractures caused by indentation in cracked granitoids. Research report TULEA 1996:24 ISSN 0347-0881.

Pusch, R., 1989. Influence of various excavation techniques on the structure and physical properties of "near-field" rock around large boreholes. SKB Technical Report, 89:32.

Pusch, R., 1995. *Rock Mechanics on a Geological Base. Developments in Geotechnical Engineering,* Vol. *77*. Elsevier Publ. Co. (ISBN: 0-444896 13-9).

Saouma, V. E. and Kleeinosky, M. 1984. Finite element simulation of rock cutting; a fracture mechanics approach. *Proc. 25th U. S. Symp. on Rock Mech.*, pp 792-799.

Shen, B. and Stephansson O., 1993. Numerical analysis of Mode I and Mode II propagation of rock fractures, *Int. J. Rock Mech. Min. Sci. & Geomech. Abstr.(Special issue for the 34th U. S. Symposium on rock mechanics)*.

Shen, B. and Stephansson O., 1994. Modification of the G-criterion for Crack Propagation Subjected to Compression, *Engng. Fract. Mech.,* Vol. 47, No. 2, pp 177-189.

Shen, B.,1993. *Mechanics of Fractures and Intervening Bridges in Hard Rocks*, Ph.D. Thesis, Royal Institute Technology, Stockholm, Sweden.

SKB, 1994. Äspö Hard Rock Laboratory annual report 1993. SKB Technical Report, 94-11.

Sprunt, E. S. and Brace, W. F., 1974. Direct observation of microcavities in crystalline rocks, *Int. J. Rock Mech. Min. Sci. & Geomech. Abstr.*, Vol. 11, pp 139-150.

Tan Xiangchun, 1996. *Modelling of Drill String Buckling and Tool Indentation in Rock Drilling and Fragmentation,* Ph. D thesis, 1996:197D, Luleå University, Sweden.

Tan Xiangchun, Kou Shaoquan and Lindqvist, P-A, 1994. Cracks in rock caused by mechanical excavation, SKB AR 44-94-002.

Tan Xiangchun and Kou Shaoquan, 1997. Simulation of rock indentation subsurface cracks and side cracks using fracture mechanics and numerical methods, SKB project report (to be published).

Tan Xiangchun and Shen, B., 1995. Simulation of rock splitting process by DDM, *Proc. of 3rd Int. Symp. on Min. Mech. and Auto.*, Golden, Colorado, U. S. A., June 12-14, Vol. 2, pp 7-16.

Vutukuri, V. S., Rustan, A. and Alm, O., 1983. Influence of physical properties of rock and rock-like material on blastability in crater and slab blasting - A literature and model study, Report GF (Swedish Mining Research Foundation) 8221, Luleå.

Wagner, H. and Schumann, E. H. R., 1971. The stamp-load bearing strength of rock. An experimental and theoretical investigation. *Rock Mechanics*, Vol. 3, pp 185-207.

Walsh, J. B., 1965a. The effects of cracks on the compressibility of rocks. *J. Geophys. Res.*, Vol. 70, pp 381-389.

Walsh, J. B., 1965b. The effects of cracks on the uniaxial elastic compression of rocks. *J. Geophys. Res.*, Vol. 70, pp 399-411.

Walsh, J. B., 1966. Seismic wave attenuation in rock due to friction. *Geophysics,* Vol. 71, pp 2591-2599.

Whittaker, B. N., Singh R. N. and Sun G., 1992. *Rock Fract. Mech. — principles, design and applications*, Elsevier, Amsterdam.

Xu, S., Reinhardt, H. W. and Gappoev, M. 1996. Mode II fracture testing for highly orthotropic materials like wood, *Int. J. of Fract.*, Vol. 75, pp 185-214.

Yoffe, E. H., 1982. Elastic stress field caused by indenting brittle materials, *Phyl. Mag. A*, Vol. 46, No. 4, pp 617-628.

Zeuch, D. H., Swenson, D. V. and Finger, J. T., 1983. Subsurface damage development in rock during drag-bit cutting: observations and model predictions. 24th U. S. Symposium on Rock Mechanics, June.

Zhang Zongxian and Kou Shaoquan, 1990. On rock fracture under static and dynamic indentations. *Journal of University of Science and Technology Beijing,* Vol. 12, No. 5, pp 401-407 (in Chinese).

Zhang Zongxian, 1994. *Principles of rock breakage and its applications.* Metallurgical Industry Press. Beijing, China (in Chinese).